



PNNL-29823

General Analysis of Data Collected from DOE Lidar Buoy Deployments Off Virginia and New Jersey

April 2020

William J Shaw
Jennifer Draher
Gabriel Garcia Medina
Alicia M Gorton
Raghavendra Krishnamurthy
Rob K Newsom
Mikhail Pekour
Lindsay M Sheridan
Zhaoqing Yang

DISCLAIMER

This report was prepared as an account of work sponsored by an agency of the United States Government. Neither the United States Government nor any agency thereof, nor Battelle Memorial Institute, nor any of their employees, makes **any warranty, express or implied, or assumes any legal liability or responsibility for the accuracy, completeness, or usefulness of any information, apparatus, product, or process disclosed, or represents that its use would not infringe privately owned rights.** Reference herein to any specific commercial product, process, or service by trade name, trademark, manufacturer, or otherwise does not necessarily constitute or imply its endorsement, recommendation, or favoring by the United States Government or any agency thereof, or Battelle Memorial Institute. The views and opinions of authors expressed herein do not necessarily state or reflect those of the United States Government or any agency thereof.

PACIFIC NORTHWEST NATIONAL LABORATORY
operated by
BATTELLE
for the
UNITED STATES DEPARTMENT OF ENERGY
under Contract DE-AC05-76RL01830

Printed in the United States of America

Available to DOE and DOE contractors from the
Office of Scientific and Technical Information,
P.O. Box 62, Oak Ridge, TN 37831-0062;
ph: (865) 576-8401
fax: (865) 576-5728
email: reports@adonis.osti.gov

Available to the public from the National Technical Information Service
5301 Shawnee Rd., Alexandria, VA 22312
ph: (800) 553-NTIS (6847)
email: orders@ntis.gov <<https://www.ntis.gov/about>>
Online ordering: <http://www.ntis.gov>

General Analysis of Data Collected from DOE Lidar Buoy Deployments Off Virginia and New Jersey

April 2020

William J Shaw
Jennifer Draher(a)
Gabriel Garcia Medina
Alicia M Gorton
Raghavendra Krishnamurthy
Rob K Newsom
Mikhail Pekour
Lindsay M Sheridan
Zhaoqing Yang

Prepared for
the U.S. Department of Energy
under Contract DE-AC05-76RL01830

Pacific Northwest National Laboratory
Richland, Washington 99354

(a) Bureau of Ocean Energy Management
Washington, DC 20240

Abstract

Pacific Northwest National Laboratory (PNNL) operates two AXYS WindSentinel lidar buoys for the U.S. Department of Energy's Wind Energy Technologies. The purpose of these buoys is to collect hub-height winds and supporting meteorological and oceanographic information to facilitate the development of offshore wind energy in the U.S. In general, each buoy is deployed for a year or more at a given location in order to capture at least a full annual cycle of weather conditions. The initial deployment for one buoy was off the coast of Virginia beginning in 2015, and the other buoy was first deployed off the coast of New Jersey beginning in 2016. Over the last two years, PNNL has had an opportunity to analyze the data collected during these first two deployments.

This report describes a substantial analysis of data collected by the two lidar buoys operated off the coasts of Virginia and New Jersey. The centerpiece instrument for each buoy as deployed off Virginia and New Jersey is a lidar system, which is designed to measure the horizontal wind vector from approximately 40 m to 200 m above the sea surface with vertical resolution of 40 m. Since the initial deployments, the original lidars have been replaced with Leosphere 866 v2 systems. The analyses in this report will apply to the original Vindicator systems. In addition to the wind profiles from the lidars, the buoys collect near-surface measurements of wind speed and direction, air temperature, relative humidity, barometric pressure, and solar irradiance. Oceanographic variables measured include the two-dimensional wave spectrum, water temperature and conductivity, and ocean current vectors to a depth of 90 m.

An assessment of overall data recovery and a basic analysis of the data collected was provided in a previous report. This report substantially extends that analysis. The various sections describe the development and application of an inertial measurement unit (IMU) data recovery scheme for the New Jersey deployment; a climatological analysis of winds at hub height and at the surface together with thermodynamic variables measured at the surface for the full deployment periods; an analysis of oceanographic observations regarding sea state; the development of a refinement for NOAA's WaveWatch III model to allow its application to near-shore areas; a basic climatology of ocean currents observed from the buoys; an analysis of observed winds in the framework of Monin-Obukhov Similarity Theory; and the development and evaluation of techniques to extract turbulence intensity and turbulence kinetic energy from the lidars.

The analyses contained in this report provide a great deal of new information about offshore conditions on the U.S. East Coast. In addition, the experience gained will inform both configurations and analysis of data from future deployments of these lidar buoy systems.

Acknowledgments

We are grateful to the Bureau of Ocean Energy Management (BOEM) of the Department of the Interior for supporting BOEM staff member Jennifer Draher's contribution to the analysis of buoy current data through a detail at Pacific Northwest National Laboratory (PNNL) in the summer of 2019. We also thank Brian Gaudet of PNNL for his constructive technical suggestions as well as his technical review of the final document. This work was funded by the Wind Energy Technologies Office of the Department of Energy's (DOE) Office of Energy Efficiency and Renewable Energy. PNNL is operated by the Battelle Memorial Institute for the U.S. DOE under Contract DE AC05 76RL01830.

Acronyms and Abbreviations

3D	three-dimensional
ADCP	Acoustic Doppler Current Profiler
AGL	above ground level
BAO	Boulder Atmospheric Observatory
DBS	Doppler beam swinging
DJF	December, January, February
DOE	U.S. Department of Energy
IEC	International Electrotechnical Commission
IMU	inertial measurement unit
JJA	June, July, August
KPI	key performance indicator
MAM	March, April, May
MO	Monin-Obukhov
NCEP	National Centers for Environmental Prediction
NOAA	National Oceanic and Atmospheric Administration
OADS	Optical Air Data Systems
pBias	percent bias
PNNL	Pacific Northwest National Laboratory
R ²	coefficient of determination
RF	random forest
RMSE	root-mean-square error
SON	September, October, November
TI	turbulence intensity
TKE	turbulence kinetic energy
TOGA/COARE	Tropical Ocean-Global Atmosphere Coupled-Ocean Atmosphere Response Experiment
UTC	coordinated universal time
XPIA	eXperimental Planetary boundary layer Instrumentation Assessment

Contents

Abstract.....	ii
Acknowledgments.....	iii
Acronyms and Abbreviations.....	iv
1.0 Introduction	1.1
1.1 Buoy Instrumentation	1.2
2.0 Recovery of Lidar Winds During the New Jersey Deployment	2.1
2.1 Background.....	2.1
2.2 Method.....	2.2
2.2.1 OADS IMU Correction	2.4
2.2.2 Roll, Pitch, and Yaw Offsets	2.5
2.2.3 Proxy for OADS IMU	2.7
2.3 Wind Retrieval and Motion Compensation	2.7
2.3.1 Reprocessed Winds	2.8
2.4 Average Winds	2.13
2.5 Summary	2.19
3.0 Basic Climatology of Wind and Other Meteorological Variables.....	3.1
3.1 Overview of Meteorological Instrumentation.....	3.1
3.2 Hub-Height Analysis – Wind	3.1
3.3 Near-Surface Analysis	3.8
3.3.1 Wind.....	3.8
3.3.2 Temperature.....	3.15
3.3.3 Relative Humidity.....	3.16
3.3.4 Pressure.....	3.17
3.4 Summary	3.18
4.0 Basic Climatology of Sea State	4.1
4.1 Historical Context of Sea State	4.1
4.2 Sea State Analysis Over Deployment Lifetime	4.3
4.2.1 Spatial Characteristics.....	4.3
4.2.2 Lidar Buoys	4.4
4.2.3 Tidal Influence	4.9
4.3 Numerical Model Development	4.10
4.3.1 Wind Forcing	4.11
4.3.2 Surface Currents	4.12
4.3.3 Ocean-Atmosphere Coupling	4.13
4.4 Summary	4.15
5.0 Basic Climatology of Ocean Currents	5.1
5.1 Data Quality Analysis.....	5.1

5.2	Comparison of Ocean Current Data to Other Buoy Sensor Data.....	5.5
5.3	Ocean Current Data Trends.....	5.11
5.4	Summary	5.13
6.0	Preliminary Analysis of the Wind Profile	6.1
6.1	Wind Shear, Fluxes and Monin-Obukhov Similarity Theory.....	6.1
6.2	Summary	6.5
7.0	Extraction of Turbulence from Vindicator Doppler Lidars	7.1
7.1	Mathematical Preliminaries	7.1
7.2	Measurement Campaign.....	7.3
7.3	Lidar Turbulence Retrieval Algorithms	7.3
	7.3.1 Turbulence Intensity Performance	7.8
	7.3.2 Turbulence Kinetic Energy Performance	7.10
	7.3.3 Lidar Uncertainty Quantification.....	7.15
7.4	Summary	7.18
8.0	General Summary	8.1
9.0	References.....	9.1
	Appendix A – Format of NetCDF Files Containing Reprocessed 1 Hz Winds.....	A.1
	Appendix B – Format of NetCDF Files Containing Reprocessed Time Averaged Winds.....	B.1

Figures

Figure 1.1.	One of two AXYS WindSentinel buoys operated by PNNL for DOE.	1.1
Figure 1.2.	Illustration of the instrument layout on each of the DOE buoys. The lidar illustrated is a new Leosphere 866 v2 that has now replaced the original OADS Vindicator III whose data are analyzed in this report.	1.3
Figure 2.1.	Wind direction from the surface wind sensor (blue) and the Vindicator at 90 m (red). The yellow shaded regions represent time periods with invalid roll, pitch and yaw data from the Vindicator’s internal inertial measurement unit.	2.1
Figure 2.2.	The DOE AXYS WindSentinel buoy showing the locations of the Vindicator III, and the AXYS IMU.	2.2
Figure 2.3.	Schematic representation of the offset between the corrected OADS and the AXYS IMU coordinate systems.	2.2
Figure 2.4.	Comparison of roll (<i>top</i>), pitch (<i>middle</i>), and yaw (<i>bottom</i>) data for the original OADS (brown), corrected OADS (blue), and original AXYS (red) IMU measurements.....	2.5
Figure 2.5.	Distributions of the difference between (a) the corrected OADS roll and the AXYS roll angle, and (b) the corrected OADS pitch and the AXYS pitch angle. These distributions were obtained using 1 Hz data from November 5, 6, 8, and 9, 2015.....	2.6
Figure 2.6.	Median difference (black curve) between the corrected OADS yaw and the AXYS yaw angle, as a function of the AXYS yaw angle. These results were obtained using 1 Hz data from November 5, 6, 8, and 9, 2015.....	2.6
Figure 2.7.	Panels a) and b) show the “body” coordinate system for the corrected OADS IMU data. Also shown is the geometry for the outgoing laser beams. Panel c) shows the “body” coordinate system for the AXYS IMU data.....	2.7
Figure 2.8.	North, east, and down components of the Vindicator winds reprocessed using the corrected OADS IMU data. This example was taken from November 10, 2015.	2.9
Figure 2.9.	North, east, and down components of the Vindicator winds reprocessed using the proxy IMU data. This example was taken from November 10, 2015.....	2.10
Figure 2.10.	Reprocessed 1 Hz winds (red curves) at the 90 m level for January 10, 2016. Panels a), b), c), and d) show the corrected OADS yaw angle, the eastward velocity component, the northward velocity component, and the vertical velocity component, respectively. The original OADS winds are shown in black.	2.11
Figure 2.11.	[Reprocessed 1 Hz winds (red curves) at the 90 m level for December 17, 2015. Panels a), b), c), and d) show the corrected OADS yaw angle, the eastward velocity component, the northward velocity component, and the vertical velocity component, respectively. The original OADS winds are shown in black.	2.12
Figure 2.12.	Reprocessed 1 Hz winds (red curves) at the 90 m level for August 13, 2016. Panels a), b), c), and d) show the corrected OADS yaw angle, the	

	eastward velocity component, the northward velocity component, and the vertical velocity component, respectively. The original 1 Hz OADS winds are shown in black.	2.13
Figure 2.13.	RMSE (<i>top</i>) and correlation (<i>bottom</i>) between the reprocessed and OADS 1 Hz winds as a function of the box-car averaging width. These results were computed using data obtained on November 11, 2015, at the 90 m level. Dashed lines in the figures represent thresholds discussed in the text above.	2.14
Figure 2.14.	10-minute results at the 90 m level for March 11, 2016. a) Data quality flags for wind measurements (black) and platform attitude measurements (blue). b) Reprocessed (red) and OADS (blue) wind speeds. c) Reprocessed (red) and OADS (blue) wind directions. d) Reprocessed (red) and OADS (blue) vertical velocity. RMSE difference (<i>top</i>) and correlation (<i>bottom</i>) between the reprocessed and OADS 1 Hz winds as a function of the box-car averaging width. These results were computed using data obtained on November 11, 2015, at the 90 m level.	2.16
Figure 2.15.	10-minute results at the 90 m level for March 11, 2016. a) Data quality flag platform attitude measurements (blue). b) Reprocessed (red) and OADS (blue) wind speed standard deviations. c) Reprocessed (red) and OADS (blue) wind direction standard deviations. d) Reprocessed (red) and OADS (blue) vertical velocity standard deviations.	2.17
Figure 2.16.	10-minute results at the 90 m level for March 11, 2016. a) Data quality flag platform attitude measurements (blue). b) Proxy (red) and OADS (blue) yaw angle. c) Proxy (red) and OADS (blue) roll standard deviations. d) Proxy (red) and OADS (blue) pitch standard deviations.	2.18
Figure 2.17.	Data quality flag for wind measurements (<i>top</i>) and lidar signal strengths at 90 m for each of the three beams (<i>bottom</i>).	2.19
Figure 3.1.	90 m wind speed distributions for the Virginia and New Jersey deployments.	3.1
Figure 3.2.	90 m wind speed and direction distributions for the Virginia and New Jersey deployments.	3.2
Figure 3.3.	Mean monthly 90 m wind speeds for the Virginia and New Jersey deployments. The Virginia deployment covered two winters and springs, and one summer and fall, from December 2014–May 2016. The New Jersey deployment covered two winters and one spring, summer, and fall, from November 2015–February 2017.	3.2
Figure 3.4.	Seasonal spread in hub-height wind speeds for Virginia and New Jersey.	3.3
Figure 3.5.	Seasonal wind roses for the Virginia deployment.	3.4
Figure 3.6.	Seasonal wind roses for the New Jersey deployment.	3.5
Figure 3.7.	Average diurnal hub-height wind speed for Virginia and New Jersey deployments.	3.6
Figure 3.8.	Diurnal spread in hub-height wind speeds for Virginia and New Jersey.	3.6
Figure 3.9.	Distribution of the stability parameter for $z = 4$ m for the Virginia and New Jersey deployments.	3.7
Figure 3.10.	Hub-height winds speed distributions by stability class.	3.8

Figure 3.11. Near-surface wind speed distributions for the Virginia and New Jersey deployments.3.9

Figure 3.12. Near-surface wind roses for the Virginia and New Jersey deployments.3.9

Figure 3.13. Near-surface monthly wind speeds for Virginia and New Jersey.3.10

Figure 3.14. Spread in near-surface wind speeds for Virginia and New Jersey, respectively.3.10

Figure 3.15. Seasonal distribution of near-surface wind for the Virginia deployment.3.11

Figure 3.16. Seasonal distribution of near-surface wind for the New Jersey deployment.3.12

Figure 3.17. Diurnally-averaged near-surface wind speeds for Virginia and New Jersey.3.13

Figure 3.18. Diurnal spread in near-surface wind speeds for Virginia and New Jersey.3.13

Figure 3.19. Near-surface wind speed distributions by stability class for Virginia and New Jersey.3.14

Figure 3.20. Difference between hub-height and near-surface wind speeds as a function of atmospheric stability.3.15

Figure 3.21. Seasonal distributions of near-surface air temperature for Virginia and New Jersey.3.16

Figure 3.22. Diurnal distributions of near-surface air temperature for Virginia and New Jersey.3.16

Figure 3.23. Seasonal distributions of 4 m relative humidity for Virginia and New Jersey.3.17

Figure 3.24. Diurnal distributions of 4 m relative humidity for Virginia and New Jersey.3.17

Figure 3.25. Seasonal distributions of air pressure for Virginia and New Jersey.3.18

Figure 4.1. Bathymetry of the study region in pseudo color and with buoy locations identified.4.1

Figure 4.2. Empirical cumulative probability density functions of significant wave height at three long-term buoys in the Mid-Atlantic Bight. Dashed lines represent the period where lidar buoys were deployed.4.2

Figure 4.3. Altimetry-derived significant wave height climatology during lidar buoy deployment period. Red triangles mark the location of lidar buoys. Black line corresponds to the 200 m isobath. Note that color limits vary for all plots.4.4

Figure 4.4. Distributions of significant wave height and wave direction for the Virginia and New Jersey deployments, respectively.4.5

Figure 4.5. Bivariate distributions between significant wave height and peak period for the (a) Virginia and (b) New Jersey deployments. The percentages of occurrence above 0.01% are shown in each bin for a total sum of 100%.4.5

Figure 4.6. Like Figure 4.5 but for mean wave period.4.6

Figure 4.7. Significant wave height and maximum wave height histograms for the (a) Virginia and (b) New Jersey deployment.4.6

Figure 4.8. Monthly significant wave height spread.4.7

Figure 4.9. Empirical cumulative probability density functions of significant wave height for the (a) Virginia and (b) New Jersey deployments.4.7

Figure 4.10. Monthly wave roses for the Virginia deployment. Significant wave height is shown in the colors.....4.8

Figure 4.11. Monthly wave roses for the New Jersey deployment. Significant wave height is shown in the colors.4.9

Figure 4.12. Power spectra of the significant wave height time series for the Virginia (a) and New Jersey (b) deployments.....4.10

Figure 4.13. Model data comparisons for January 2016.....4.12

Figure 4.14. Average surface current intensity for 2016. VA and NJ stand for the buoy deployments off Virginia and New Jersey, respectively.4.13

Figure 4.15. Model data comparisons for models with different atmospheric coupling intensities (β_{max}) and surface currents (U_s).....4.14

Figure 5.1. Current magnitude and direction color plots for the Virginia ocean current data record.....5.2

Figure 5.2. Current magnitude and direction color plots for the New Jersey ocean current data record.....5.2

Figure 5.3. Current magnitude and direction by bin, averaged over 5 days, for the Virginia ocean current data record.5.3

Figure 5.4. Current magnitude and direction by bin, averaged over 5 days, for the New Jersey ocean current data record.....5.4

Figure 5.5. Current roses (*left*), wave roses (*center*), and wind roses (*right*) for February 2015 and February 2016 of the Virginia buoy deployment.5.6

Figure 5.6. Current roses (*left*), wave roses (*center*), and wind roses (*right*) for December 2015 and December 2016 of the New Jersey buoy deployment.5.7

Figure 5.7. Wind speed (a), significant wave height (b), current magnitude (c), and a comparison of the mean-normalized averages (d) for the Virginia deployment.5.8

Figure 5.8. Wind speed (a), significant wave height (b), current magnitude (c), and a comparison of the mean-normalized averages (d) for the New Jersey deployment.5.8

Figure 5.9. Wind direction (a), wave direction (b), current direction (c), and a comparison of the averages (d) for the Virginia deployment.....5.9

Figure 5.10. Wind direction (a), wave direction (b), current direction (d), and a comparison of the averages (d) for the New Jersey deployment.5.9

Figure 5.11. Vector plot comparison of 12-hour averaged currents, waves, and winds for the Virginia deployment.5.10

Figure 5.12. Vector plot comparison of 12-hour averaged currents, waves, and winds for the New Jersey deployment.....5.11

Figure 5.13. Current roses for the Virginia (*left*) and New Jersey (*right*) deployments for the trimmed data records.5.12

Figure 5.14. Hourly, monthly, and seasonal boxplots for the Virginia deployment trimmed data record.....5.12

Figure 5.15. Hourly, monthly, and seasonal boxplots for the New Jersey deployment trimmed data record.....5.13

Figure 6.1. Wind speed shear as a function of the air-sea temperature difference for a) the Virginia deployment and b) the New Jersey deployment.....6.1

Figure 6.2. Comparison between observations and the results of the bulk method for January 2015 during the Virginia deployment. a) Observed surface wind speed (red) and the friction velocity from the bulk method (blue). b) Observed air-sea virtual temperature difference (red) and the sensible heat flux from the bulk method (blue). c) Observed wind shear (red) and the wind shear implied by the bulk method (blue).....6.4

Figure 6.3. Scatter plots showing the bulk method wind shear versus the observed wind shear during a) the entire Virginia deployment and b) the entire New Jersey deployment.....6.5

Figure 7.1. Location of the Vindicator lidars near the BAO tower during XPIA field campaign in 2015.....7.3

Figure 7.2. Effect of cross-contamination between the wind components using the lidar DBS measurement technique (Kelberlau and Mann 2019).7.5

Figure 7.3. *u*-component power spectral density from sonic anemometer, Vindicator lidar, and Windcube v2 lidar during neutral, stable, and very unstable atmospheric conditions.7.6

Figure 7.4. PNNL 1 Hz wind vector processing compared to OADS smoothed estimates.7.6

Figure 7.5. *u*-component power spectral density of sonic anemometer, Windcube v2, and Vindicator lidars using both OADS- and PNNL-processed 1 Hz data. The resonance wavelengths are shown by the dotted black lines.7.7

Figure 7.6. Turbulence intensity comparisons between a) Vindicator lidar, b) Windcube v2 and sonic anemometer. The color bar represents the number of samples in each bin.7.8

Figure 7.7. Turbulence intensity profiles of a) availability, b) normalized root-mean-square error, c) coefficient of correlation, and d) slope values from a linear fit from both Vindicator and Windcube v2 lidar compared to a sonic anemometer.....7.9

Figure 7.8. a) Atmospheric stability distribution observed during the XPIA field campaign from sonic anemometer data at the BAO tower, and b) percentage errors in turbulence intensity as a function of atmospheric stability for the Vindicator lidars. The error bars indicate 1 standard deviation.7.10

Figure 7.9. 10-minute statistical comparison between PNNL-processed and OADS-processed TKE estimates with sonic anemometer for varying averaging seconds (0 seconds refers to no averaging, i.e., instantaneous): a) coefficient of determination, b) slope of the linear regression, c) intercept of the linear regression, and d) root-mean-square error between the lidar and sonic datasets.7.11

Figure 7.10. Mann uniform shear model fit to sonic anemometer at 100 m AGL on March 22, 2015, at 00 hrs. The fit parameters are also shown.....7.13

Figure 7.11. Unbiased predictor importance for TKE estimates using Vindicator lidar data. The predictor variables are WS – windspeed, TI – turbulence intensity, Unc – lidar TKE uncertainty, alpha – wind shear, and Wp – vertical velocity variance.7.14

Figure 7.12. a) The uncertainty of TKE from Vindicator lidar measurements and b) time series of 10-minute averaged TKE estimates from sonic and two best methods of lidar TKE estimates (Methods 1 and 3).7.17

Figure 7.13. Error in TKE estimates between Method 3 and sonic anemometer at 100 m AGL versus lidar TKE uncertainty during XPIA campaign. Higher lidar uncertainty shows poorer confidence in TKE estimates.....7.18

Tables

Table 1.1. Instrument complement for each of the DOE lidar buoys during the Virginia and New Jersey Deployments.....1.2

Table 4.1. Model resolution conversion table from spherical to planar coordinates and time steps used. 38°N is used as a reference latitude for the conversions.....4.11

Table 4.2. Error statistics for sensitivity analysis.4.15

Table 7.1. Stability classification based on *L* thresholds (Sathe et al. 2011).7.5

Table 7.2. Key performance indicators for turbulence measurements.....7.8

Table 7.3. Evaluation of Vindicator lidar TKE methods compared to sonic anemometer at 100 m AGL.....7.15

1.0 Introduction

Pacific Northwest National Laboratory (PNNL) operates two AXYS WindSentinel lidar buoys for the U.S. Department of Energy's (DOE) Wind Energy Technologies Office (Figure 1.1). The purpose of these buoys is to collect hub-height winds and supporting meteorological and oceanographic information to facilitate the development of offshore wind energy in the United States. In general, each buoy is deployed for a year or more at a given location in order to capture at least a full annual cycle of weather conditions.

This report describes a substantial analysis of data collected by the two lidar buoys operated off the coasts of Virginia and New Jersey. The Virginia buoy was on station approximately 40 km offshore from December 2014–May 2016. The New Jersey buoy was deployed approximately 5 km offshore from November 2015–February 2017. During the deployments the buoys sampled vector wind profiles from approximately 40 m to 200 m above the surface. In addition, the buoys collected supporting meteorological and oceanographic information, including near-surface winds, temperature, humidity, the two-dimensional wave spectrum, and ocean temperature and currents. Most of the data were recorded at 1-second intervals and processed to 10-minute or other averaging periods either on-board the buoy or in post-processing.



Figure 1.1. One of two AXYS WindSentinel buoys operated by PNNL for DOE.

1.1 Buoy Instrumentation

The centerpiece instrument for each buoy as deployed off Virginia and New Jersey is a Vindicator III lidar manufactured by Optical Air Data Systems (OADS), which is designed to measure the horizontal wind vector from approximately 40 m to 200 m above the sea surface with vertical resolution of 40 m. Since the initial deployments, the original lidars have been replaced with more powerful Leosphere 866 v2 systems. The analyses in this report will apply to the original Vindicator systems. In addition to the wind profiles from the lidars, the buoys collect near-surface measurements of wind speed and direction, air temperature, relative humidity, barometric pressure, and solar irradiance. Oceanographic variables measured include the two-dimensional wave spectrum, water temperature and conductivity, and ocean current vectors to a depth of 90 m. These are summarized in Table 1.1.

Table 1.1. Instrument complement for each of the DOE lidar buoys during the Virginia and New Jersey Deployments.

Sensor Type	Manufacturer	Model
Wind Profile	Optical Air Data Systems	Vindicator III
Wind Speed (2)	Vector Instruments	A100R
Wind Direction	Vector Instruments	WP200
Temperature, Relative Humidity	Rotronic	MP101A
Barometer	RM Young	61302V
Pyranometer	Licor	LI-200
Water Temperature	AXYS	YSI
Conductivity, Temperature, Depth (CTD)	Seabird	SBE 37SMP-1j-2-3c
Wave	AXYS	TRIAXYS NW II
Current Profile (Acoustic Doppler Profiler; ADP)	Nortek	Aquadopp 400 kHz
Tilt/Compass	MicroStrain	3DM GX3 25

The locations of the various instruments on the buoys are shown in Figure 1.2. Note that this diagram shows the newer Leosphere 866 v2 lidar system rather than the Vindicator III. The original Vindicator is visible in Figure 1.1 and later in Figure 2.2.

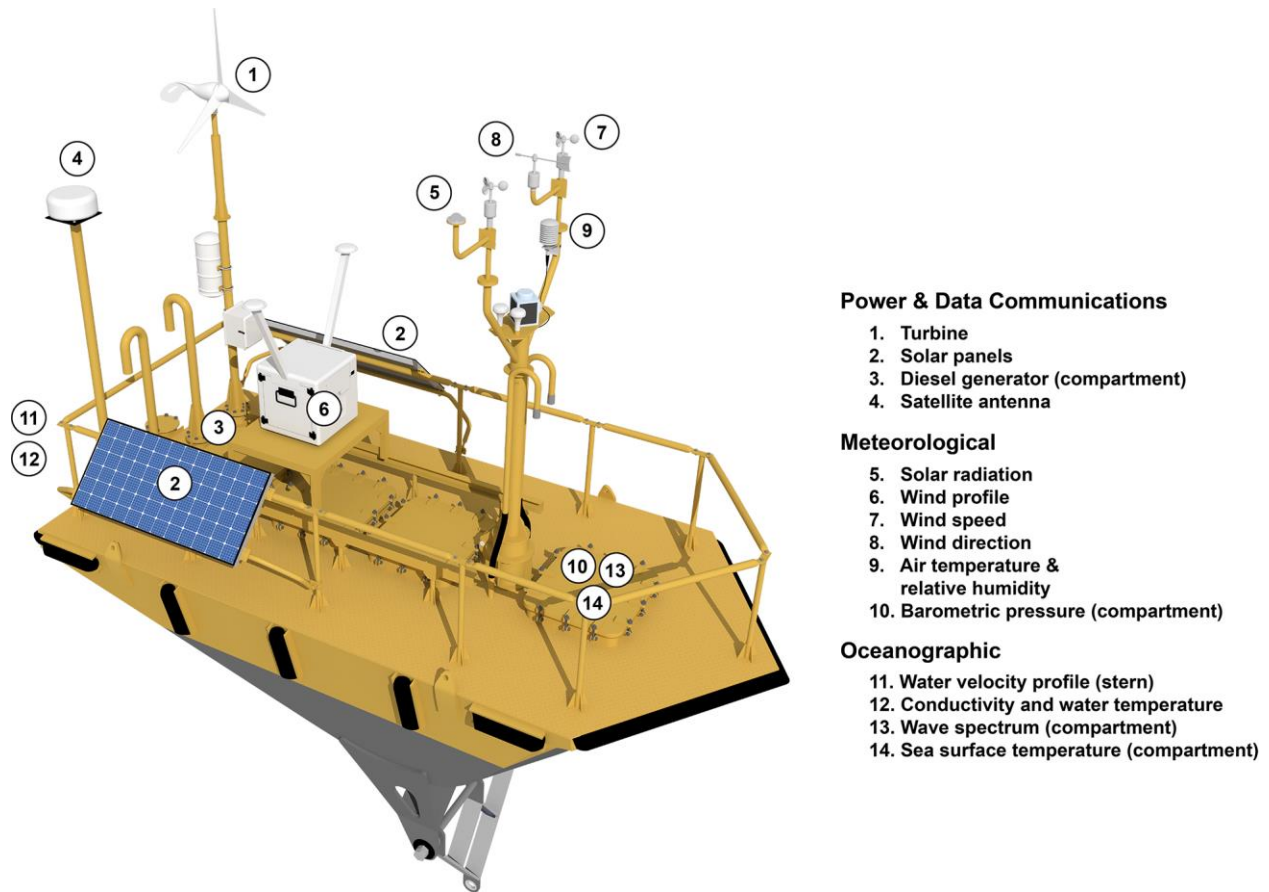


Figure 1.2. Illustration of the instrument layout on each of the DOE buoys. The lidar illustrated is a new Leosphere 866 v2 that has now replaced the original OADS Vindicator III whose data are analyzed in this report.

An assessment of overall data recovery and a basic analysis of the data collected was provided in Shaw et al. (2018). This report substantially extends that analysis. Section 2.0 describes the development and application of a data recovery scheme for the New Jersey buoy’s deployment. For a substantial fraction of the deployment period, the inertial measurement unit (IMU) for the lidar did not produce valid data. For mathematical reasons, this did not significantly affect wind speed measurements, but it made wind directions unusable. The data recovery scheme used orientation information from the buoy wave sensor as a surrogate for the lidar’s information to successfully recover virtually all of the lost information. Section 3.0 provides a climatological analysis of winds at hub height and the surface together with thermodynamic variables measured at the surface for the full deployment periods. Section 4.0 focuses on the oceanographic observations made by both buoys to describe sea state over the full deployment periods. In addition, this section describes the development of a refinement for National Oceanic and Atmospheric Administration’s (NOAA) WaveWatch III model to allow its application to near-shore areas. Section 5.0 provides a basic climatology of ocean currents observed from the buoys during the deployments. Section 6.0 extends the analysis of observed winds to an evaluation in the framework of Monin-Obukhov Similarity Theory. Finally, Section 7.0 describes the development and evaluation of techniques to extract turbulence intensity and turbulence kinetic energy from the lidars. The section provides an evaluation of these variables derived from a Vindicator III lidar using eddy-correlation flux data collected during the eXperimental Planetary boundary layer Assessment Experiment in 2015.

2.0 Recovery of Lidar Winds During the New Jersey Deployment

2.1 Background

The U.S. Department of Energy (DOE) AXYS WindSentinel buoy (S/N 6NB00130) was deployed ~5 km off the New Jersey coast (near Atlantic City) from ~November 6, 2015, until February 7, 2017. In the course of analyzing the raw (1 sec.) lidar data from this deployment we discovered that there were periods of time when the lidar’s internal IMU generated invalid attitude data, i.e., invalid roll, pitch, and yaw data. During these periods, the roll, pitch, and yaw measurements from the Vindicator IMU would “flat-line” for hours or days at a time. The frequency and duration of these failures generally increased with time during the deployment. Figure 2.1 illustrates how much of the New Jersey data set is affected by this failure. Time periods highlighted in yellow are those periods with invalid IMU data from the Vindicator. The Vindicator relies on its internal IMU to perform motion compensation. Without valid attitude data, the wind measurements are suspect.

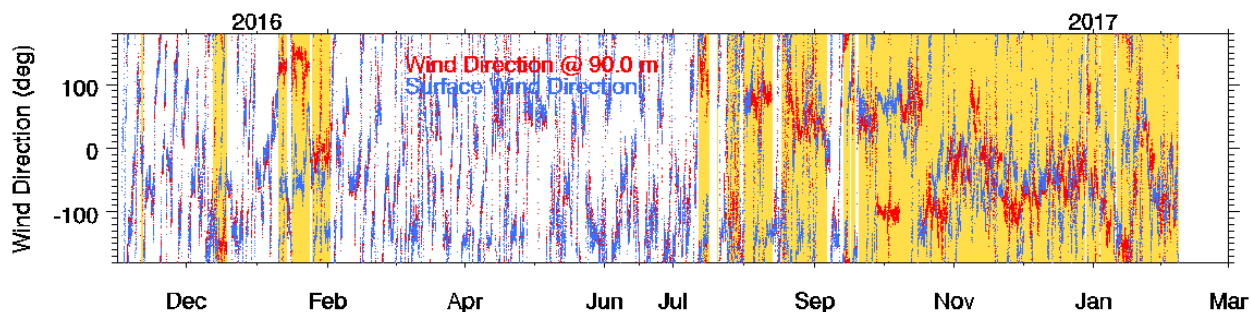


Figure 2.1. Wind direction from the surface wind sensor (blue) and the Vindicator at 90 m (red). The yellow shaded regions represent time periods with invalid roll, pitch and yaw data from the Vindicator’s internal inertial measurement unit.

In addition to the IMU inside the Vindicator lidar, the AXYS WindSentinel buoy has its own IMU (a Microstrain 3DM-GX3-25). The AXYS IMU was mounted on the mast next to the navigation light enclosure, as indicated in Figure 2.2. This sensor provides a redundant source of buoy attitude data that could potentially be used in place of the Vindicator’s internal IMU to correct the wind measurements for effects of platform motion. Inspection of the AXYS IMU data indicates that this sensor was working throughout the entire deployment. In this section we describe how the AXYS IMU data were used to recover the lidar wind measurements during periods when the Vindicator’s internal IMU was not working.

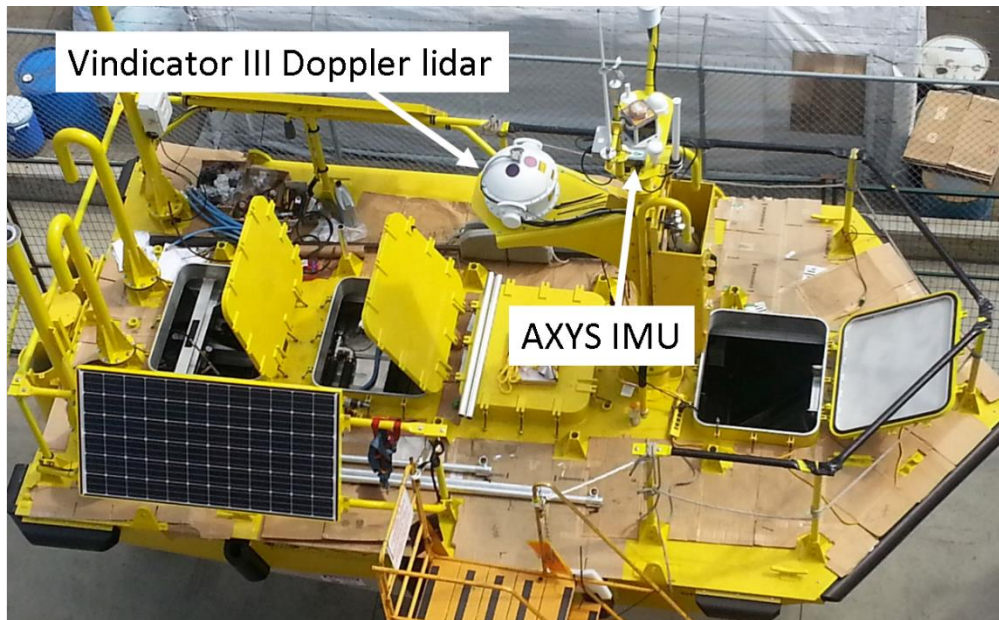


Figure 2.2. The DOE AXYS WindSentinel buoy showing the locations of the Vindicator III, and the AXYS IMU.

2.2 Method

In order to substitute the AXYS IMU data for the Vindicator III (also referred to as “OADS” after the manufacturer, Optical Air Data Systems) IMU data we need to understand how the coordinate systems for the two sensors are oriented relative to each other. Figure 2.3 shows a schematic representation of the OADS and AXYS sensor coordinates. The x-axis defines the heading direction, the y-axis points toward starboard, and the z-axis points down (consistent with the standard aerospace convention). As indicated in Figure 2.3, there is a small offset between the two sensor coordinate systems, and this results in differences in the roll, pitch, and yaw measurements. The first task was then to determine these offsets during periods when both IMUs were working. Once determined, the offsets were then added to the AXYS roll, pitch, and yaw measurements to produce a proxy dataset that is used in place of the OADS IMU data.

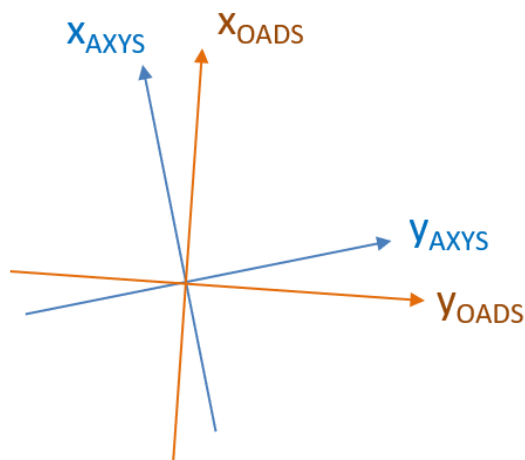


Figure 2.3. Schematic representation of the offset between the corrected OADS and the AXYS IMU coordinate systems.

The roll, pitch, and yaw measurements from the AXYS IMU are consistent with the standard aerospace convention. The transformation from sensor coordinates to Earth-fixed coordinates (i.e., north, east, and down) is given by

$$\begin{pmatrix} \text{north} \\ \text{east} \\ \text{down} \end{pmatrix} = R_z(\alpha_{AXYS})R_y(\beta_{AXYS})R_x(\gamma_{AXYS}) \begin{pmatrix} x_{AXYS} \\ y_{AXYS} \\ z_{AXYS} \end{pmatrix} \quad (2.1)$$

where

- α_{AXYS} is the AXYS yaw angle
- β_{AXYS} is the AXYS pitch angle
- γ_{AXYS} is the AXYS roll angle.

The rotation matrices, where χ is the appropriate above angle, are given by

$$R_x(\chi) = \begin{pmatrix} 1 & 0 & 0 \\ 0 & \cos \chi & -\sin \chi \\ 0 & \sin \chi & \cos \chi \end{pmatrix} \quad (2.2)$$

$$R_y(\chi) = \begin{pmatrix} \cos \chi & 0 & \sin \chi \\ 0 & 1 & 0 \\ -\sin \chi & 0 & \cos \chi \end{pmatrix} \quad (2.3)$$

and

$$R_z(\chi) = \begin{pmatrix} \cos \chi & -\sin \chi & 0 \\ \sin \chi & \cos \chi & 0 \\ 0 & 0 & 1 \end{pmatrix} \quad (2.4)$$

By contrast, the OADS IMU data are a bit more difficult to interpret. The reason for this is rooted in the history of the Vindicator. The Vindicator was originally designed to be mounted on the underside of a helicopter in order to provide range-resolved wind measurements in the forward (i.e., heading) direction. In this configuration, the OADS IMU was mounted horizontally with its x-axis pointing in the heading direction, and z down, consistent with the usual aerospace convention. When the Vindicator was “adapted” to provide wind measurements in the vertical direction, as on the buoys, it appears no attempt was made to reorient the internal IMU. As a result, the OADS IMU measurements correspond to a sensor that is pitched up by 90° (i.e., rotation about the y-axis). This was a complicating design choice because the limits on the pitch measurement are $\pm 90^\circ$. Thus, as the sensor pitches through zenith, the roll and yaw angles are forced to swing by $\pm 180^\circ$ in order to maintain a pitch angle that is less than or equal to 90° .

2.2.1 OADS IMU Correction

In our case, it is preferable to have a vertically oriented Vindicator corresponding to a pitch and roll of zero. Instead, the OADS IMU data contains an extra rotation in pitch that must first be removed in order to apply the transformation given by Equation (2.1). Figure 2.4 shows a comparison between the AXYS and the OADS roll, pitch, and yaw measurements. From this figure it is possible to see how the effect of the 90° pitch rotation can be “deconvolved” from the OADS data. The procedure for doing this is as follows:

- $\gamma_{OADS} = -\gamma_{OADS}$
 - For $\gamma_{OADS} > 90^\circ$ set $\gamma_{OADS} \rightarrow \gamma_{OADS} - 180^\circ$
 - For $\gamma_{OADS} < -90^\circ$ set $\gamma_{OADS} \rightarrow \gamma_{OADS} + 180^\circ$
- $\beta_{OADS} = 90^\circ - \beta_{OADS}$
 - For $\gamma_{OADS} > 90^\circ$ set $\beta_{OADS} \rightarrow -\beta_{OADS}$
 - For $\gamma_{OADS} < -90^\circ$ set $\beta_{OADS} \rightarrow -\beta_{OADS}$
- $\alpha'_{OADS} = \alpha_{OADS}$
 - For $\alpha_{OADS} < 0$ set $\alpha'_{OADS} = \alpha_{OADS} + 360^\circ$
 - $\alpha'_{OADS} \rightarrow \alpha'_{OADS} - 180^\circ$
 - Perform linear interpolation to obtain estimates of α'_{OADS} where $|\gamma'_{OADS}| > 90^\circ$.

In the procedure outlined above, the corrected OADS yaw, pitch, and roll are referred to as α'_{OADS} , β'_{OADS} , and γ'_{OADS} , respectively. As shown in Figure 2.4, the corrected OADS data are highly correlated with the AXYS measurements.

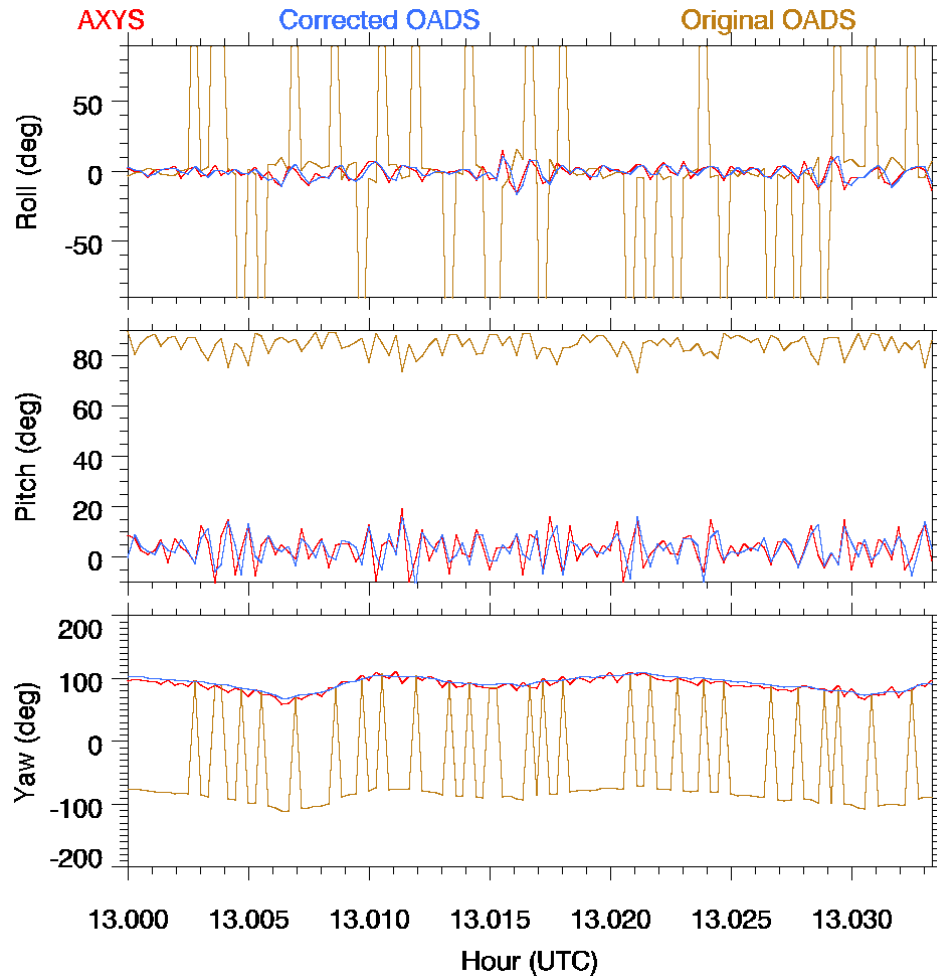


Figure 2.4. Comparison of roll (*top*), pitch (*middle*), and yaw (*bottom*) data for the original OADS (brown), corrected OADS (blue), and original AXYS (red) IMU measurements.

2.2.2 Roll, Pitch, and Yaw Offsets

The corrected OADS data can be compared directly to the AXYS IMU measurements in order to establish the roll, pitch, and yaw offsets that are necessary to create the proxy OADS IMU dataset. Figure 2.5 shows distributions of the roll and pitch differences computed using all 1 Hz data acquired on November 5, 6, 8, and 9, 2015. This was prior to the first failure of the OADS IMU, which occurred on November 11, 2015, at approximately 07:00 coordinated universal time (UTC). As shown in Figure 2.5, the pitch and roll differences are quite small. The median roll difference (OADS-AXYS) was found to be 0.49° , and the median pitch difference was found to be 0.29° .

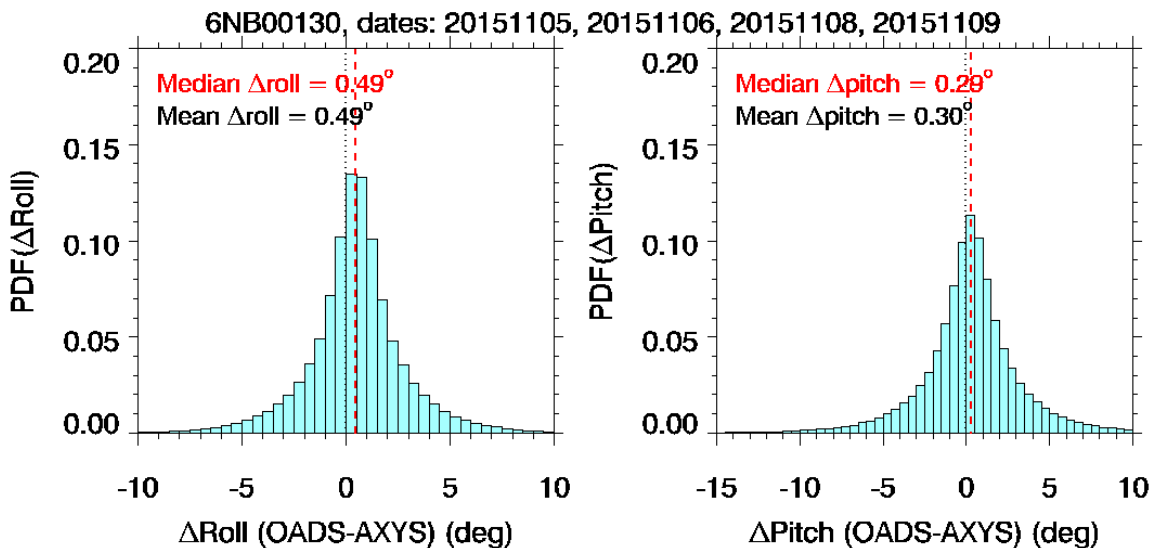


Figure 2.5. Distributions of the difference between (a) the corrected OADS roll and the AXYS roll angle, and (b) the corrected OADS pitch and the AXYS pitch angle. These distributions were obtained using 1 Hz data from November 5, 6, 8, and 9, 2015.

When computing the yaw differences, we found the yaw difference to be a function of the yaw itself. This may be due to differences in the magnetometer calibrations between the two IMUs. Figure 2.6 shows the median yaw difference (OADS-AXYS) as function of the AXYS yaw angle. Again, these differences were computed from data acquired on November 5, 6, 8, and 9, 2015. We note that we also computed roll, pitch, and yaw offsets for other periods during the New Jersey deployment when the OADS IMU was working. The results from these other periods were found to be consistent with the results shown in Figure 2.5 and Figure 2.6.

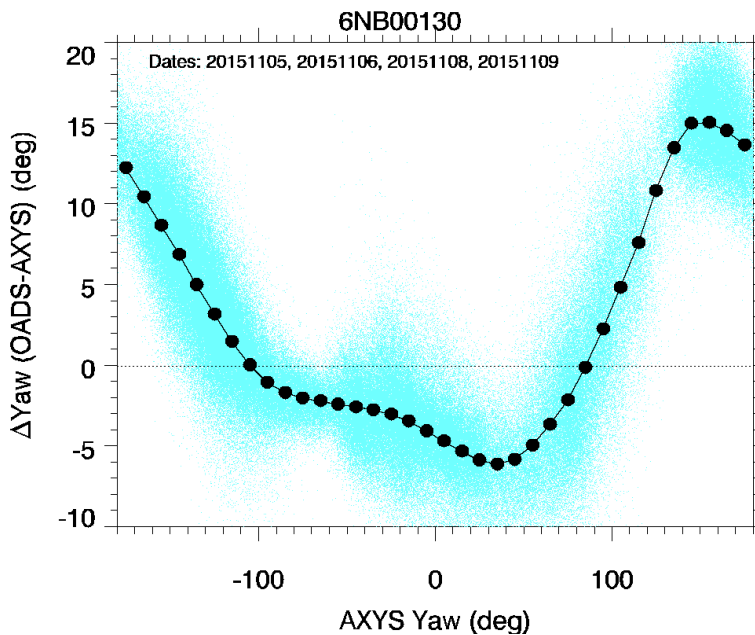


Figure 2.6. Median difference (black curve) between the corrected OADS yaw and the AXYS yaw angle, as a function of the AXYS yaw angle. These results were obtained using 1 Hz data from November 5, 6, 8, and 9, 2015.

2.2.3 Proxy for OADS IMU

Once the roll, pitch, and yaw offsets are determined from the AXYS and the corrected OADS IMU data, the proxy OADS IMU data are given by

$$\alpha_{OADS}^{proxy} = \alpha_{AXYS} + \Delta\alpha(\alpha_{AXYS}) \tag{2.5}$$

$$\beta_{OADS}^{proxy} = \beta_{AXYS} + \Delta\beta \tag{2.6}$$

$$\gamma_{OADS}^{proxy} = \gamma_{AXYS} + \Delta\gamma \tag{2.7}$$

where $\Delta\alpha$, $\Delta\beta$, and $\Delta\gamma$ are the median yaw, pitch, and roll differences shown in in Figure 2.5 and Figure 2.6.

2.3 Wind Retrieval and Motion Compensation

Figure 2.7 shows the body coordinates corresponding to the corrected OADS and AXYS IMU measurements. The x-axis is directed toward the bow, the y-axis points toward the starboard side, and the z-axis points down.

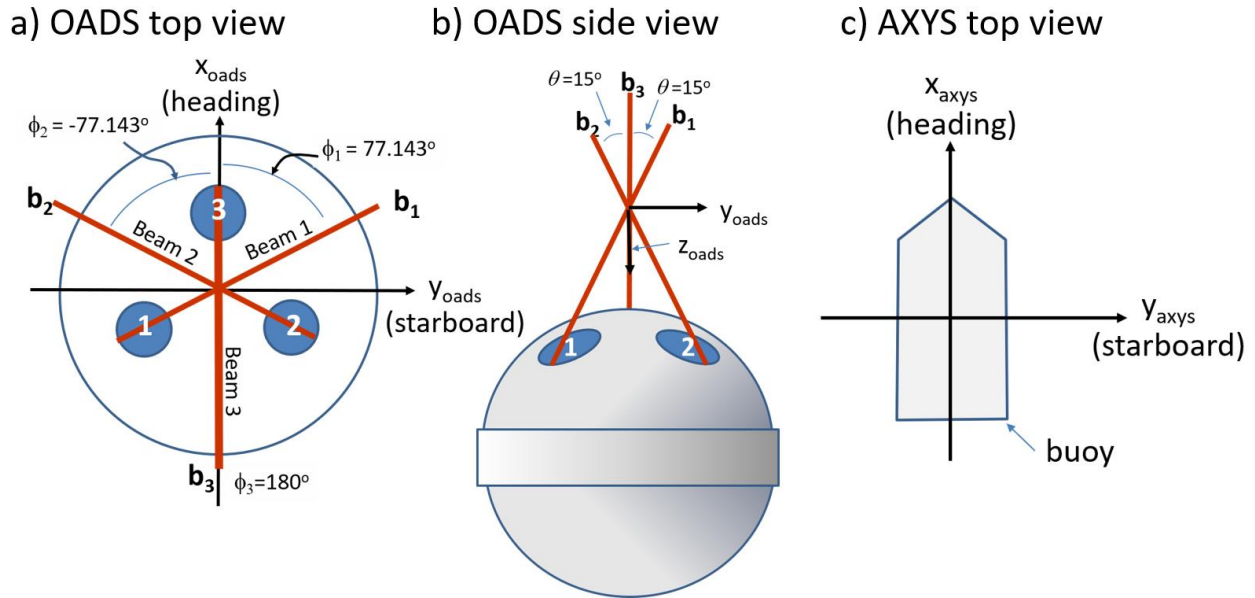


Figure 2.7. Panels a) and b) show the “body” coordinate system for the corrected OADS IMU data. Also shown is the geometry for the outgoing laser beams. Panel c) shows the “body” coordinate system for the AXYS IMU data.

The unit vectors that define the laser beam pointing directions are given by

$$\mathbf{b}_i = \hat{x} \cos \phi_i \sin \theta + \hat{y} \sin \phi_i \sin \theta - \hat{z} \cos \theta \tag{2.8}$$

where \hat{x} , \hat{y} , and \hat{z} are unit vectors along the x, y, and z directions (in the corrected OADS body frame), respectively. The beam pointing directions are defined by the azimuth angles,

$\phi_1 = 77.143^\circ$, $\phi_2 = -77.143^\circ$, and $\phi_3 = 180^\circ$, as shown in Figure 2.7. The beam zenith angles are $\phi = 15^\circ$ for all three beams. Note that the laser beams do not exit perpendicular to the windows. Instead, the beams exit in such a way that they intersect at a common point about 25 cm above the lidar, as shown in Figure 2.7.

The lidar measures radial velocity along three laser beams. For a given range gate, this three-beam measurement results in the following linear system

$$\begin{pmatrix} ur_1 \\ ur_2 \\ ur_3 \end{pmatrix} = \begin{pmatrix} \cos \phi_1 \sin \theta & \sin \phi_1 \sin \theta & -\cos \theta \\ \cos \phi_2 \sin \theta & \sin \phi_2 \sin \theta & -\cos \theta \\ \cos \phi_3 \sin \theta & \sin \phi_3 \sin \theta & -\cos \theta \end{pmatrix} \begin{pmatrix} u \\ v \\ w \end{pmatrix} \quad (2.9)$$

where ur_1 , ur_2 , and ur_3 are the radial velocities along the \mathbf{b}_1 , \mathbf{b}_2 , and \mathbf{b}_3 unit vectors, respectively. The heading, starboard, and down velocity components in the sensor frame are denoted by u , v , and w , respectively.

The solution of Equation (2.9) gives the components of the wind vector (u , v , w) expressed in body coordinates. The motion-compensation procedure simply involves transforming this vector from the body frame to the Earth frame (ignoring translational motions). This can be accomplished using either the proxy data derived from the AXYS IMU,

$$\begin{pmatrix} U_{north} \\ U_{east} \\ U_{down} \end{pmatrix} = R_z(\alpha_{AXYS}^{proxy}) R_y(\beta_{AXYS}^{proxy}) R_x(\gamma_{AXYS}^{proxy}) \begin{pmatrix} u \\ v \\ w \end{pmatrix} \quad (2.10)$$

or the corrected OADS IMU data,

$$\begin{pmatrix} U_{north} \\ U_{east} \\ U_{down} \end{pmatrix} = R_z(\alpha'_{OADS}) R_y(\beta'_{OADS}) R_x(\gamma'_{OADS}) \begin{pmatrix} u \\ v \\ w \end{pmatrix} \quad (2.11)$$

2.3.1 Reprocessed Winds

Figure 2.8 shows the result of reprocessing the Vindicator radial velocity measurements using the corrected OADS IMU data. Similarly, Figure 2.9 shows the result of reprocessing the same data using the proxy OADS IMU as derived from the AXYS IMU data. The black curves in both of these figures represent results from the original OADS processing. The results of Figure 2.8 and Figure 2.9 are nearly identical, as expected. We speculate that the original OADS winds were subjected to substantial smoothing. The reprocessed (red) results shown in both Figure 2.8 and Figure 2.9 were smoothed using an 11-point box-car average. Despite this averaging, it is still noisier than the original OADS result. We also note that the results using the proxy data (Figure 2.9) appear to exhibit slightly more noise than the results using the corrected OADS IMU data (Figure 2.8). This appears to be due to the slightly noisier AXYS IMU measurements.

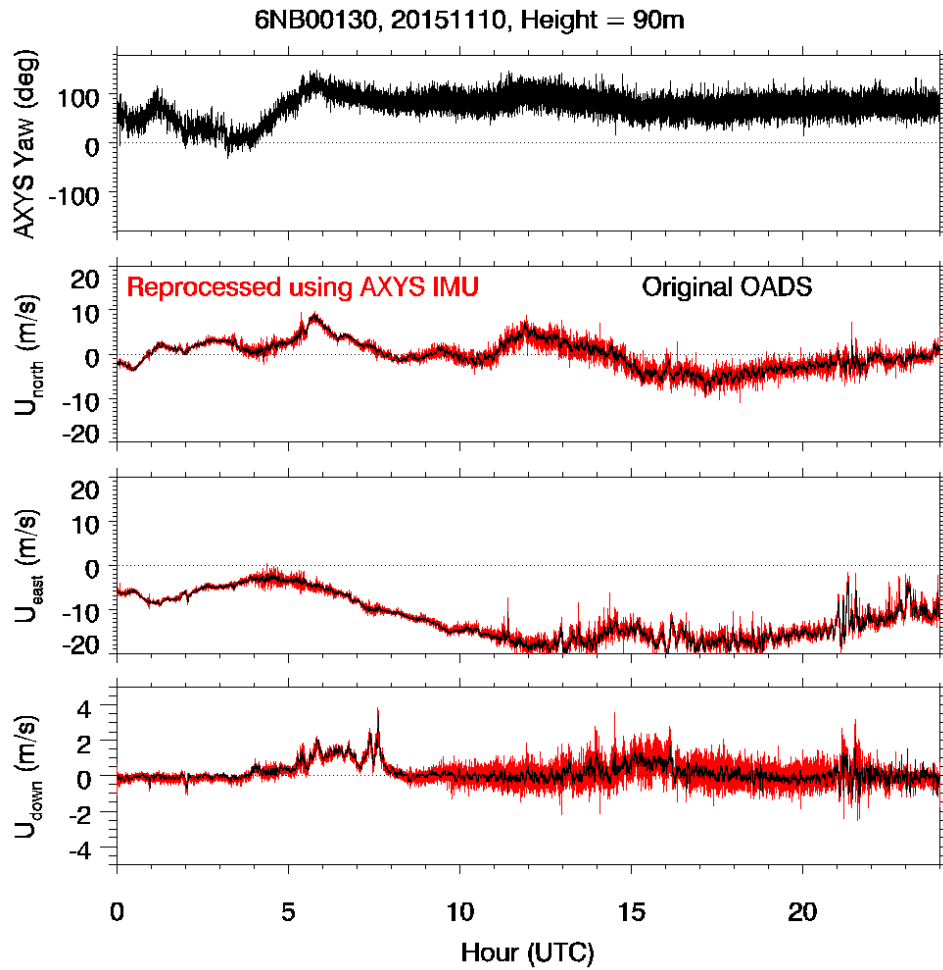


Figure 2.8. North, east, and down components of the Vindicator winds reprocessed using the corrected OADS IMU data. This example was taken from November 10, 2015.

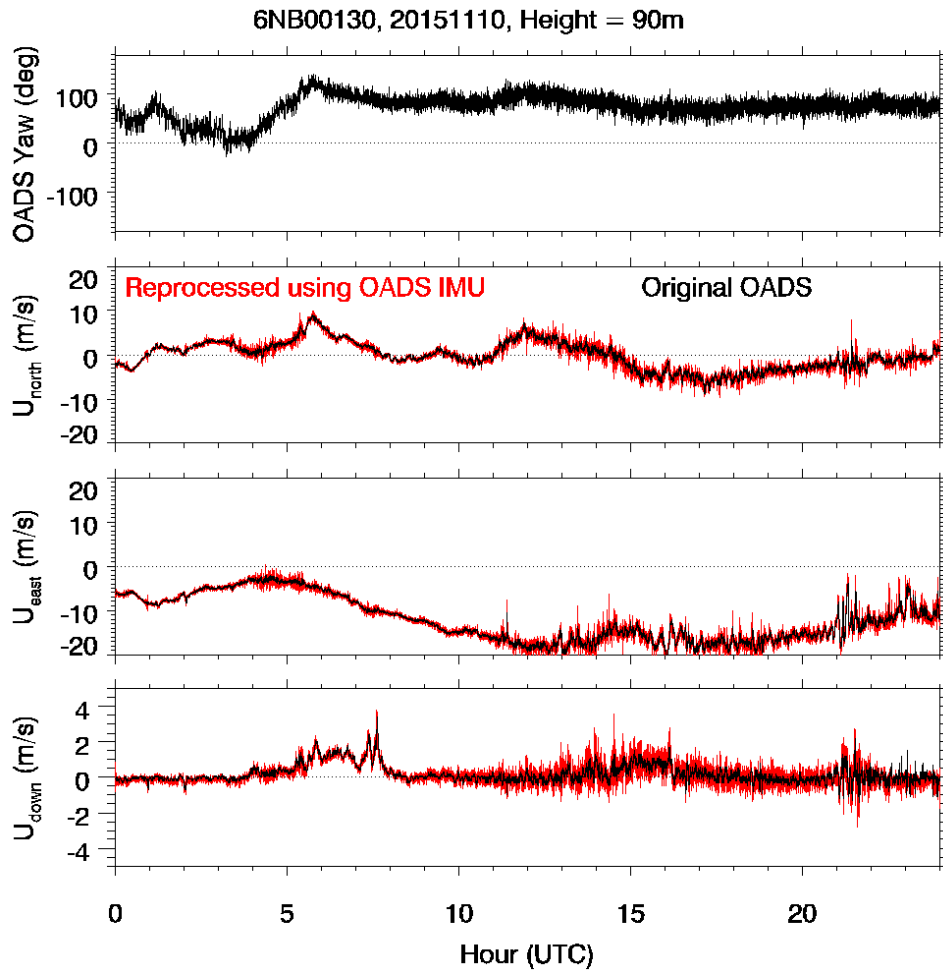


Figure 2.9. North, east, and down components of the Vindicator winds reprocessed using the proxy IMU data. This example was taken from November 10, 2015.

Figures 2.10 through 2.12 show examples of reprocessed winds using the proxy IMU data (red curves) for cases in which the OADS IMU data were invalid for either the entire day or part of the day. Figure 2.10 illustrates how the reprocessed winds and OADS winds diverge from one another after the OADS IMU flat-lines. Figure 2.11 shows an example of how radically the winds differ on a day when the OADS IMU was not functioning at all. Figure 2.12 illustrates how the winds converge after the OADS IMU comes back to life.

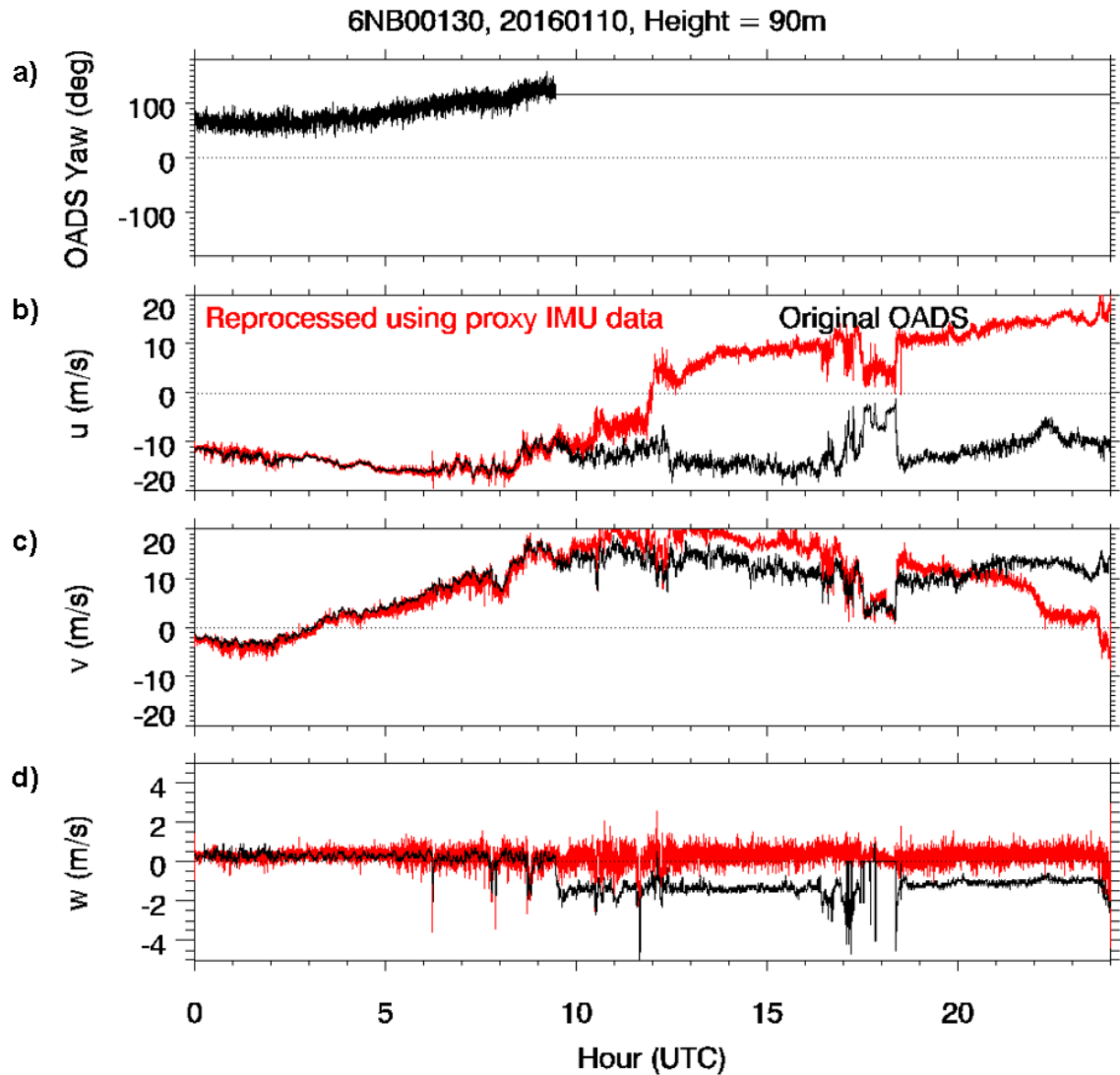


Figure 2.10. Reprocessed 1 Hz winds (red curves) at the 90 m level for January 10, 2016. Panels a), b), c), and d) show the corrected OADS yaw angle, the eastward velocity component, the northward velocity component, and the vertical velocity component, respectively. The original OADS winds are shown in black.

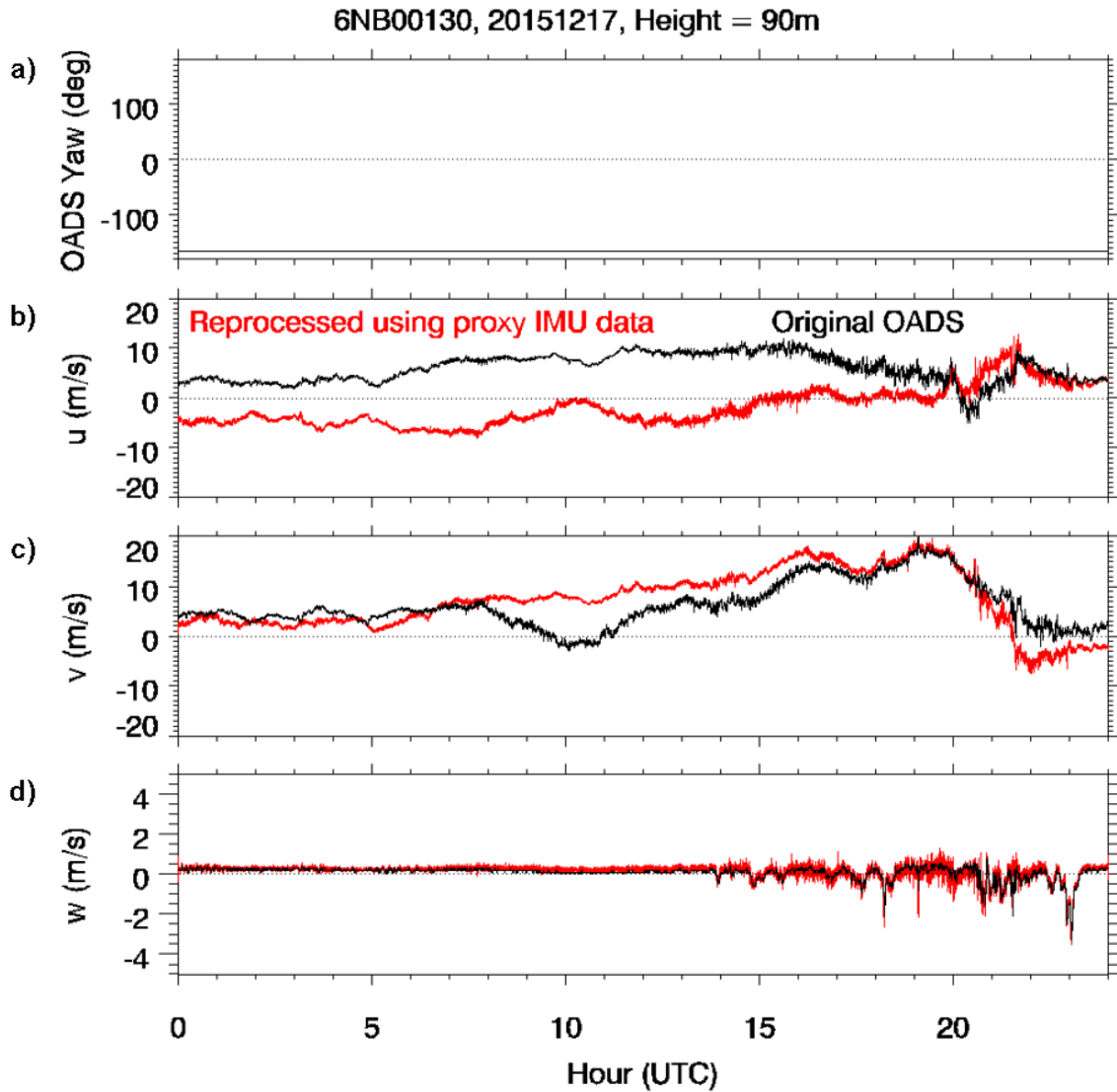


Figure 2.11. [Reprocessed 1 Hz winds (red curves) at the 90 m level for December 17, 2015. Panels a), b), c), and d) show the corrected OADS yaw angle, the eastward velocity component, the northward velocity component, and the vertical velocity component, respectively. The original OADS winds are shown in black.

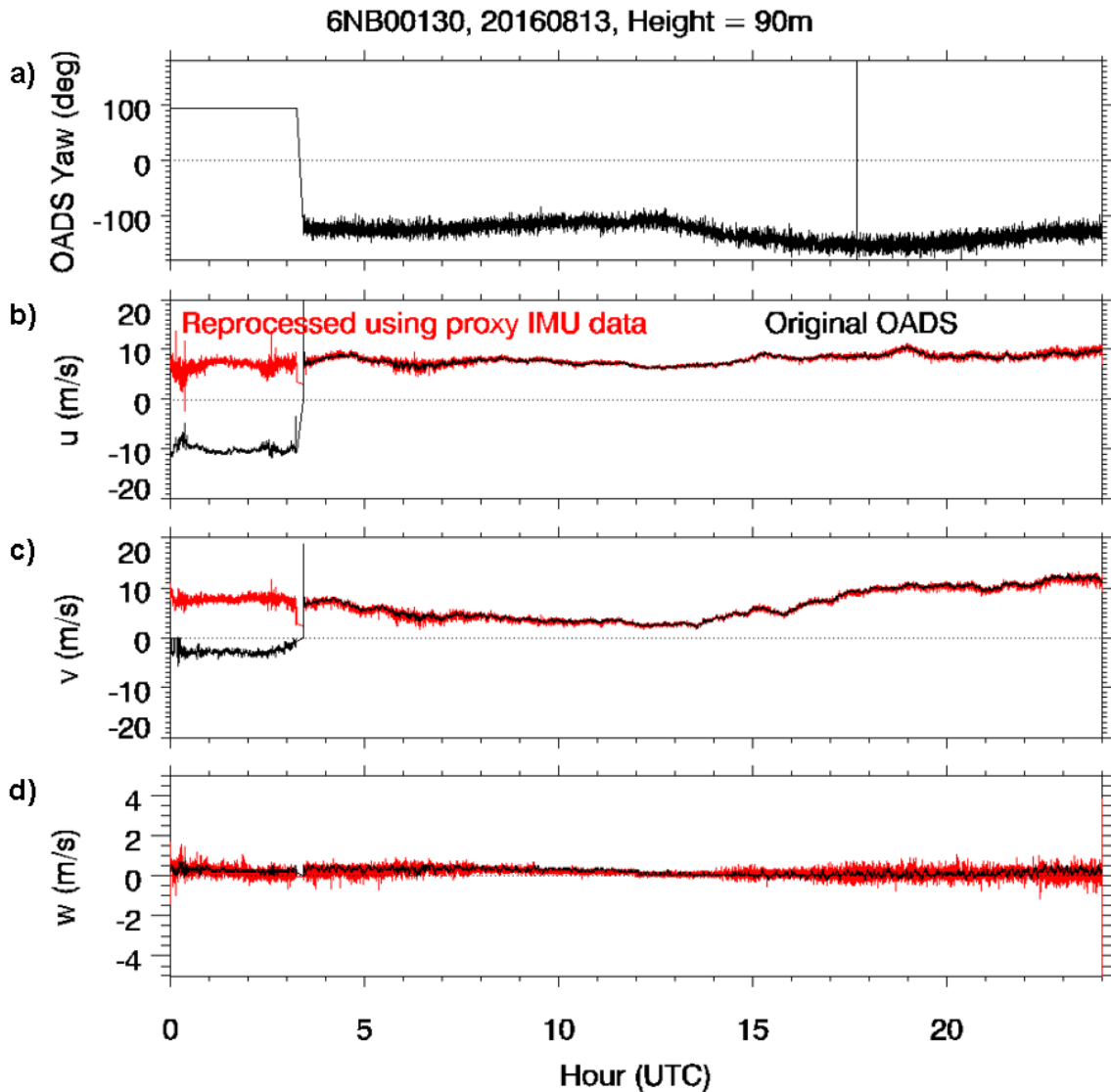


Figure 2.12. Reprocessed 1 Hz winds (red curves) at the 90 m level for August 13, 2016. Panels a), b), c), and d) show the corrected OADS yaw angle, the eastward velocity component, the northward velocity component, and the vertical velocity component, respectively. The original 1 Hz OADS winds are shown in black.

2.4 Average Winds

The reprocessed 1 Hz winds were averaged in time to generate separate datasets using 2-, 5-, and 10-minute averaging intervals. In addition to the mean winds, these datasets also include estimates of standard deviations of wind speed, wind direction, and vertical velocity. As noted previously, the 1 Hz winds are quite noisy, and this has a huge effect on estimates of variance. It appears that the OADS approach was to apply a smoothing filter prior to computing the statistical moments. The problem with this approach is that the smoothing affects both the signal and the noise, and the degree of smoothing is somewhat subjective. Despite this, the objective here is to simply match the 1 Hz OADS winds as closely as possible (during periods when the OADS IMU was functioning).

For this study, a box-car smoothing filter was applied to the reprocessed 1 Hz winds. Figure 2.13 shows how the root-mean-square error (RMSE) and correlation between the reprocessed and OADS winds changes as the width of the box-car smoothing filter is increased. As indicated in the figure, a smoothing width of about 30 s is required in order to achieve an RMSE less than 10 cm s^{-1} and a correlation greater than 0.9. Thus, a smoothing width of 30 s was applied to the reprocessed winds in this study.

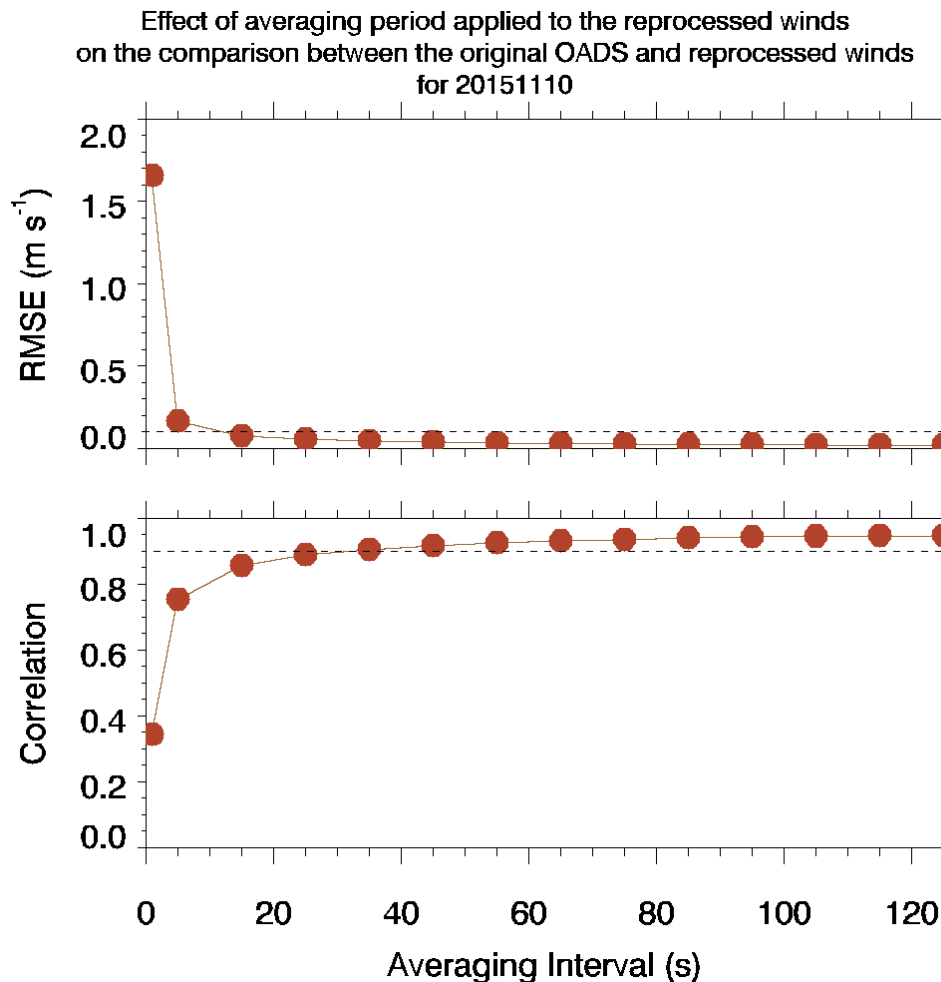


Figure 2.13. RMSE (*top*) and correlation (*bottom*) between the reprocessed and OADS 1 Hz winds as a function of the box-car averaging width. These results were computed using data obtained on November 11, 2015, at the 90 m level. Dashed lines in the figures represent thresholds discussed in the text above.

Figures 2.14 through 2.17 show 10-minute-averaged results for August 17, 2016. Figure 2.14 shows the wind speed, wind direction, vertical velocity, and data quality flags for the wind and platform attitude measurements.

Figure 2.15 shows the standard deviations in wind speed, wind direction, and vertical velocity. Figure 2.16

shows the mean yaw and the standard deviations in pitch and roll;
6NB00130 signal strength for 20160311

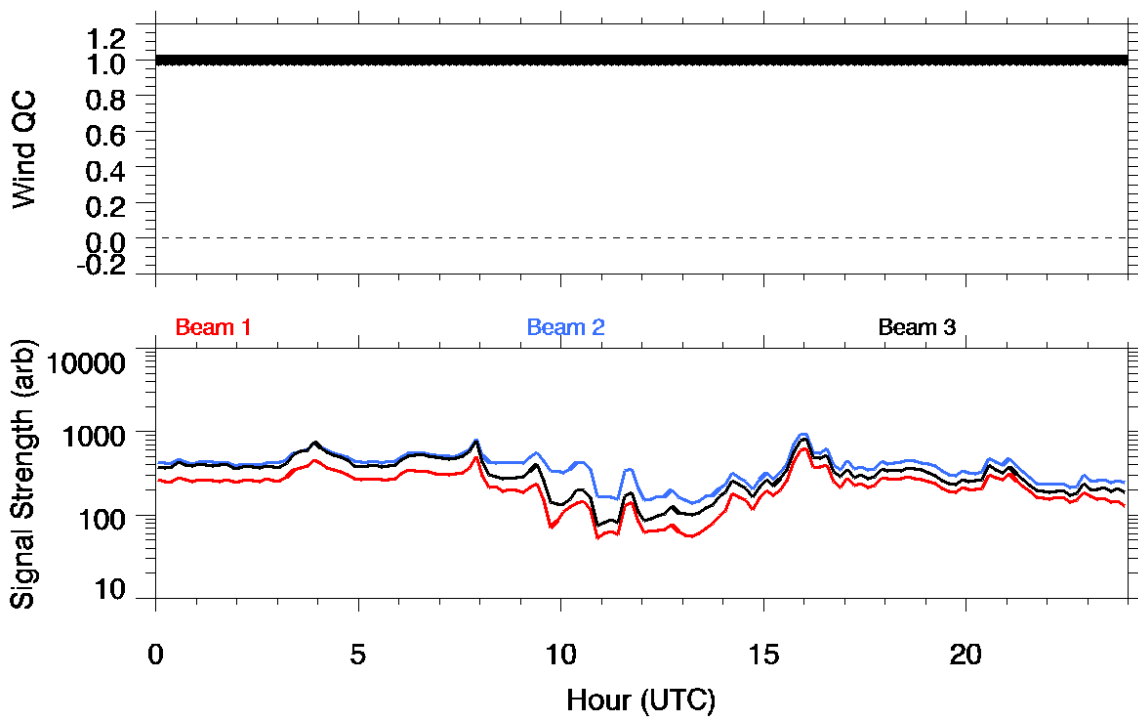


Figure 2.17 shows the mean signal strengths for each of the three beams.

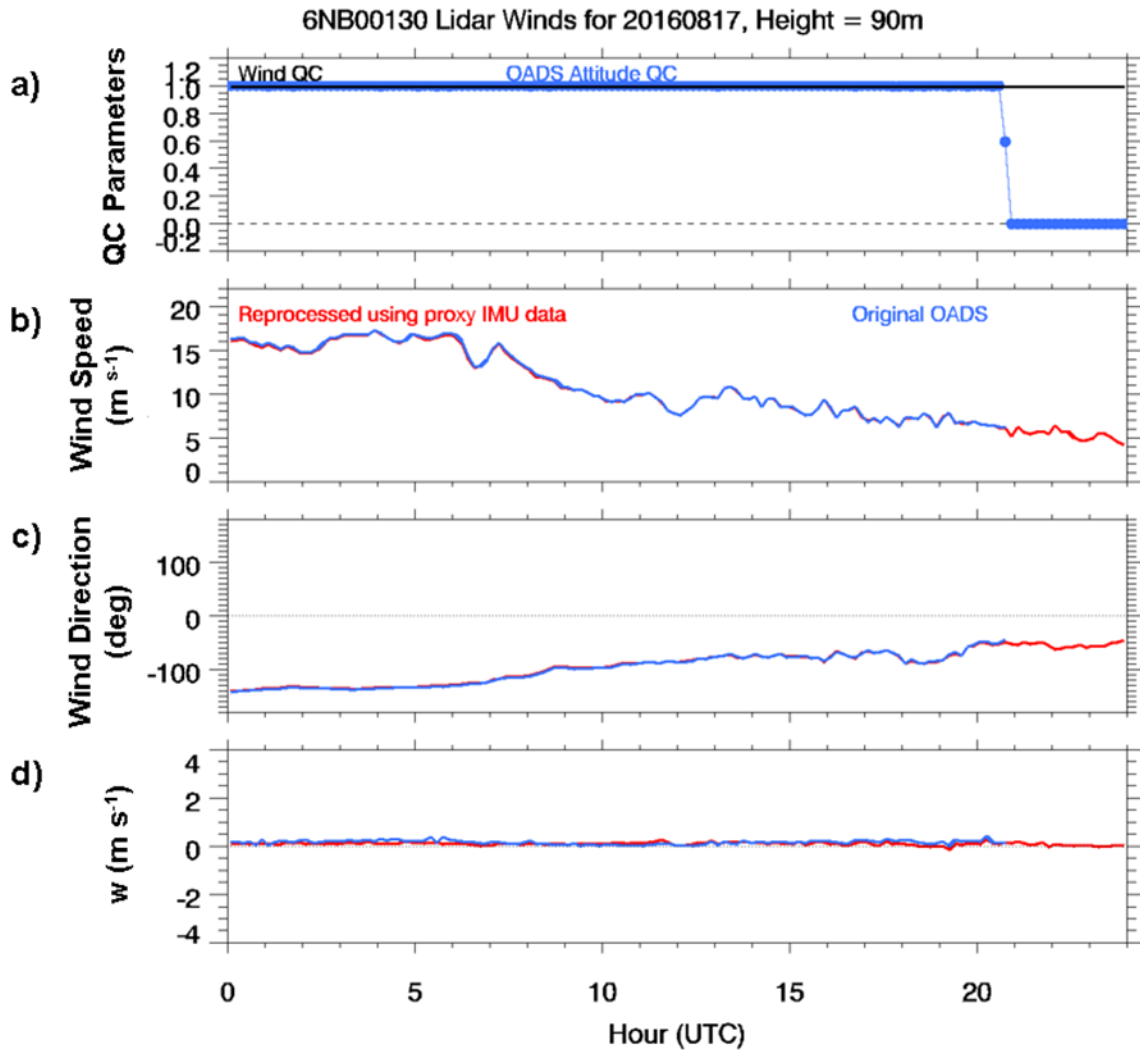


Figure 2.14. 10-minute results at the 90 m level for March 11, 2016. a) Data quality flags for wind measurements (black) and platform attitude measurements (blue). b) Reprocessed (red) and OADS (blue) wind speeds. c) Reprocessed (red) and OADS (blue) wind directions. d) Reprocessed (red) and OADS (blue) vertical velocity. RMSE difference (*top*) and correlation (*bottom*) between the reprocessed and OADS 1 Hz winds as a function of the box-car averaging width. These results were computed using data obtained on November 11, 2015, at the 90 m level.

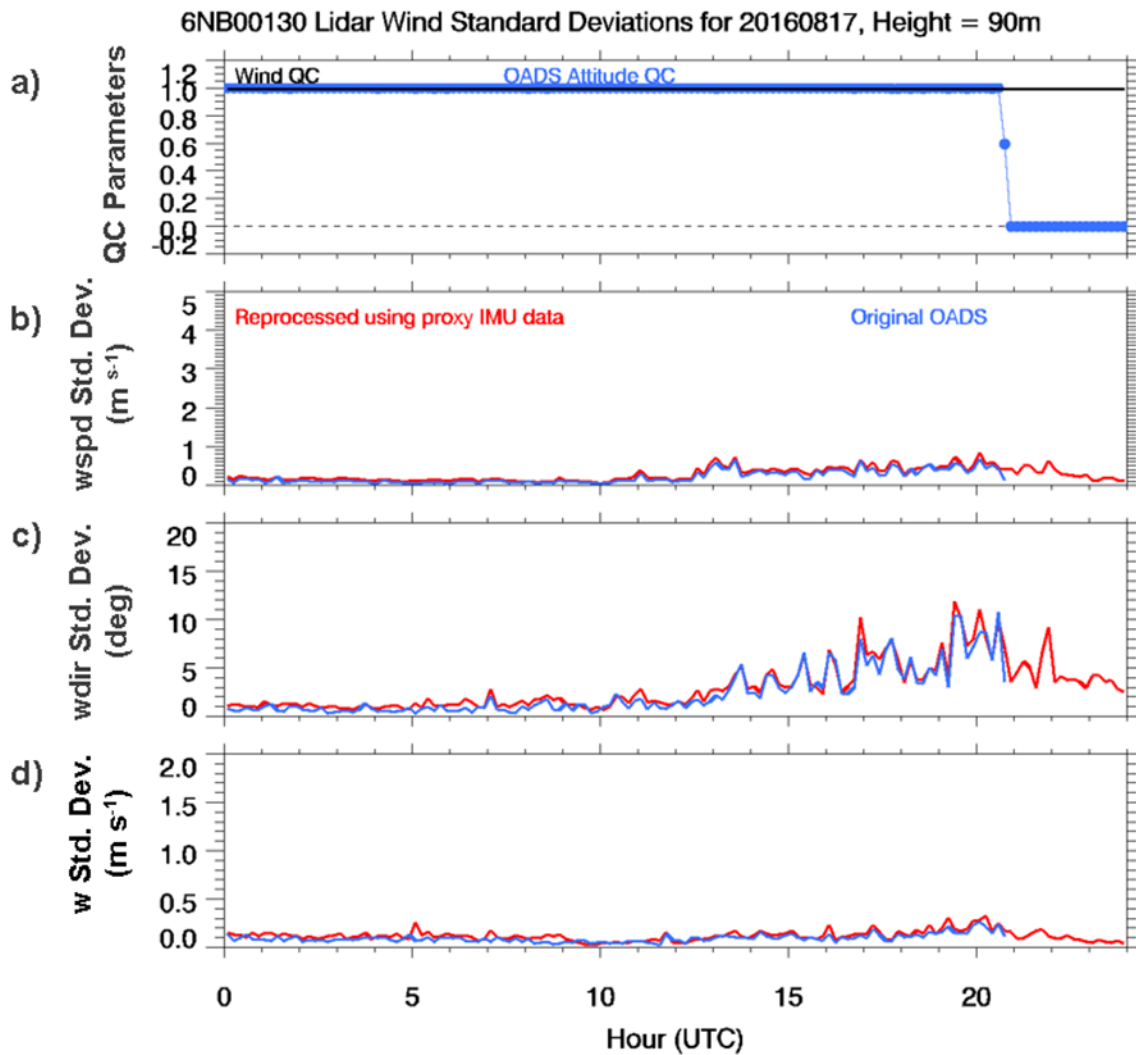


Figure 2.15. 10-minute results at the 90 m level for March 11, 2016. a) Data quality flag platform attitude measurements (blue). b) Reprocessed (red) and OADS (blue) wind speed standard deviations. c) Reprocessed (red) and OADS (blue) wind direction standard deviations. d) Reprocessed (red) and OADS (blue) vertical velocity standard deviations.

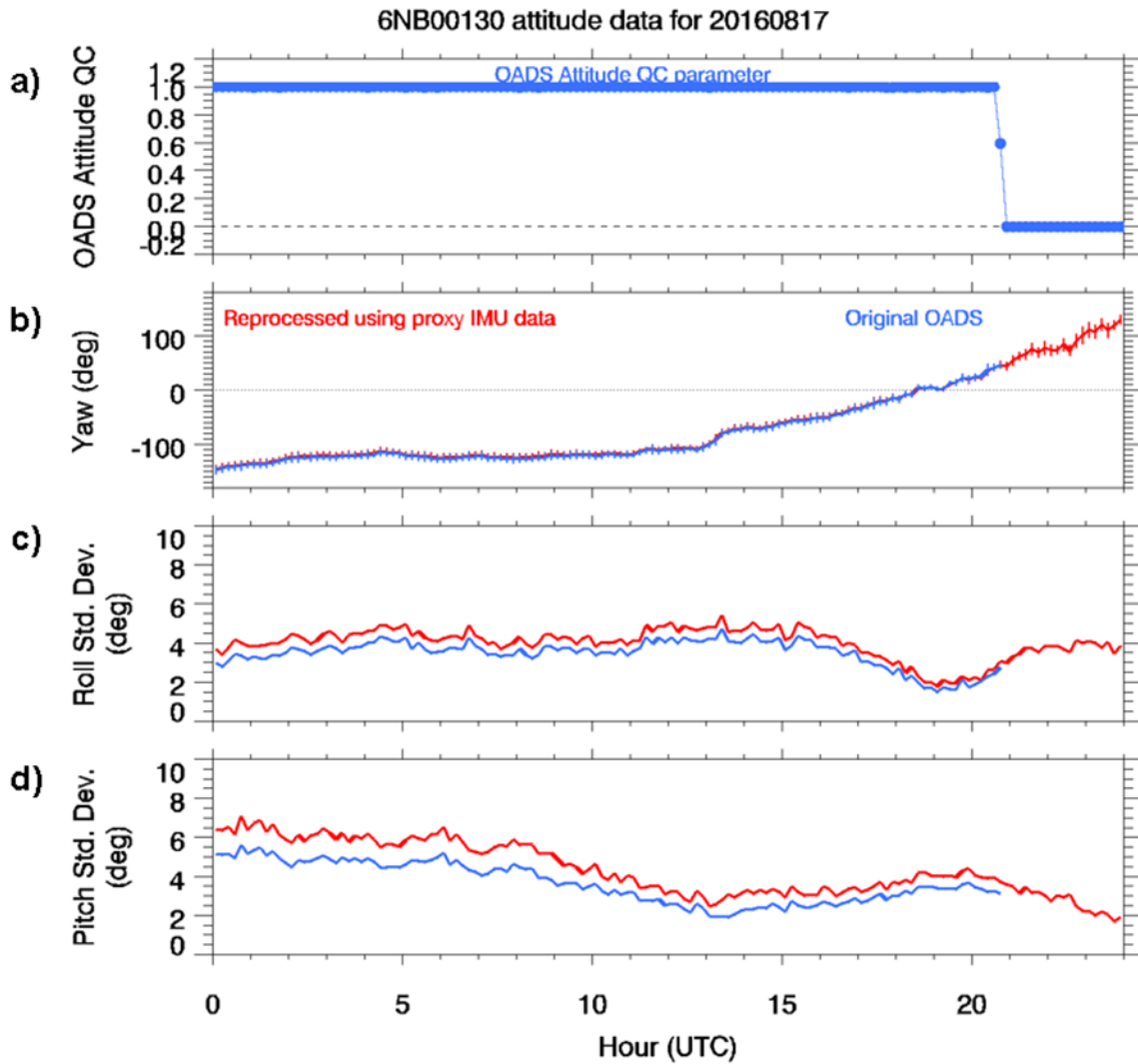


Figure 2.16. 10-minute results at the 90 m level for March 11, 2016. a) Data quality flag platform attitude measurements (blue). b) Proxy (red) and OADS (blue) yaw angle. c) Proxy (red) and OADS (blue) roll standard deviations. d) Proxy (red) and OADS (blue) pitch standard deviations.

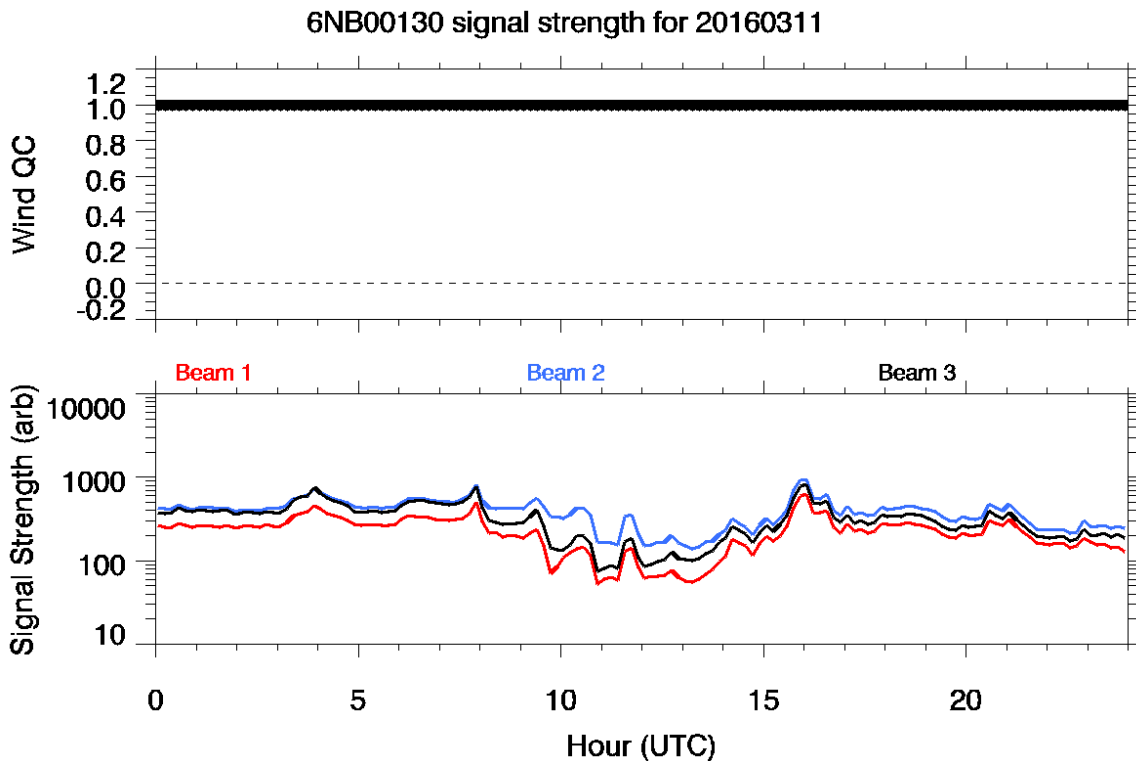


Figure 2.17. Data quality flag for wind measurements (*top*) and lidar signal strengths at 90 m for each of the three beams (*bottom*).

2.5 Summary

The goal of this work was to recover winds that were corrupted by the failure of the Vindicator's internal IMU during the New Jersey deployment from November 6, 2015, until February 7, 2017. The approach was to substitute valid IMU data from the AXYS buoy to perform motion compensation. This required first determining the offsets in roll, pitch, and yaw between the Vindicator and AXYS attitude measurements. Once determined, these offsets were added to the AXYS roll, pitch, and yaw measurements to generate proxy attitude data that was then used to perform motion compensation on the 1 Hz measurements. The reprocessed 1 Hz winds were then averaged in time to yield 2-, 5-, and 10-minute-averaged winds. NetCDF file formats for reading 1 Hz and averaged reprocessed wind profiles are provided in Appendices A and B.

3.0 Basic Climatology of Wind and Other Meteorological Variables

3.1 Overview of Meteorological Instrumentation

Historically, offshore atmospheric observations have been concentrated near the surface. The WindSentinel buoys were equipped with a suite of instruments (see Table 1.1) to simultaneously probe atmospheric conditions near the surface and at higher levels that are especially relevant to the wind energy industry. The following sections discuss the trends in wind speed, wind direction, temperature, pressure, and relative humidity throughout the deployments and in accordance with seasonality and the diurnal cycle.

3.2 Hub-Height Analysis – Wind

The lidars aboard the buoys provide wind information at 90 m, a hub height commonly used by the wind energy industry. The following discussion provides an analysis of wind speed and direction at this level by season, time of day, stability class, and for the entire deployment period. We note that the New Jersey lidar information used in this examination is the reprocessed version produced by PNNL described in Section 2.3.1, and that the directions have been corrected to true north by subtracting 11.3° from the Virginia directions and 12.4° from the New Jersey directions.

Figure 3.1 shows the distributions of 90 m wind speeds for the Virginia and New Jersey buoys, respectively, for the duration of each deployment. The Virginia hub-height data shows more variability in the wind speeds than does the New Jersey data at the same level; however, it is noted that the deployments covered sequential years with modest overlap and that different seasons were sampled twice in the respective deployments.

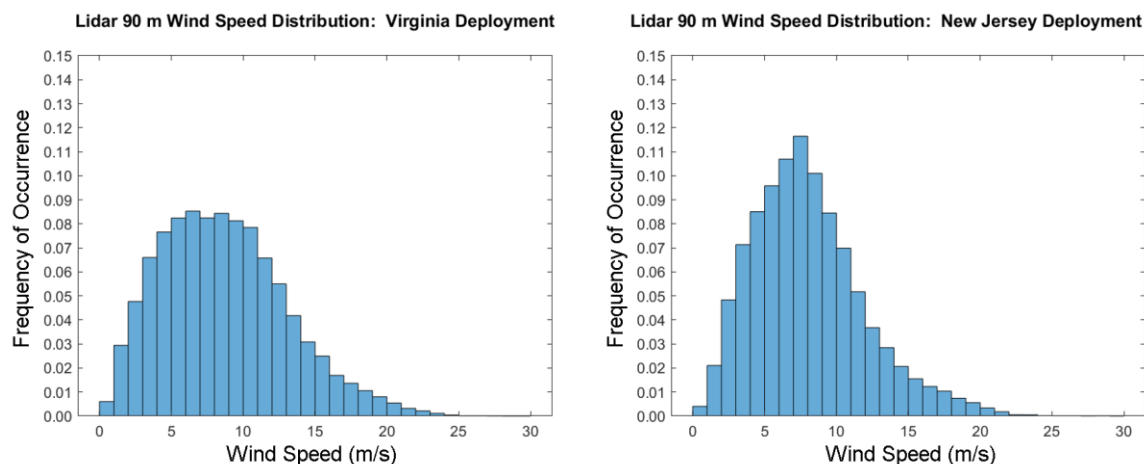


Figure 3.1. 90 m wind speed distributions for the Virginia and New Jersey deployments.

The hub-height wind roses for each deployment are depicted in Figure 3.2. The Virginia wind distribution is bimodal, with winds coming mainly from the south-southwest and north. The New Jersey winds are primarily sourced from the northwest and southwest, with secondary components from the north-northwest and east-northeast.

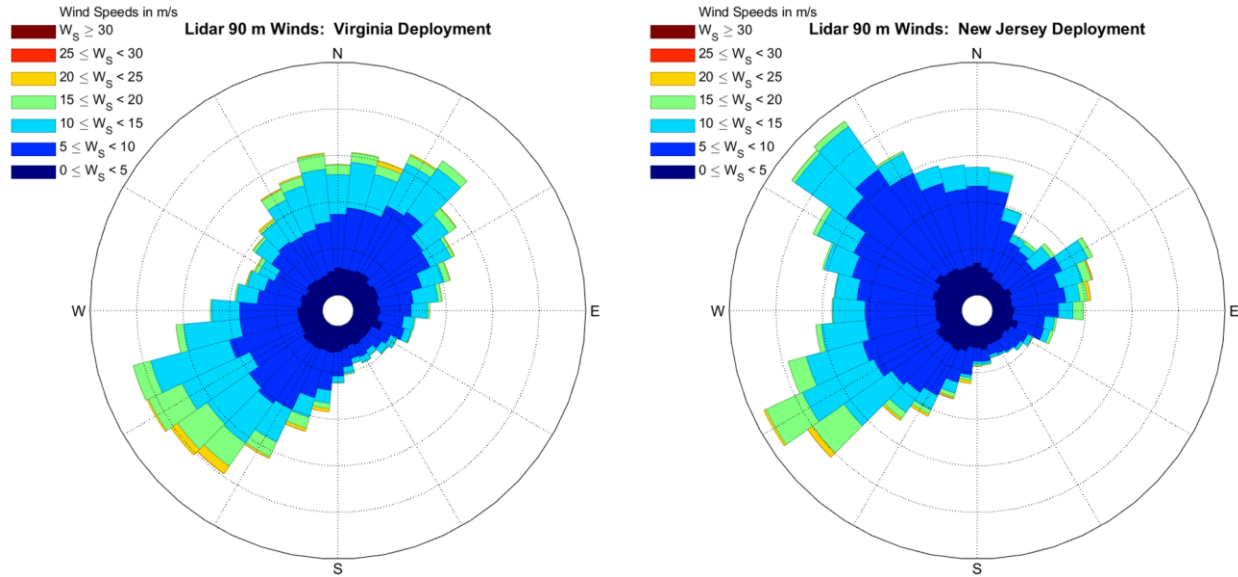


Figure 3.2. 90 m wind speed and direction distributions for the Virginia and New Jersey deployments.

Despite their distinct locations, temporal coverages, and distances from the shoreline, the Virginia and New Jersey sites show very similar seasonal hub-height wind speed patterns, as shown in Figure 3.3. Both locations have mean wind speed maxima in the winter and minima in the summer. The seasonal spread of the wind speeds is depicted in the box plots in Figure 3.4. Including outliers, the month of largest degree of dispersion for Virginia is February and January for New Jersey.

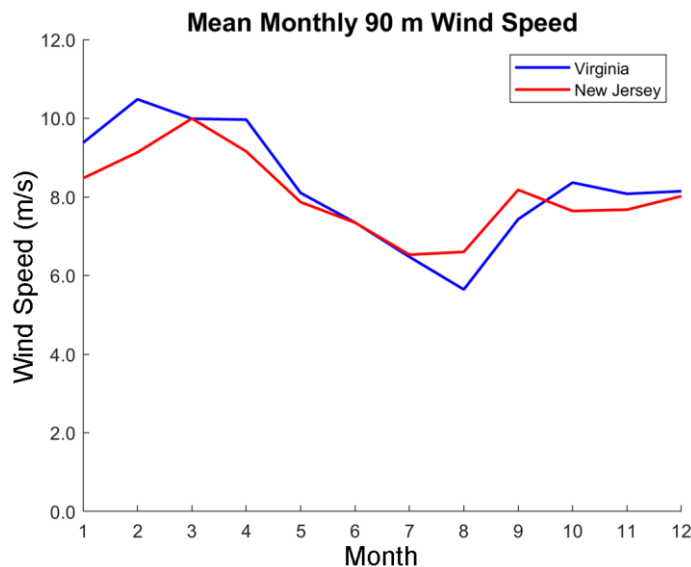


Figure 3.3. Mean monthly 90 m wind speeds for the Virginia and New Jersey deployments. The Virginia deployment covered two winters and springs, and one summer and fall, from December 2014–May 2016. The New Jersey deployment covered two winters and one spring, summer, and fall, from November 2015–February 2017.

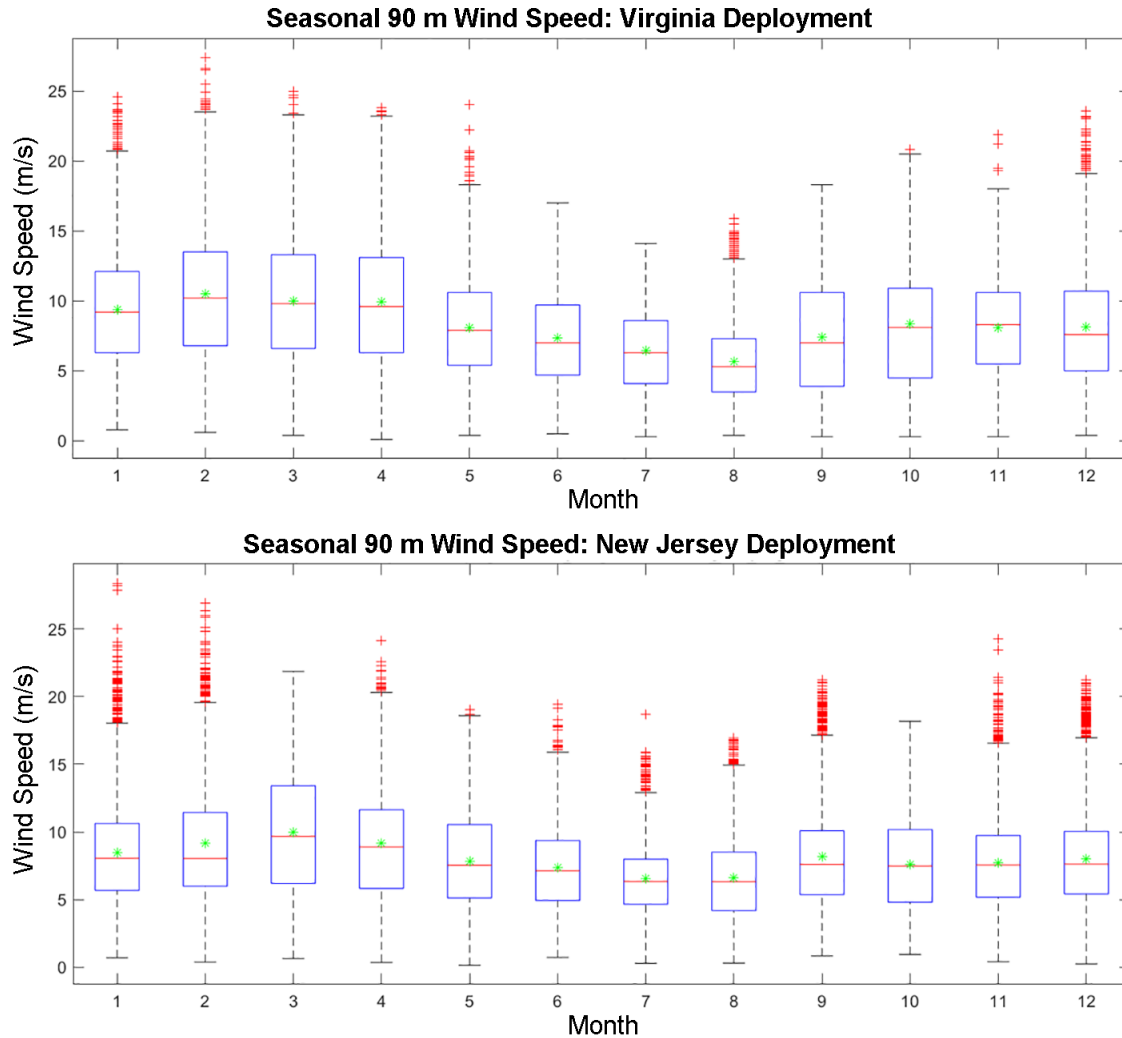


Figure 3.4. Seasonal spread in hub-height wind speeds for Virginia and New Jersey.

Figure 3.5 shows the seasonal evolution of hub-height wind direction as reported by the Virginia buoy. The winter Virginia winds are north-northwesterly, with a secondary southwesterly component. In spring, the south-southwesterly winds become dominant, with a smaller north-northeasterly component. The summer dominant directions are similar to those of spring, with slower wind speeds and more directional diversity in the southwest quadrant. Fall winds at the Virginia buoy have a northeasterly dominance.

The seasonal transition of hub-height wind direction at the New Jersey buoy is shown in Figure 3.6. Winter is characterized by northwesterly winds, which transition to southwesterly with a northeastern secondary component in spring. Summer winds are southwesterly, and northwesterly to a lesser degree. Fall winds cover all quadrants except the southeast.

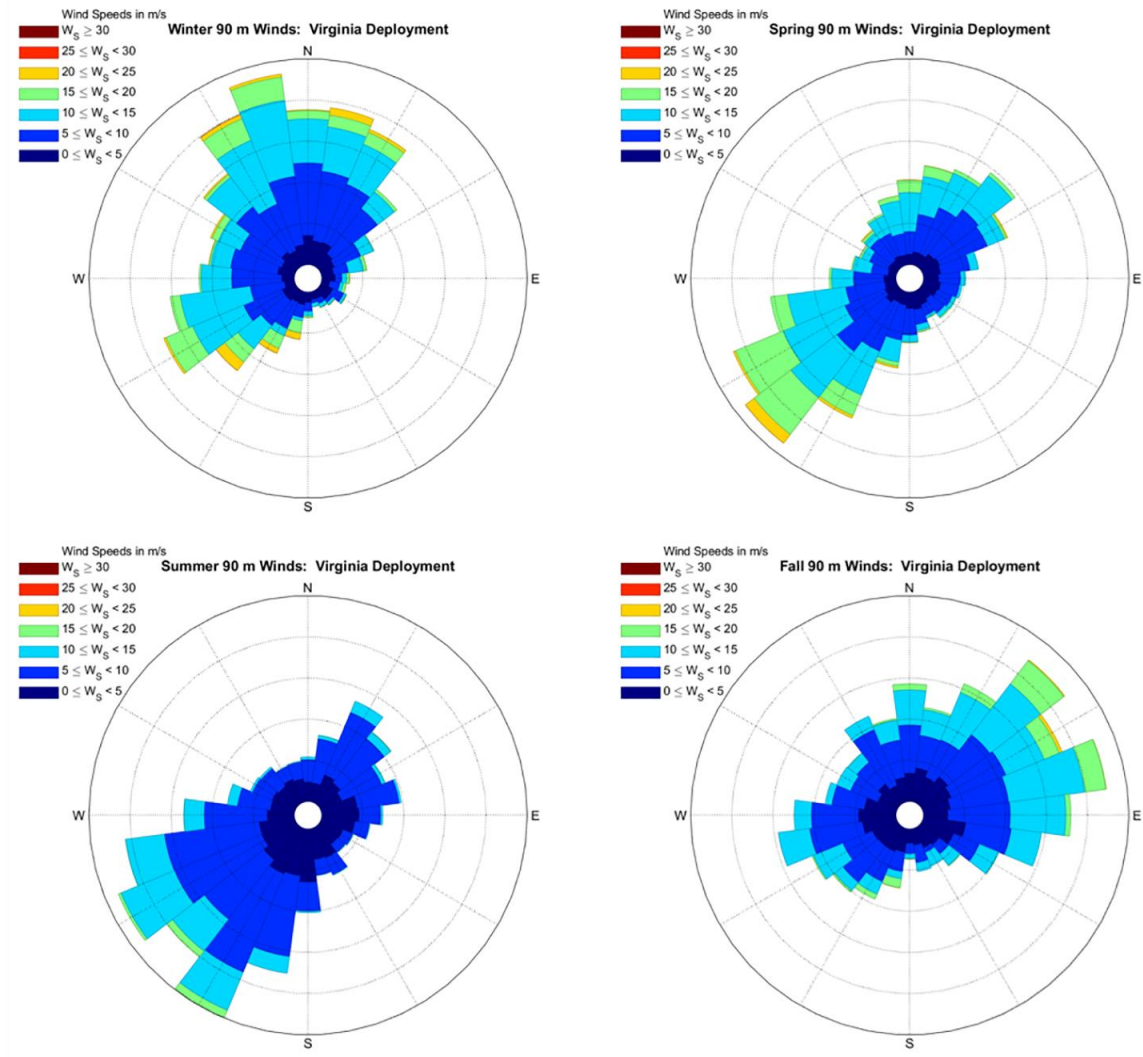


Figure 3.5. Seasonal wind roses for the Virginia deployment.

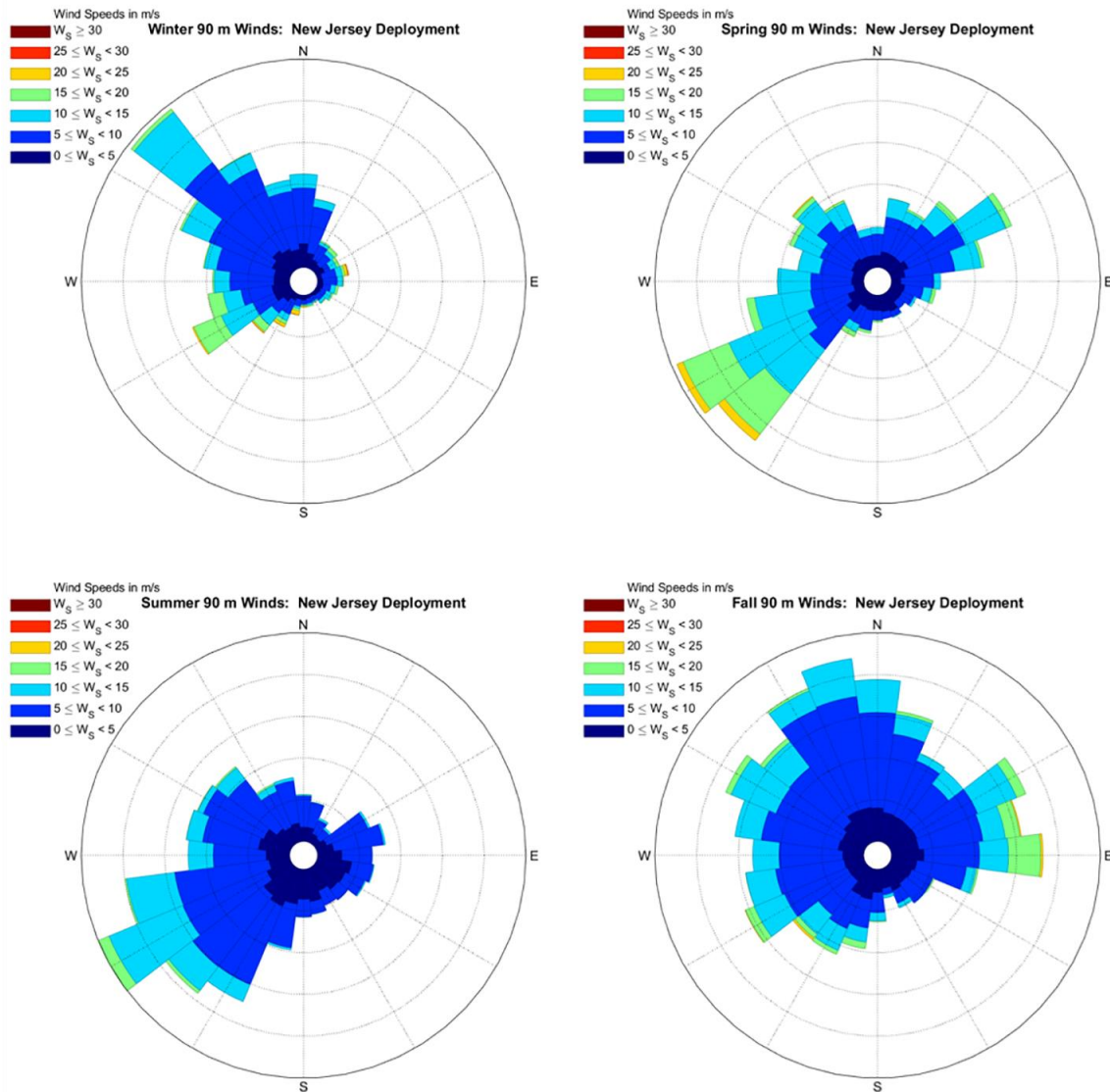


Figure 3.6. Seasonal wind roses for the New Jersey deployment.

The diurnal hub-height wind speed averages and boxplots are displayed in Figures 3.7 and 3.8, respectively. Both deployment locations fell within the Eastern Time Zone; therefore, local noon is at 16 or 17 UTC, depending on time of year, and local midnight is at 4 or 5 UTC. The average wind speed minimum for New Jersey occurs earlier in the day than for Virginia.

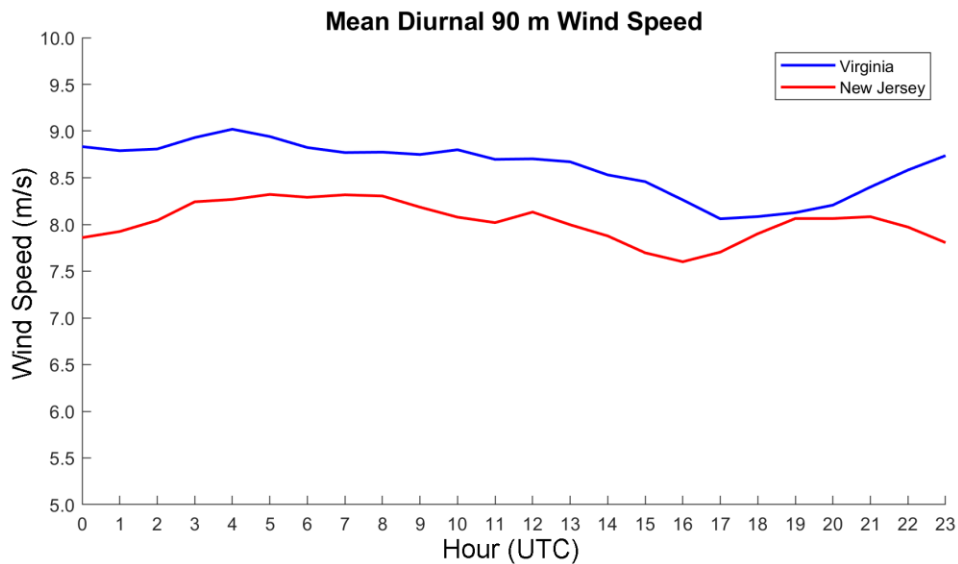


Figure 3.7. Average diurnal hub-height wind speed for Virginia and New Jersey deployments.

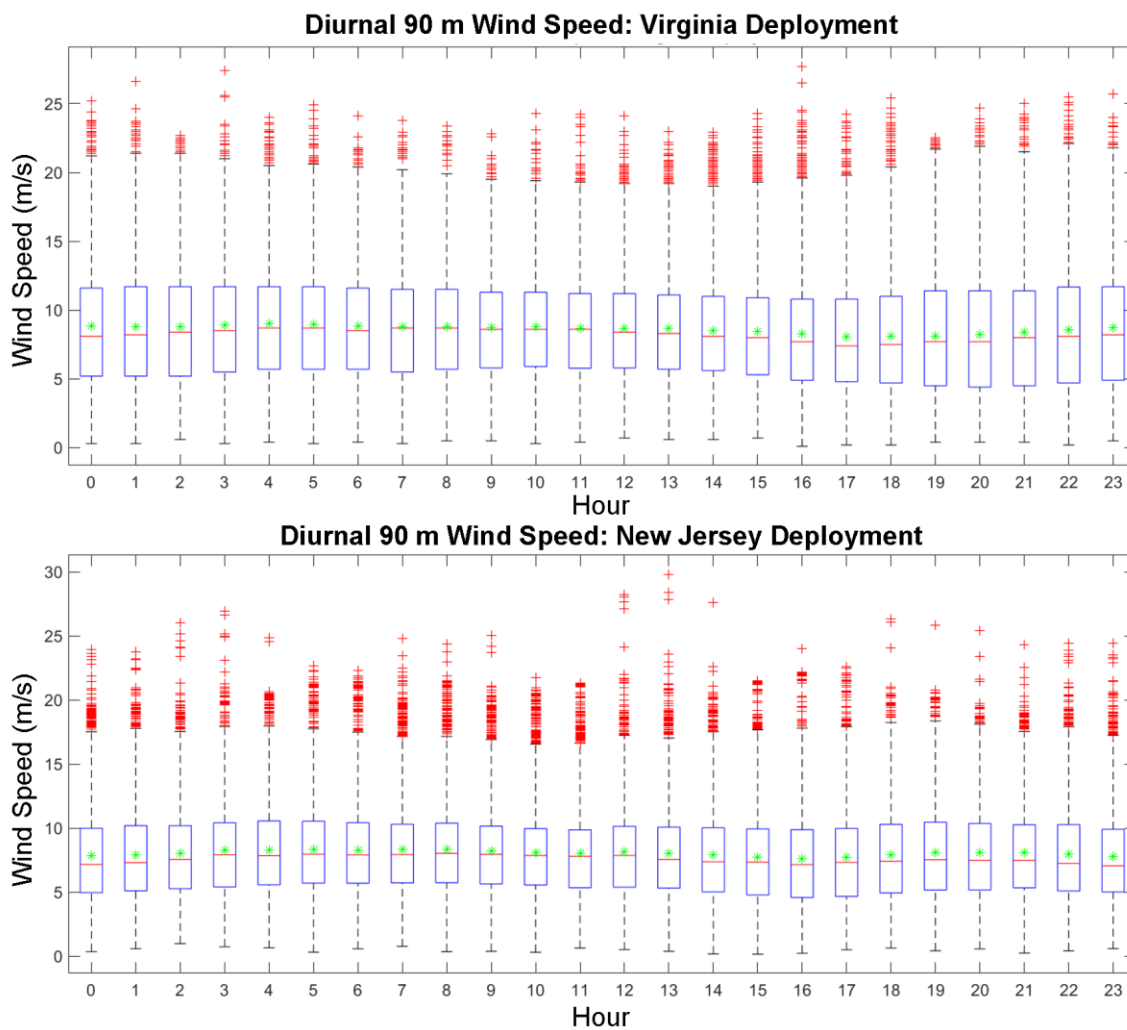


Figure 3.8. Diurnal spread in hub-height wind speeds for Virginia and New Jersey.

Finally, the hub-height winds can be analyzed according to the stability of the atmosphere, a measure of atmospheric tendency to encourage or discourage vertical motion. The turbulent fluxes of heat and momentum were estimated by applying the bulk parameterization methodology of Woods Hole Oceanographic Institute, a simplified version of the Fairall et al. (1996) Tropical Ocean-Global Atmosphere Coupled-Ocean Atmosphere Response Experiment (TOGA/COARE) algorithm, to the near-surface buoy atmospheric and oceanographic measurements (https://woodshole.er.usgs.gov/operations/sea-mat/air_sea.html/index.html). Stability limits were defined as follows, using the 4 m measurement height as z : unstable for $z/L < -0.1$, neutral for $|z/L| \leq 0.1$, and stable for $z/L > 0.1$. z/L is discussed more fully in Section 6.0. Figure 3.9 shows that, for each deployment location, the dominant stability class is neutral, followed by unstable, and finally stable.

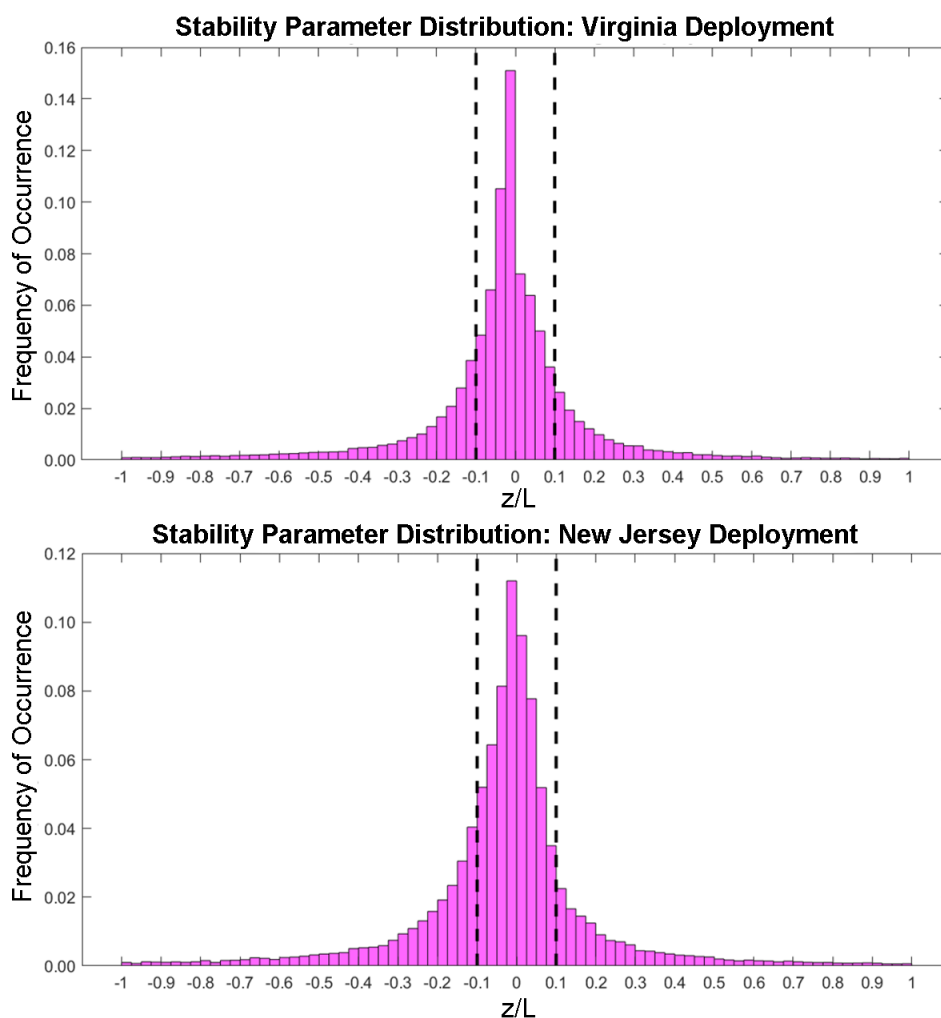


Figure 3.9. Distribution of the stability parameter for $z = 4$ m for the Virginia and New Jersey deployments.

The hub-height wind speed distributions are broken out by stability class in Figure 3.10. Unstable cases for both locations produce narrow distributions of lower wind speeds due to a well-mixed boundary layer resulting in minimal shear. The neutral and stable cases show more variability in the hub-height speeds.

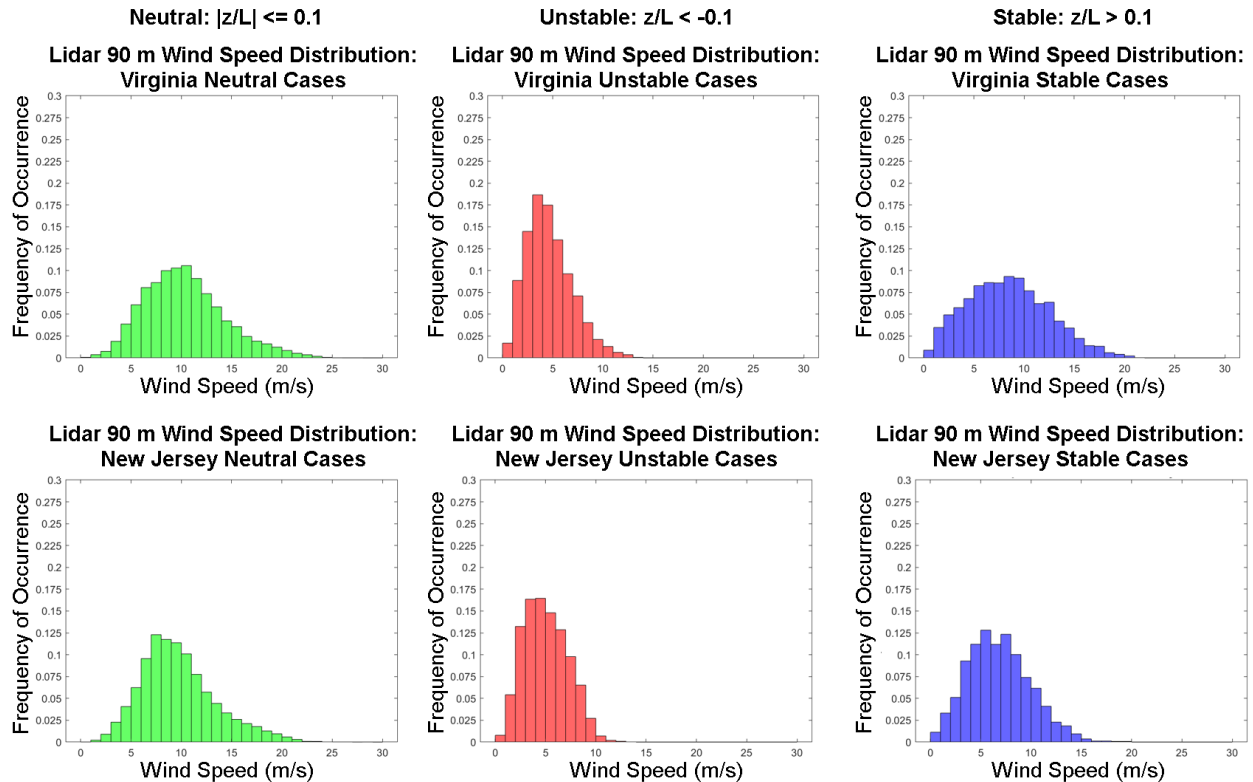


Figure 3.10. Hub-height winds speed distributions by stability class.

3.3 Near-Surface Analysis

Meteorological instruments at 4 m provide a complementary study to the flow at hub height. The following discussion provides an analysis of the near-surface wind speed, direction, temperature, pressure, and relative humidity. We again note that the directions have been corrected to true north by subtracting 11.3° from the Virginia directions and 12.4° from the New Jersey directions.

3.3.1 Wind

The 4 m wind speed distributions for Virginia and New Jersey are very similar, as shown in Figure 3.11. The corresponding wind roses follow in Figure 3.12. The New Jersey wind direction distribution at 4 m is quite similar to the corresponding hub-height distribution in Figure 3.2, primarily southwesterly and northwesterly with a northeasterly secondary component. The Virginia 4 m wind directions differ from the 90 m directions in that the bimodal distribution is northeasterly and southerly, instead of northerly and south-southwesterly.

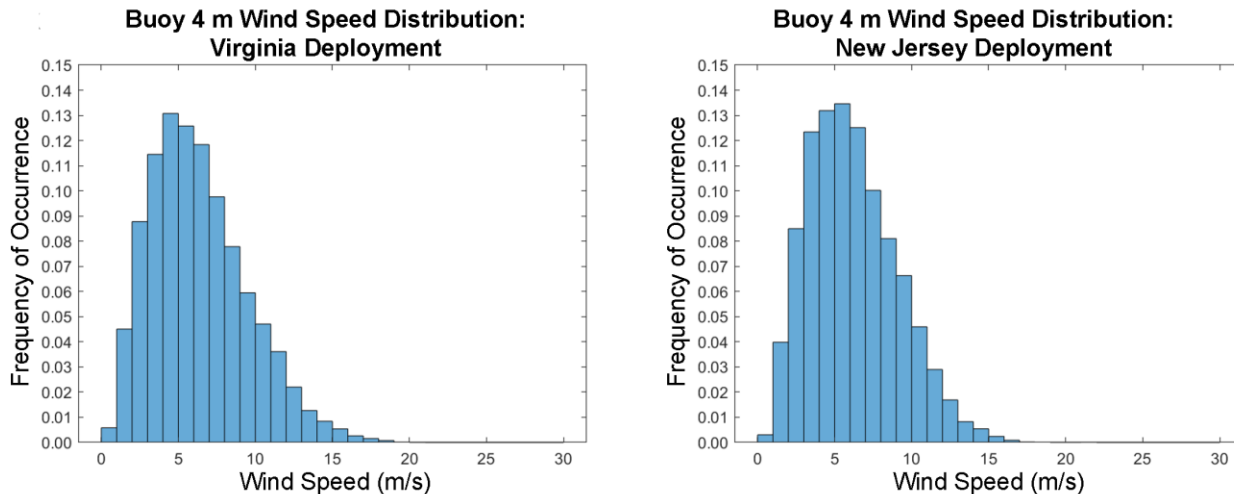


Figure 3.11. Near-surface wind speed distributions for the Virginia and New Jersey deployments.

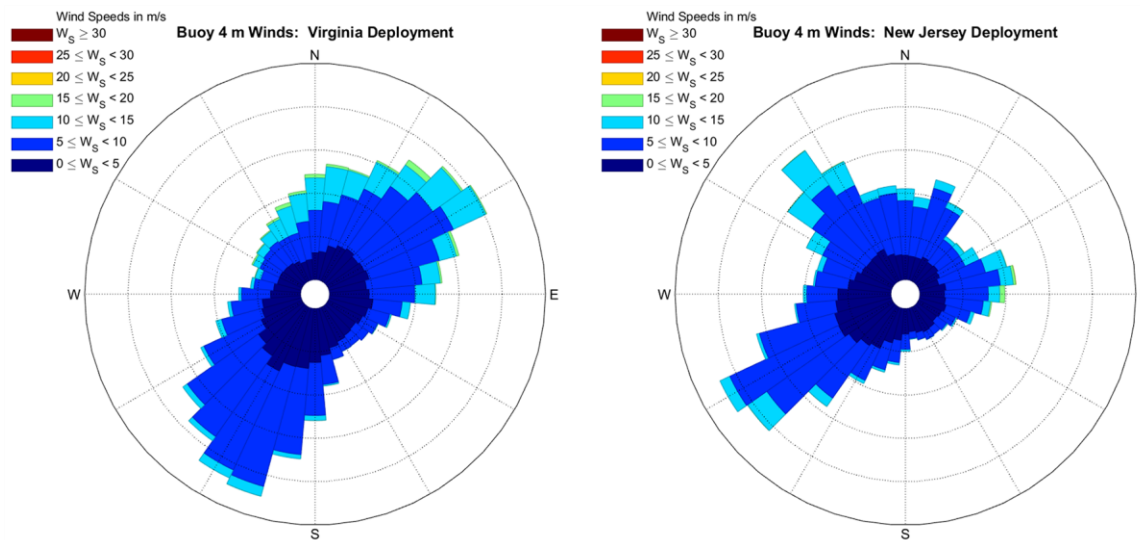


Figure 3.12. Near-surface wind roses for the Virginia and New Jersey deployments.

The seasonally-averaged wind speeds for each site show similar patterns of peak winds in winter and minimum speeds in summer as shown in Figures 3.13 and 3.14.

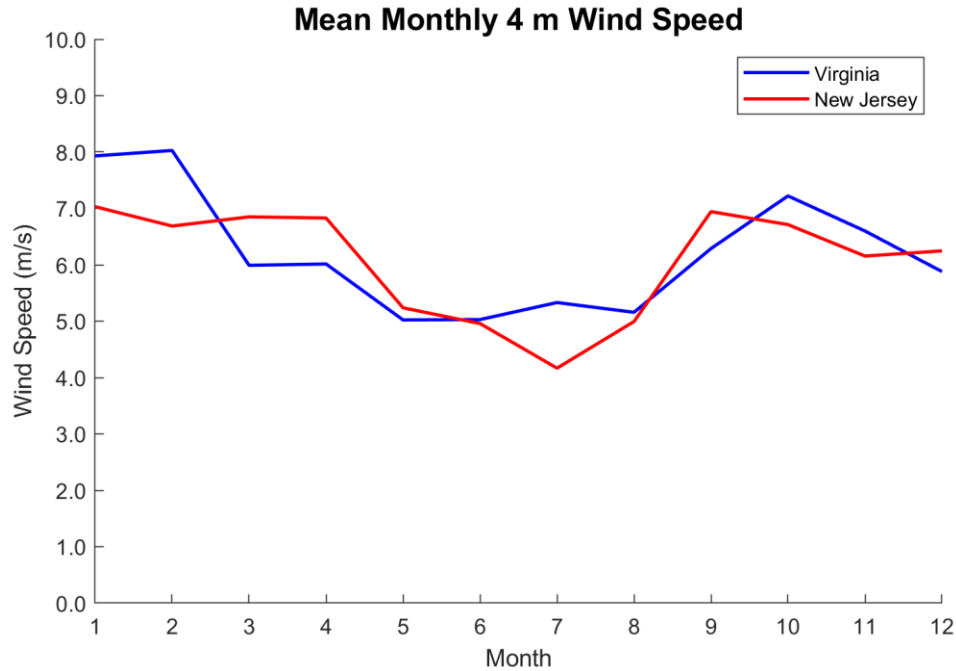


Figure 3.13. Near-surface monthly wind speeds for Virginia and New Jersey.

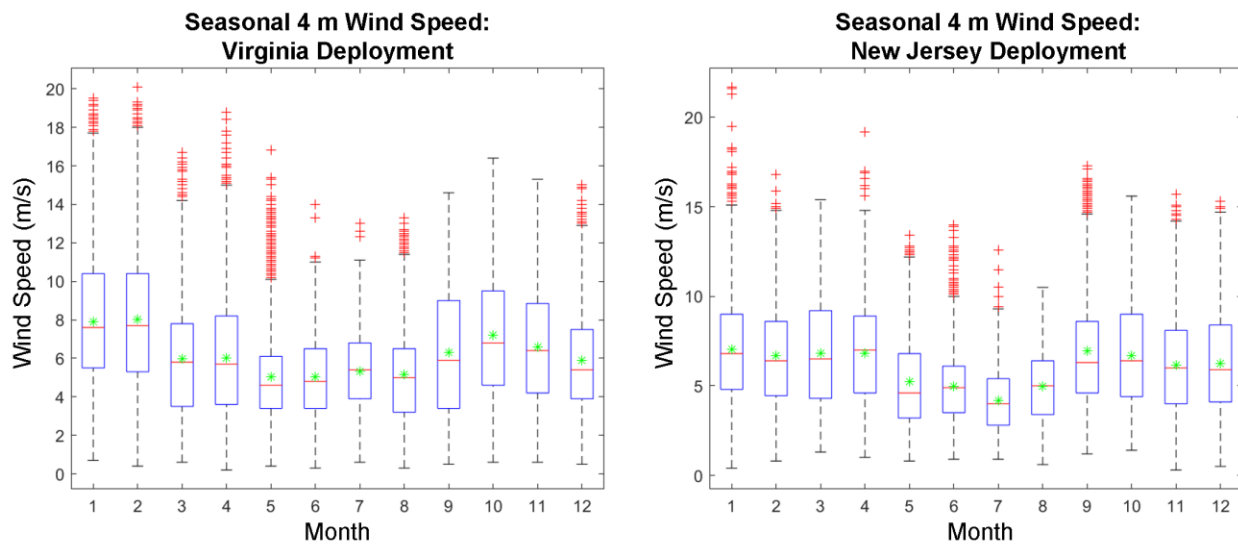


Figure 3.14. Spread in near-surface wind speeds for Virginia and New Jersey, respectively.

The seasonal evolution of the near-surface Virginia winds is shown in Figure 3.15. In the winter, strong winds come from the northern quadrant, with a secondary and slower component coming from the south. By spring the fastest winds are still coming from the northeast and north, though the frequency is reduced. A larger amount of the wind is sourced from the south. This southerly trend continues through the summer, with just a small component coming from the northeast. The fall near-surface flow is dominated by northeasterly winds.

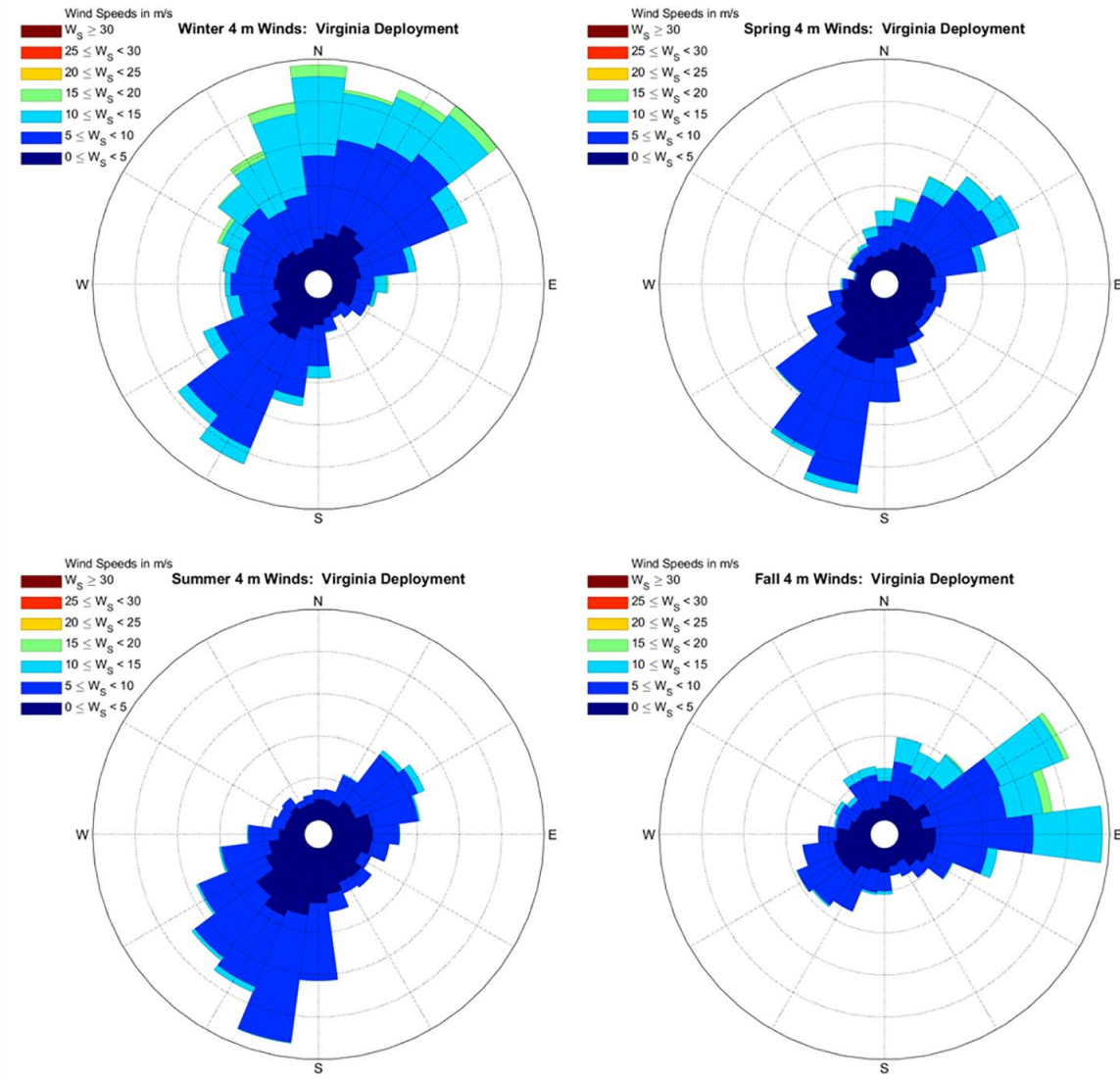


Figure 3.15. Seasonal distribution of near-surface wind for the Virginia deployment.

The seasonal analysis of near-surface wind directions for the New Jersey buoy follows in Figure 3.16. Winter has the majority of winds coming from the northwest, with smaller contributions coming from the southwest and north. Spring winds are dominated by southwesterly flow, with a smaller component coming from the northeast. Slower summer winds are sourced from the southwest. Fall has the most variability in wind direction, with winds well-represented in all quadrants except the southeast.

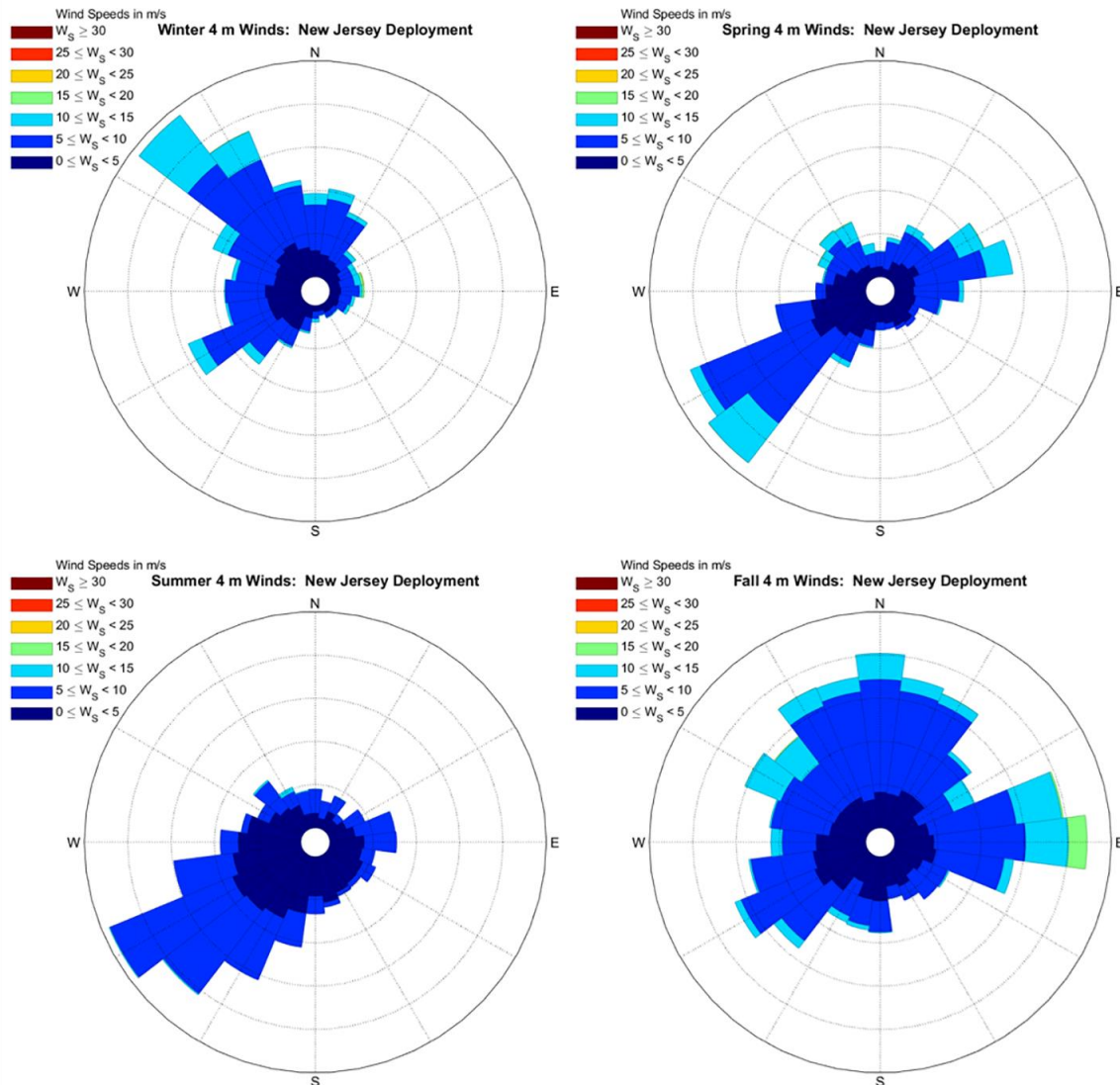


Figure 3.16. Seasonal distribution of near-surface wind for the New Jersey deployment.

The average near-surface wind speeds for both buoys do not show much variability diurnally as seen in Figures 3.17 and 3.18. The difference between the fastest and slowest diurnally-averaged wind speeds is only 0.5 m/s for both locations. The Virginia near-surface diurnal trend is similar to its hub-height counterpart: the slowest winds occur around local noon (17 UTC). Conversely, the New Jersey near-surface diurnal wind pattern has the slowest wind speeds occurring before dawn, which diverges from the pattern of the hub-height winds. In addition, the difference at 90 m in Figure 3.7 seems to be more systematic than at the surface. It is not clear whether this is due to stratification differences, coastal circulations, or some other cause.

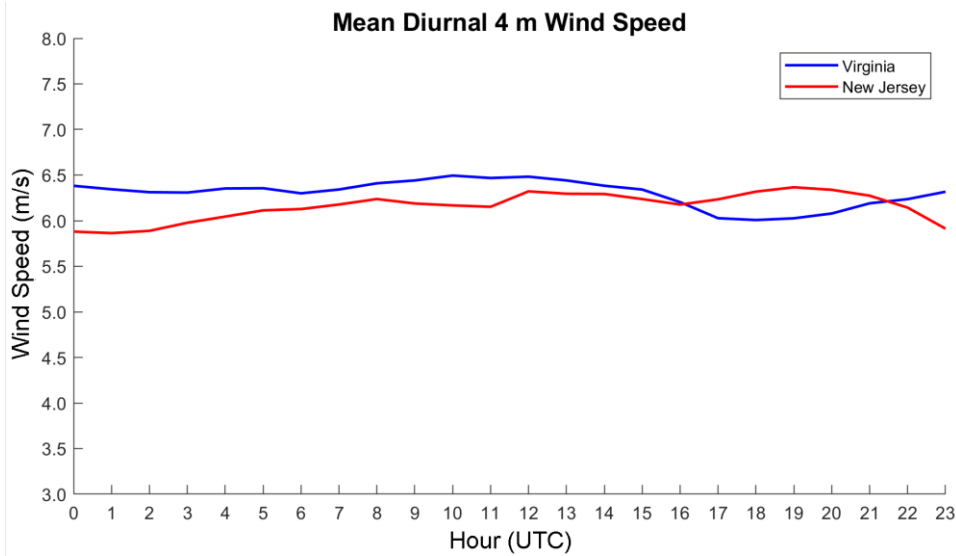


Figure 3.17. Diurnally-averaged near-surface wind speeds for Virginia and New Jersey.

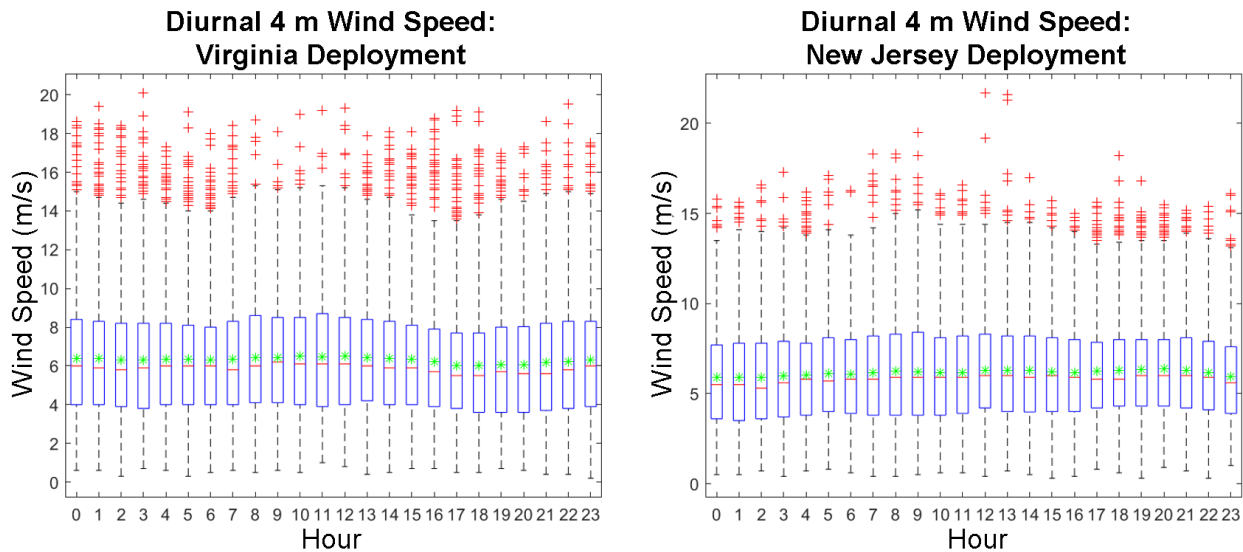


Figure 3.18. Diurnal spread in near-surface wind speeds for Virginia and New Jersey.

The near-surface wind speed distributions broken out by stability class are seen in Figure 3.19. Comparing the shape of the 4 m distributions to their 90 m counterparts, the near-surface unstable distributions are similar, the neutral are slightly narrower, and the stable are much narrower. This shows that under unstable conditions the wind shear is small and under stable conditions the wind shear is high, as expected. Figure 3.20 further illustrates this concept, showing the difference between hub-height and near-surface wind speeds as a function of the stability parameter z/L . For both sites, large values of wind shear are associated with stable conditions and minimal values of shear occur for unstable conditions.

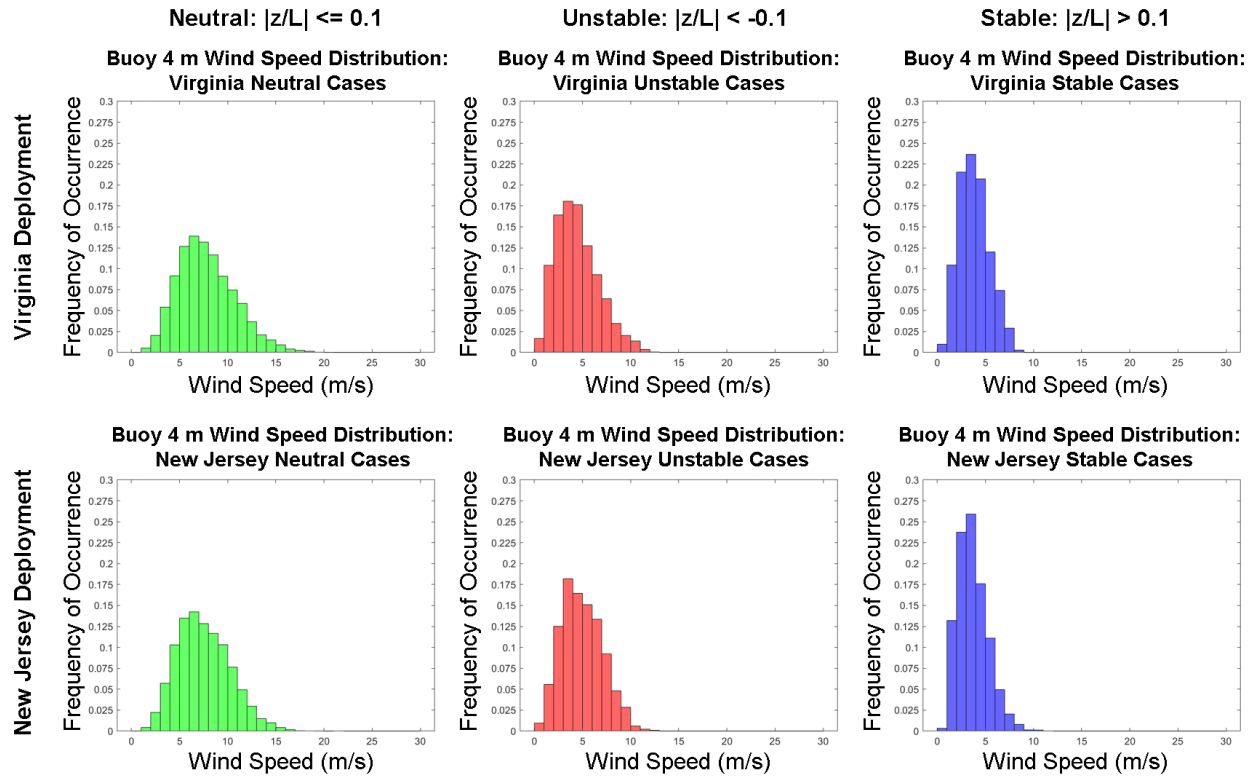


Figure 3.19. Near-surface wind speed distributions by stability class for Virginia and New Jersey.

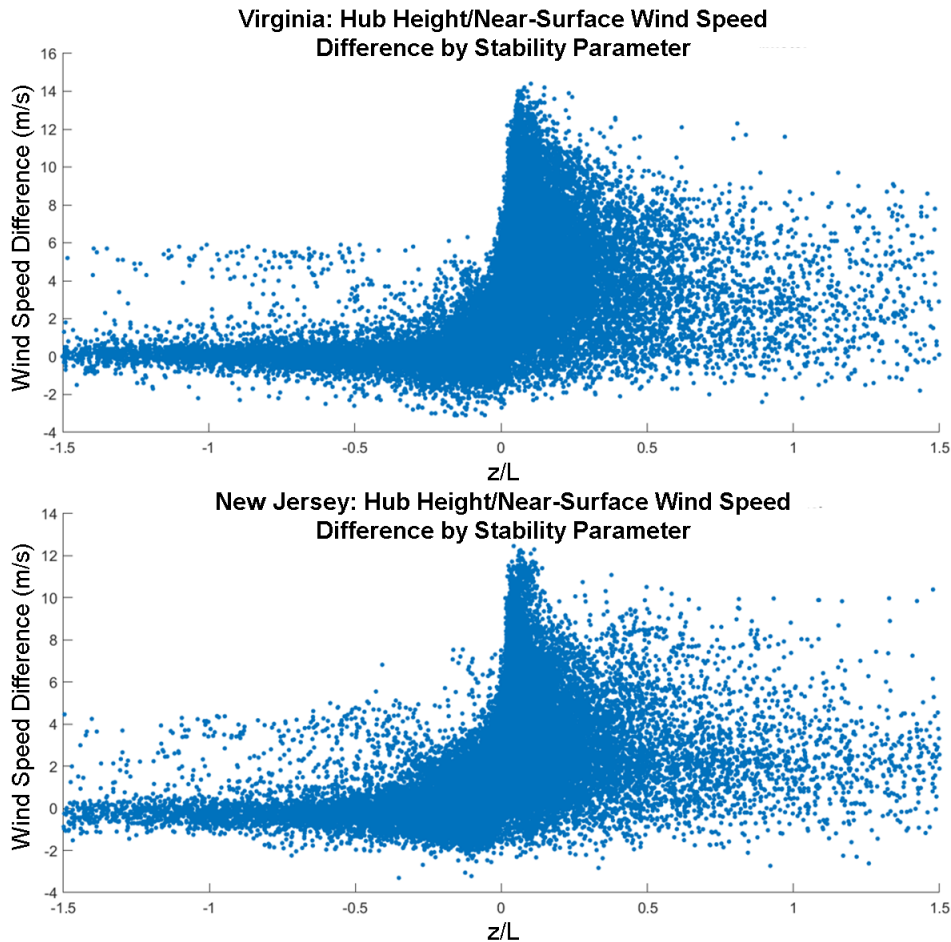


Figure 3.20. Difference between hub-height and near-surface wind speeds as a function of atmospheric stability.

3.3.2 Temperature

The mean near-surface air temperatures for each deployment are 13.7°C and 12.4°C for Virginia and New Jersey, respectively. The warmer temperature for Virginia fits in a latitudinal sense, although Figures 3.21 and 3.22 show the capability of the New Jersey site to reach the highest temperatures of the two during convective months and times of day, likely due to the closer proximity to shore.

The seasonal temperature plots in Figure 3.21 have similar trends between the two buoy sites. Both have the warmest temperatures and the least amount of variability occurring in the summer months, and the coldest temperatures and largest range happening in the winter months.

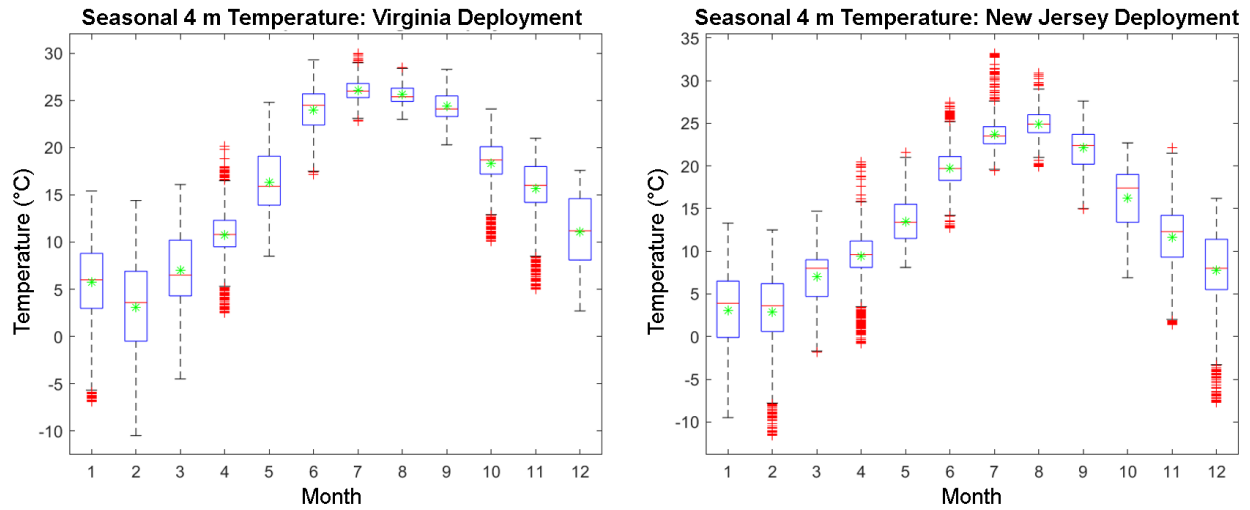


Figure 3.21. Seasonal distributions of near-surface air temperature for Virginia and New Jersey.

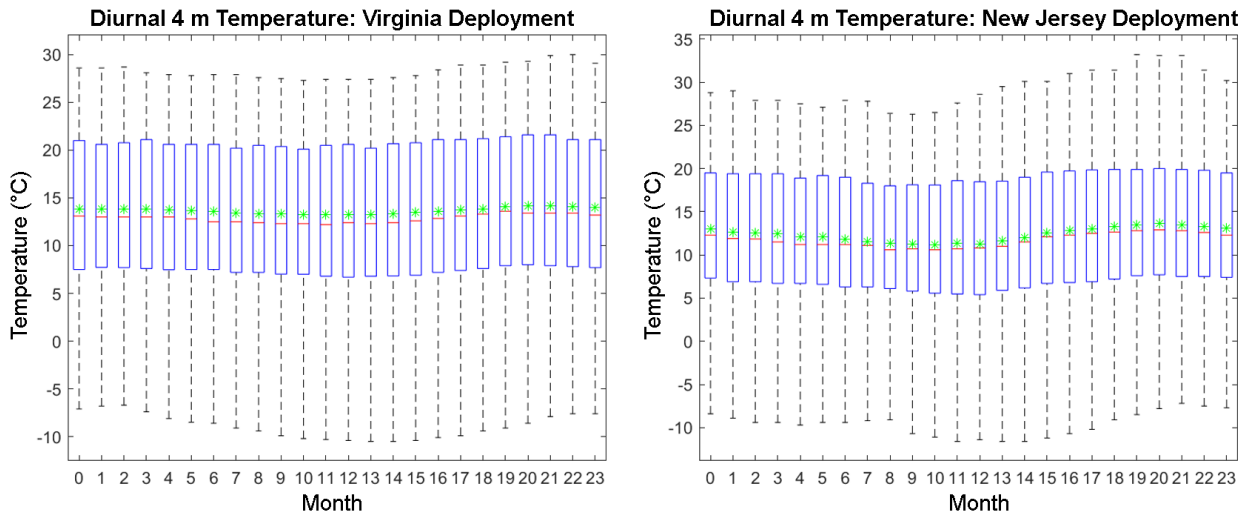


Figure 3.22. Diurnal distributions of near-surface air temperature for Virginia and New Jersey.

3.3.3 Relative Humidity

Figures 3.23 and 3.24 display the seasonal and diurnal trends in relative humidity for the buoys. The lower values of humidity seen in the afternoon correlate to the well-mixed unstable conditions that tend to occur at that time.

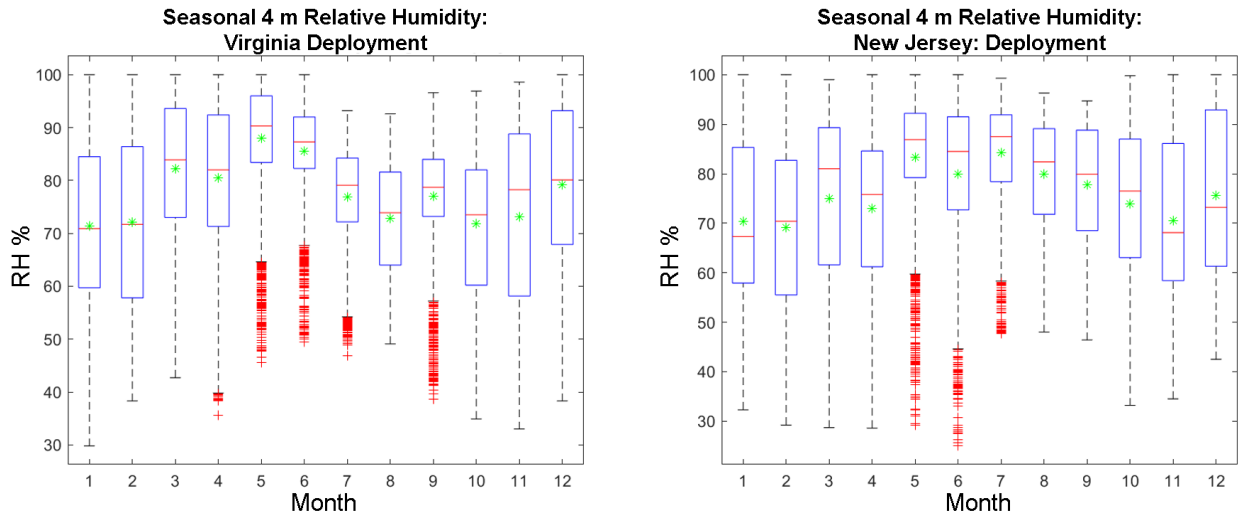


Figure 3.23. Seasonal distributions of 4 m relative humidity for Virginia and New Jersey.

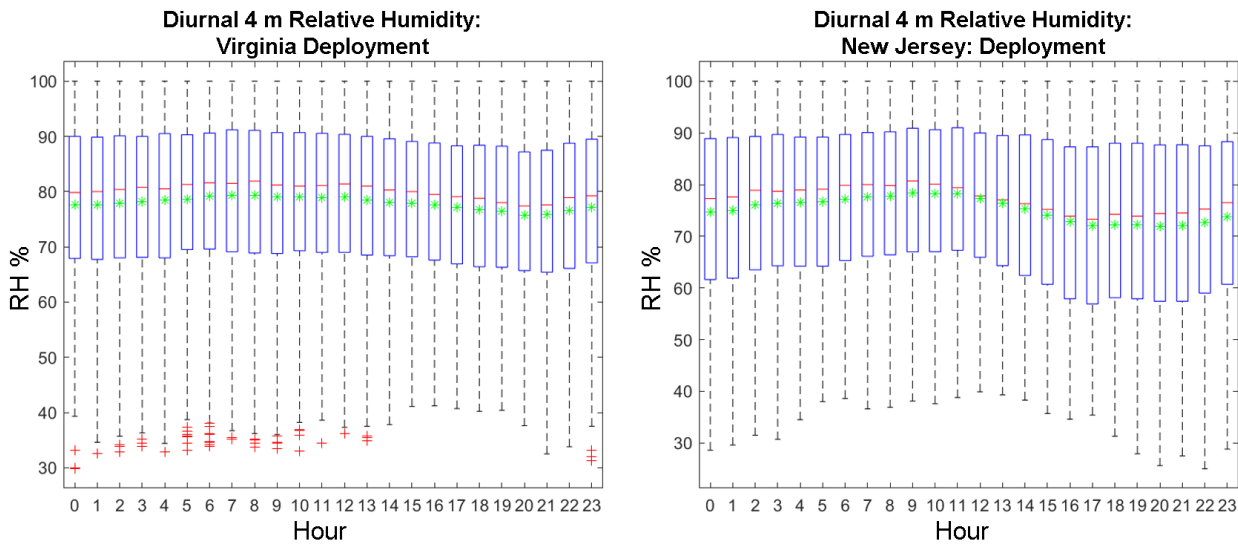


Figure 3.24. Diurnal distributions of 4 m relative humidity for Virginia and New Jersey.

3.3.4 Pressure

Summer months for both deployment sites have the lowest pressures and smallest spreads at 4 m, as shown in Figure 3.25. The low pressure outliers seen at both buoys in January are from the January 22–24, 2016, extreme blizzard in the Mid-Atlantic, which occurred during the overlap in deployment years. The lowest pressures occurred at the Virginia buoy on January 23 during this storm and on January 24 at the New Jersey buoy.

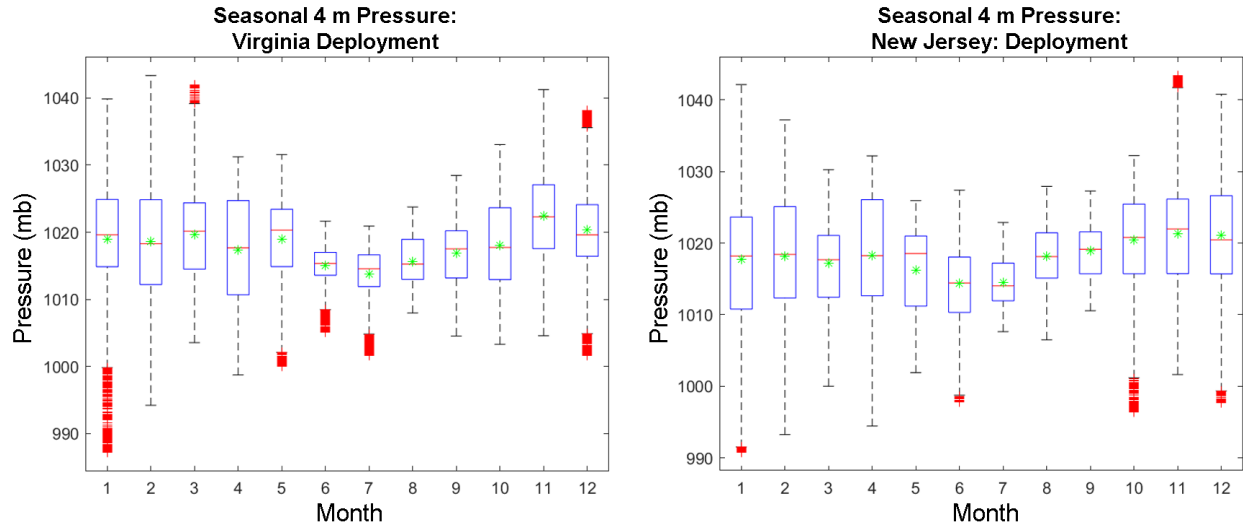


Figure 3.25. Seasonal distributions of air pressure for Virginia and New Jersey.

3.4 Summary

The WindSentinel buoys provide a rare opportunity to study the flow long-term at both hub height and near the surface at locations that can change based on opportunity and interest. The initial studies at Virginia and New Jersey resulted in valuable observations that are being used to characterize the wind resource near offshore lease locations and to validate current weather models. Upcoming work will use the Virginia and New Jersey meteorological observations to identify conditions under which models struggle to capture the wind fields with the goal of improving the capabilities of future models and versions.

The methodologies developed for the assessment of the Virginia and New Jersey deployments will be applied to the upcoming California deployments and beyond to achieve the goal of improving understanding of the evolutions of the wind fields at the surface and at heights of particular importance to the wind energy industry.

4.0 Basic Climatology of Sea State

The WindSentinel buoys are each equipped with TRIAXYS Next Wave II sensors to measure wave features such as significant wave height, wave period, and wave direction. The following discussion provides an analysis of these properties on a seasonal basis and for the entire annual cycle for both the Virginia and New Jersey deployments. The directions reported by the wave sensors were measured relative to magnetic north. For this study, it is noted that the directions have been corrected to true north by adding 11.3° to the Virginia directions and 12.4° to the New Jersey directions. Figure 4.1 shows the location of the lidar buoys and three other National Data Buoy Center buoys that have been deployed in the region for more than 20 years. The latter are used to put the measurement period in the historical context.

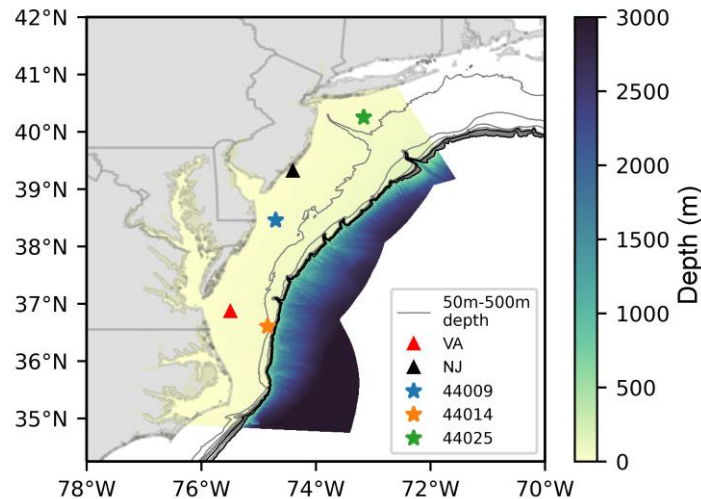


Figure 4.1. Bathymetry of the study region in pseudo color and with buoy locations identified.

4.1 Historical Context of Sea State

The wave climate in the Mid-Atlantic Bight is characterized by energetic winters and calmer summers (Bromirski and Cayan 2015). Waves in the 90th percentile are both larger and have longer periods in the winter than in the summer. However, most of the extreme events in the U.S. East Coast are associated with hurricanes occurring in late summer and early autumn (Komar and Allan 2008). There are three buoys with long records in the Mid-Atlantic Bight that serve to put the measurement period into the context of the wave climate. Buoys 44009, 44014, and 44025 have datasets starting in 1986, 1990, and 1991 to the present; their locations are shown in Figure 4.1.

Figure 4.2 shows the empirical cumulative probability density functions for significant wave height (H_{m0}) at these buoys. H_{m0} is defined from the frequency resolved variance spectrum ($E(f)$) after the water surface elevation time series is transformed into the frequency domain via Fourier transforms:

$$H_{m0} = 4\sqrt{m_0} \quad (4.1)$$

where m_0 is the zeroth-order spectral moment. The n th-order moment (m_n) is defined by:

$$m_n = \int_0^\infty f^n E(f) df \tag{4.2}$$

with f being the spectral frequency.

The yearly climatology (Figure 4.2a–c) during the sampling period aligns with the historical period, which for the longest record covers 32 years.

Seasonal characteristics during the deployment period follow the historical trends (Figure 4.2d–f). The sampled summers (JJA) show smaller waves than the long-term averages, particularly in the northern end of the study area (Figure 4.2f). Wave climate during the spring (MAM) and autumn (SON) are more similar to the winter (DJF) than the summer months.

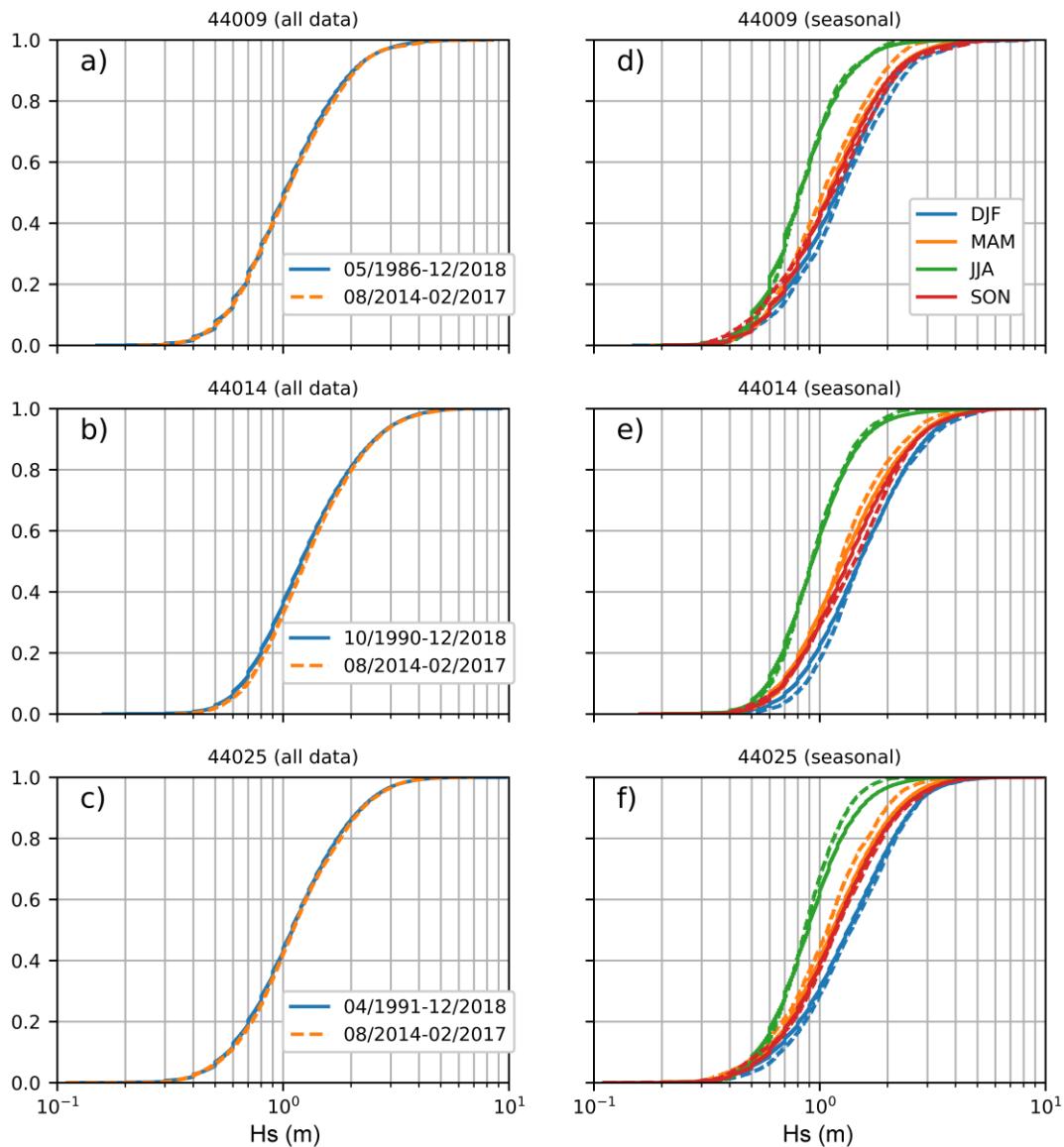


Figure 4.2. Empirical cumulative probability density functions of significant wave height at three long-term buoys in the Mid-Atlantic Bight. Dashed lines represent the period where lidar buoys were deployed.

4.2 Sea State Analysis Over Deployment Lifetime

4.2.1 Spatial Characteristics

Altimetry-derived wave heights provide global spatial coverage (Young and Donelan 2018). During the deployment period there were six altimeters that provided significant wave height estimates: JASON-2, JASON-3, SENTINEL-3A, HY-2, CRYOSAT-2, and SARAL. The combined dataset contains 82,007 measurements in the study period. Measurements based on Ku band (13–17 GHz) are used for all missions except for SARAL where the Ka band (30 GHz) is used. The reason for that is that SARAL does not provide wave data at the Ku band.

For visualization and analysis, data are binned in 0.2° by 0.2° cells, which at 40°N correspond to 22.2 by 17.0 km bins. Only bins with at least 20 data points are considered; the measurement density is shown in Figure 4.3f. Figure 4.3a–e show statistical representations of the measurements in the Mid-Atlantic Bight. During the lidar buoy deployment, H_{m0} averaged around 2.0 m offshore, which we define as water depths in excess of 200 m. During this same period five major hurricanes (Arthur, Hermine, Matthew, Jose, and Maria) and several other Nor'easters including the major blizzard of January 2016 affected the study site. Aggregated lidar buoy measurements show that waves inside the shelf exceeded H_{m0} of 8 m (Figure 4.3e). These data are also used for the validation of the numerical wave model developed for the Mid-Atlantic Bight discussed in Section 4.3.

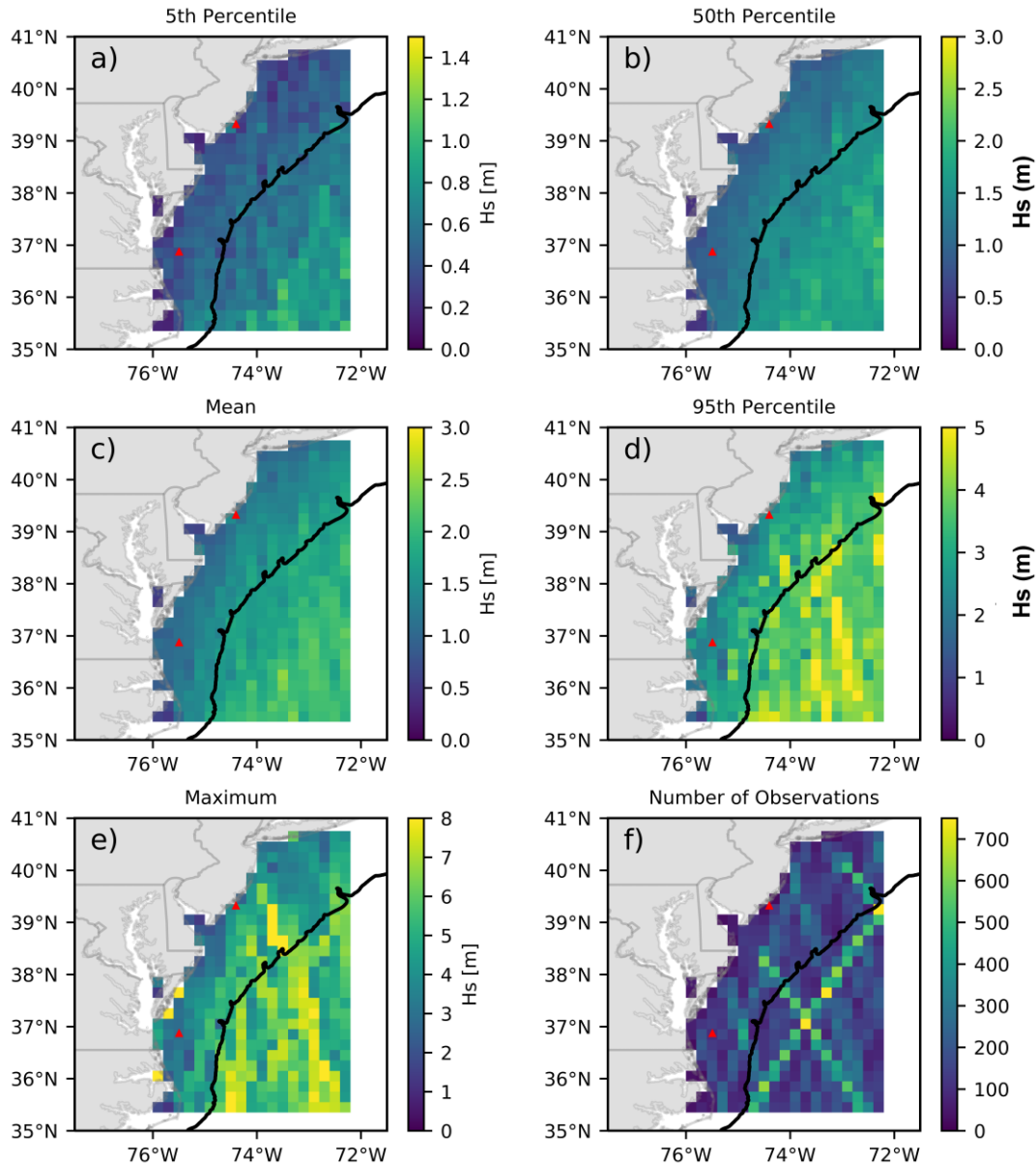


Figure 4.3. Altimetry-derived significant wave height climatology during lidar buoy deployment period. Red triangles mark the location of lidar buoys. Black line corresponds to the 200 m isobath. Note that color limits vary for all plots.

4.2.2 Lidar Buoys

4.2.2.1 Aggregated statistics during deployment time

Figure 4.4 shows the distributions of H_{m0} and wave direction for Virginia and New Jersey, respectively, for each deployment in its entirety. Waves encountering the Virginia buoy were bimodal in terms of directional distribution, coming mainly from the east-northeast and the east-southeast. The waves with the largest H_{m0} came from the east-northeast. The New Jersey buoy reported a bimodal distribution as well with the principal directions of propagation being from the east and from the southeast. At this location, the largest waves are well distributed in direction.

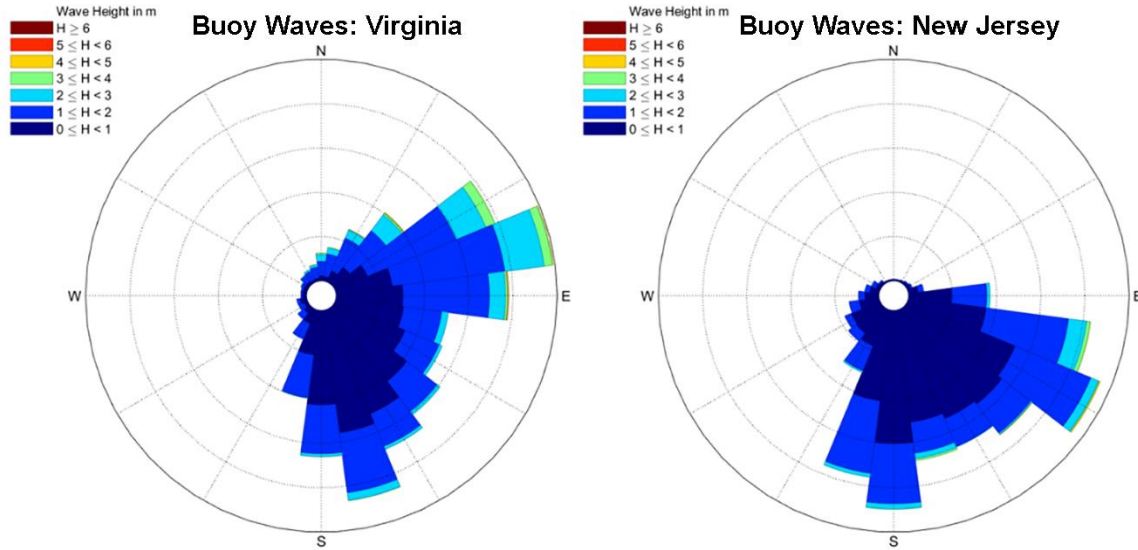


Figure 4.4. Distributions of significant wave height and wave direction for the Virginia and New Jersey deployments, respectively.

Two commonly used metrics to describe the wave period in real seas are the peak wave period (T_p) and the mean period (T_{m01}). T_p is defined as the inverse of the frequency corresponding to the peak of the wave spectrum, while T_{m01} is defined from the spectral moments (Equation 4.2) as m_0/m_1 . Bivariate distributions of H_{m0} and T_p , and H_{m0} and T_{m01} are shown in Figures 4.5 and 4.6, respectively. T_p s have a larger spread than T_{m01} s with events of 17s or longer periods occurring at both deployments. The most common sea state for both deployments has H_{m0} of 1.0 m. Occurrence of small T_p s is common at the New Jersey location, which indicates the presence of wind-driven seas dominate over swells.

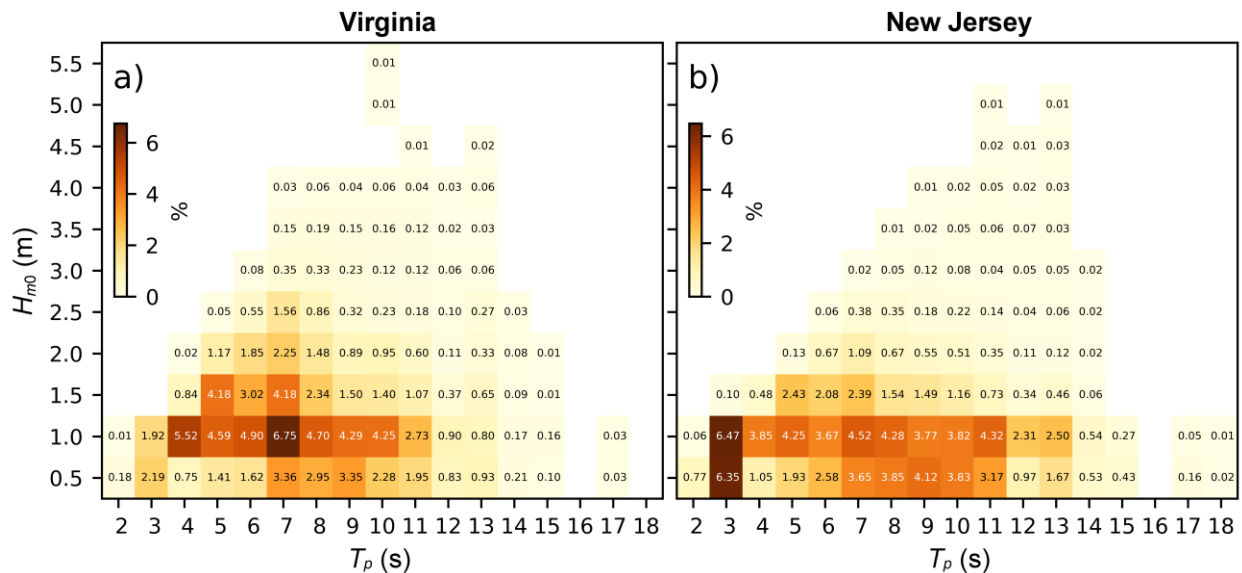


Figure 4.5. Bivariate distributions between significant wave height and peak period for the (a) Virginia and (b) New Jersey deployments. The percentages of occurrence above 0.01% are shown in each bin for a total sum of 100%.

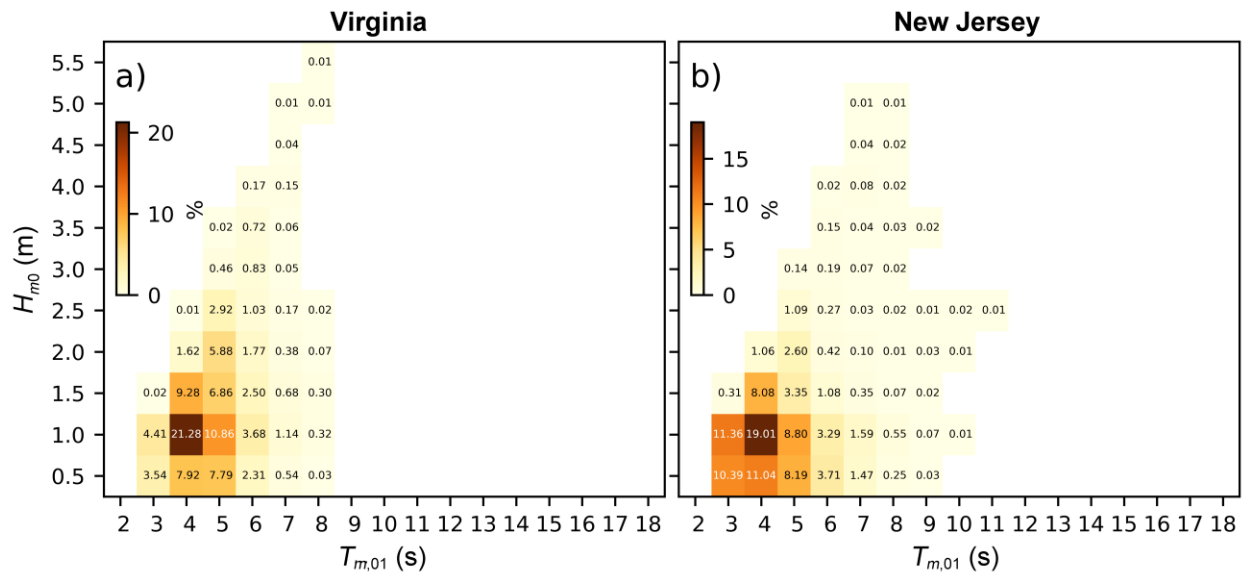


Figure 4.6. Like Figure 4.5 but for mean wave period.

The ratio of maximum wave height (H_{max}) to H_{m0} averages 1.6 for both deployments, where the maximum spread between the two has been as large as 3.2 and 3.9 for the Virginia and New Jersey deployments, respectively. In general, the distribution of maximum wave heights at both stations is wider than that of H_{m0} as shown in Figure 4.7.

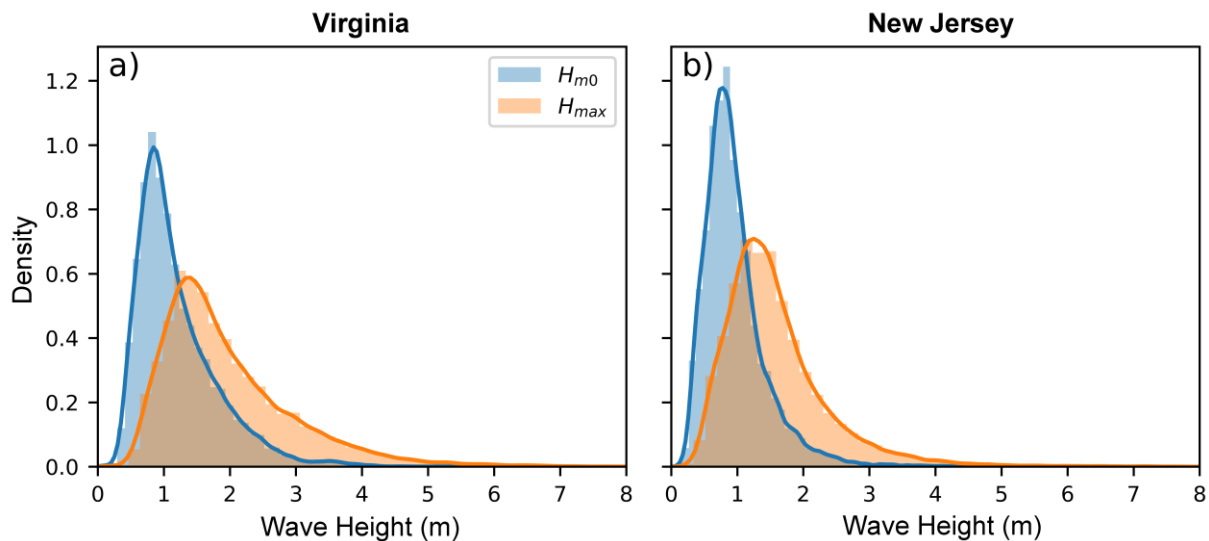


Figure 4.7. Significant wave height and maximum wave height histograms for the (a) Virginia and (b) New Jersey deployment.

4.2.2.2 Seasonal Characteristics

The seasonal wave climate captured at the Virginia site provides a sample that aligns with the general climatology of calmer conditions during the summer and stronger during the winter and shoulder months (Figure 4.8). January has the widest spread in the wave height distribution with the largest probability of outlier occurrence. The data collected by the lidar buoys sampled many large wave events as shown by the distributions. Empirical cumulative probability density

functions of significant wave height (Figure 4.9) show the same behavior as the long-term deployments (Figure 4.2).

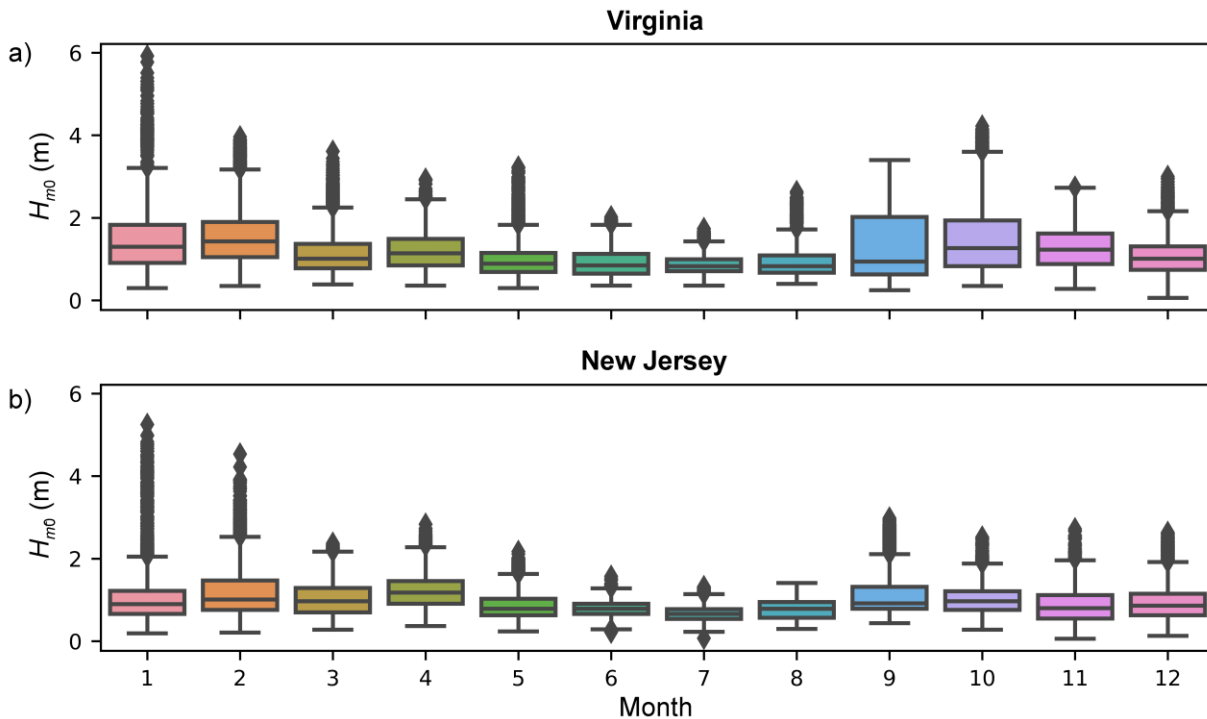


Figure 4.8. Monthly significant wave height spread.

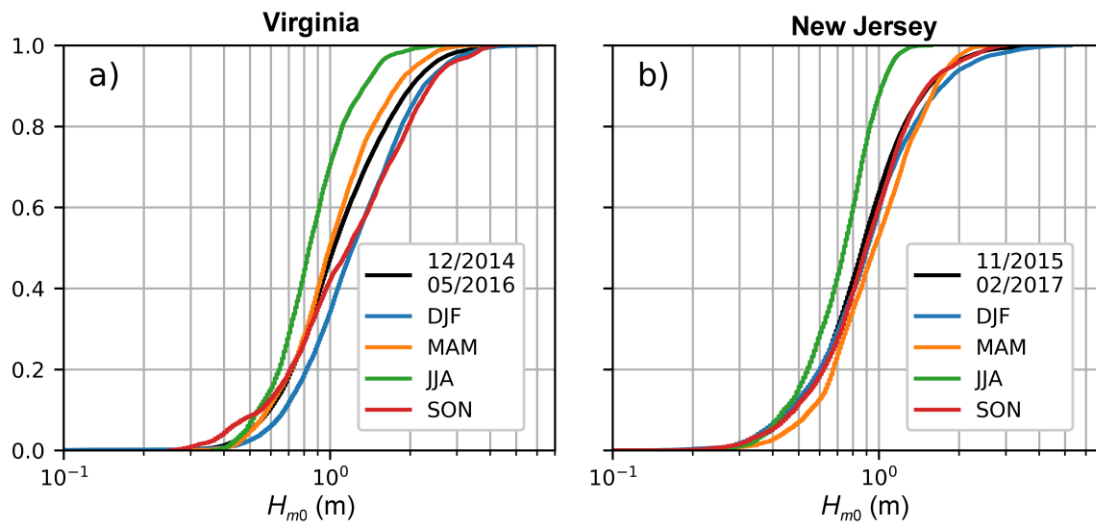


Figure 4.9. Empirical cumulative probability density functions of significant wave height for the (a) Virginia and (b) New Jersey deployments.

The dominant wave directions vary throughout the months. In Virginia, the waves approach from the southeast between May and August and predominantly from the northeast the rest of the year (Figure 4.10). December showed the most variability in the wave climate with a significant amount of energy approaching from the south to the northeast over a range of 160° . In contrast, most of the energy approaches from the south-southeast at the New Jersey location, consistent

year around (Figure 4.11). The lack of incoming wave energy from the north-northeast suggests blockage of swells by Long Island and the continent up to Massachusetts.

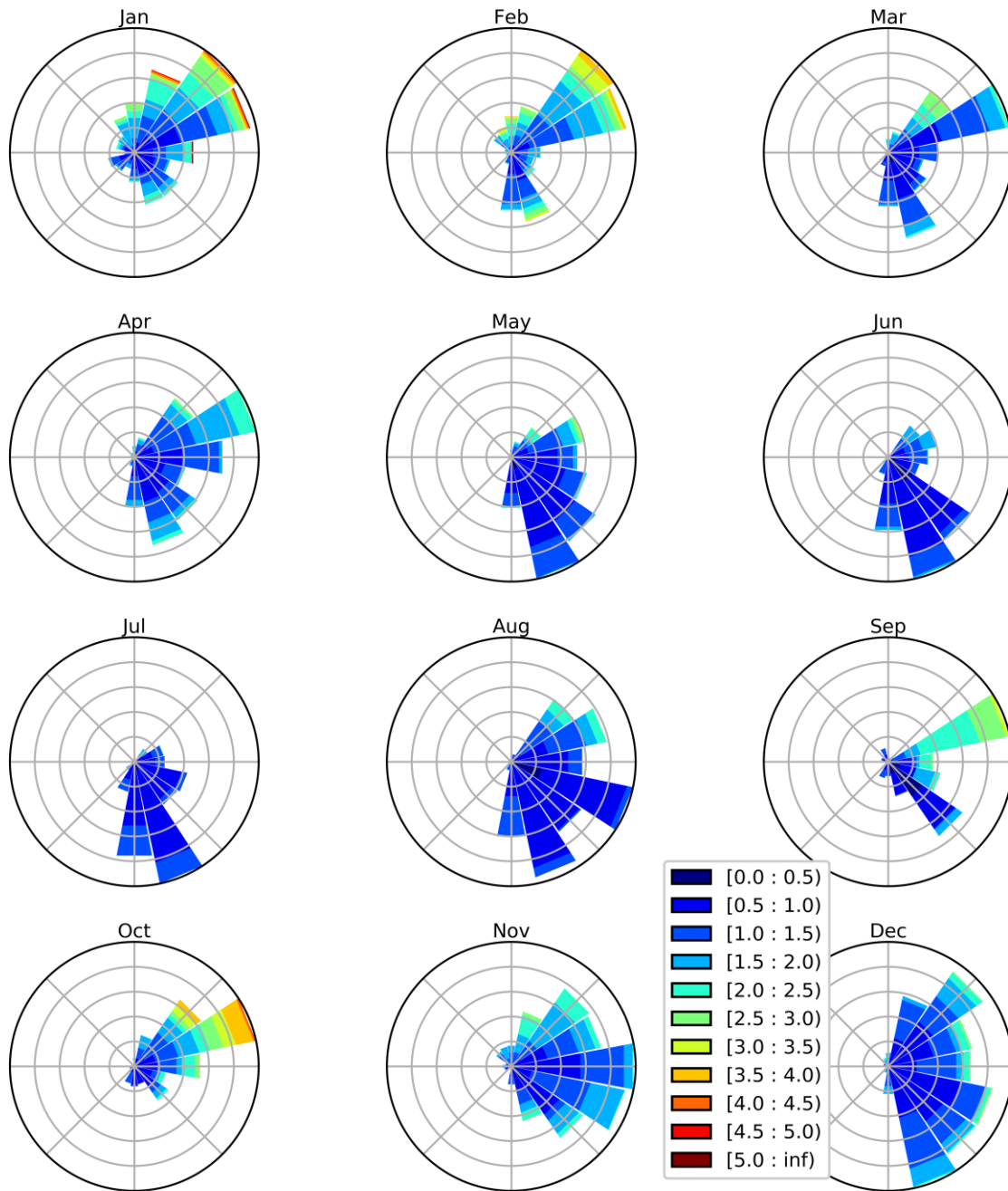


Figure 4.10. Monthly wave roses for the Virginia deployment. Significant wave height is shown in the colors.

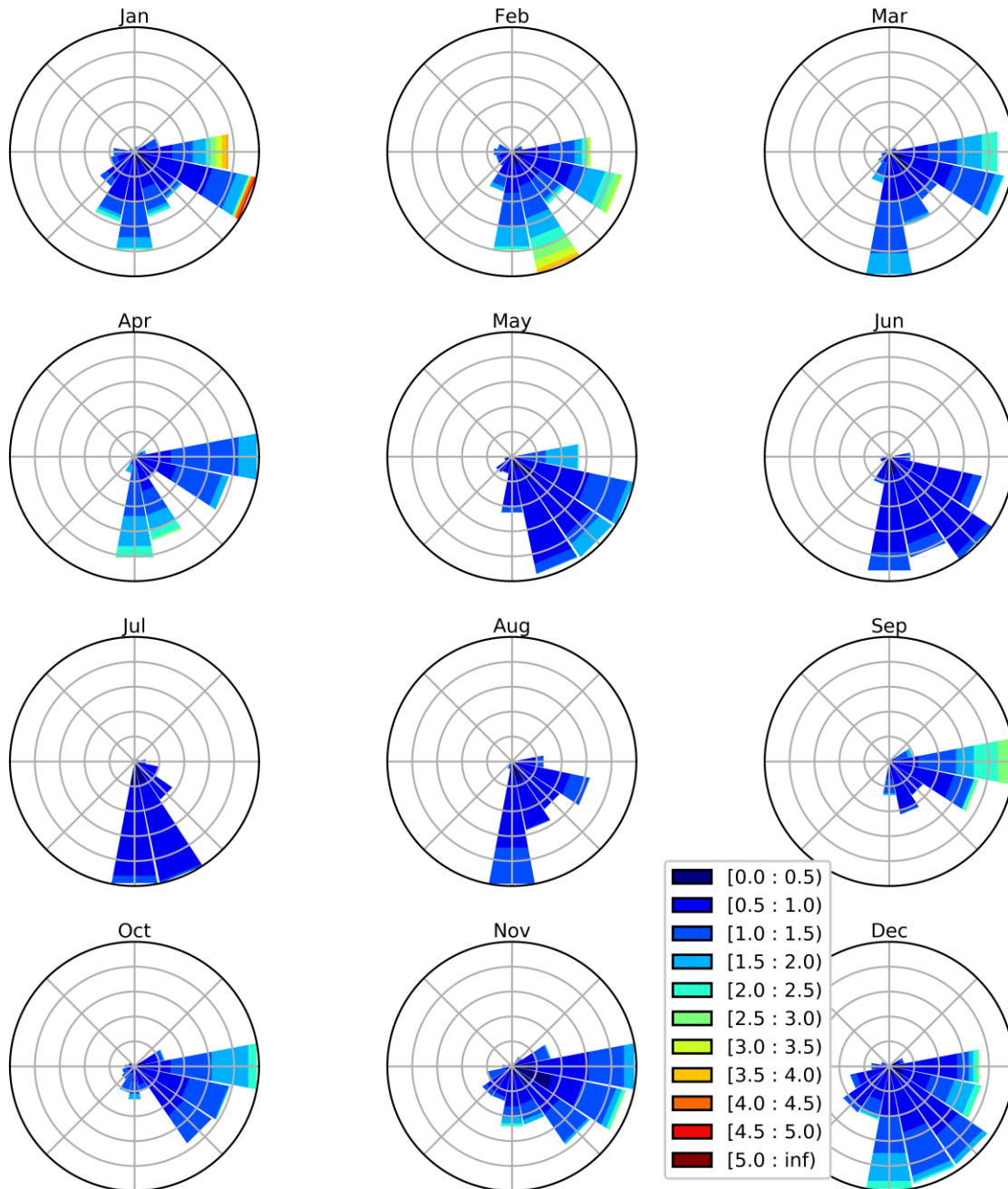


Figure 4.11. Monthly wave roses for the New Jersey deployment. Significant wave height is shown in the colors.

4.2.3 Tidal Influence

The dominant tidal constituent in the Mid-Atlantic Bight is the m^2 principal semi-diurnal component; this constituent represents the tidal generating force due to the rotation of the Earth with respect to the moon. In this section we investigate the tidal modulation on the waves measured by the lidar buoys. The tidal modulation in the wave heights can be assessed by transforming the time series of H_{m0} into the frequency domain. The longest continuous records for the Virginia and New Jersey deployments are 452 and 239 days, respectively. These time

series are converted to the frequency domain via Fourier transforms. To reduce the noise and artifacts, the mean is removed from the time series, then a Hanning window is applied before applying the Fourier transform. Finally, band averaging with a width of 10 frequencies is used to produce a spectrum with 20 degrees of freedom. Results are shown in Figure 4.12. A spike above the 95% confidence limit is observed in the Virginia deployment and not in the New Jersey deployment. The amplitude of the signal, found by integrating the three points around the peak, was found to be 3 cm for the Virginia deployment.

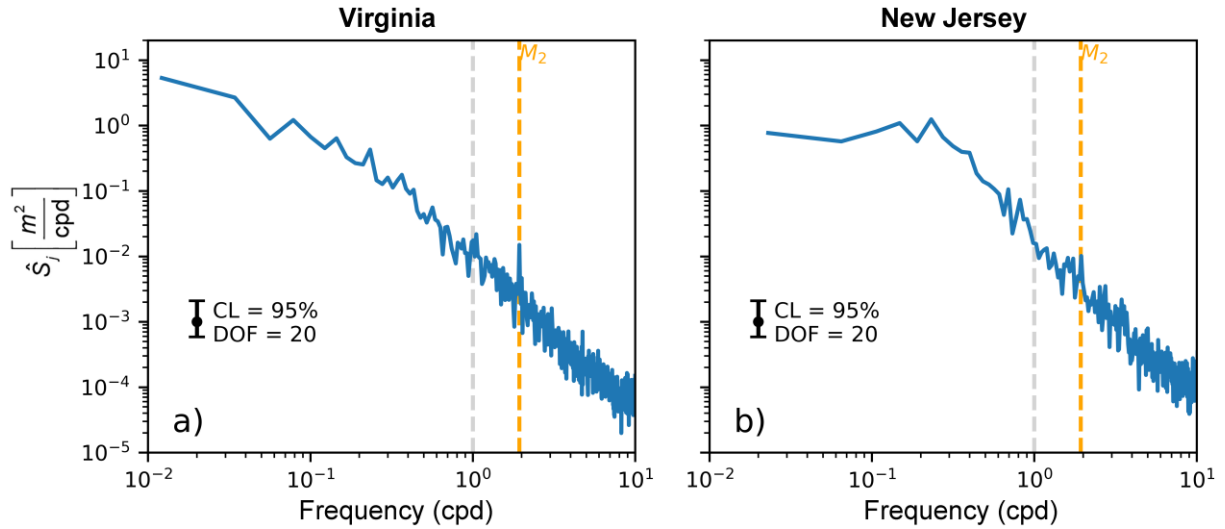


Figure 4.12. Power spectra of the significant wave height time series for the Virginia (a) and New Jersey (b) deployments.

4.3 Numerical Model Development

A numerical modeling study was conducted to complement the measurements by the lidar buoys and describe the spatial and temporal patterns of the wave field in the Mid-Atlantic Bight during the deployments. A model based on the third-generation wave-action-based model WaveWatch III (hereafter WW3) v5.16 was developed (WW3DG 2016). WW3 solves the spectral wave action balance equation:

$$\frac{\partial N}{\partial t} + \frac{\partial c_{gx} N}{\partial x} + \frac{\partial c_{gy} N}{\partial y} + \frac{\partial c_{\theta} N}{\partial \theta} + \frac{\partial c_{\sigma} N}{\partial \sigma} = \frac{1}{\sigma} (S_{in} + S_{ds} + S_{nl} + S_{bot} + S_{brk}) \quad (4.3)$$

where $N(t, x, y, \sigma, \theta) = \frac{E}{\sigma}$ is the wave action, $E \left[\frac{J}{m^2} \right]$ is the frequency and directionally resolved wave energy, t is time, x and y are the position, c is the velocity of propagation in each dimension, σ is the radian frequency, and θ is the direction. The right-hand side of the equation represents the sources and sinks of energy. Wave growth (S_{in}) and dissipation due to whitecapping (S_{ds}) are modeled with the ST4 source term package (Ardhuin et al. 2010). This parameterization also includes swell dissipation. Default model parameters are used for non-linear quadruplet interactions (S_{nl}), dissipation due to bottom friction (S_{bot}), and depth-induced wave breaking (S_{br}). The wave spectrum is discretized with 32 logarithmically spaced frequencies ranging from 0.035 to 0.672 Hz, and 36 equally spaced directions.

The model has been developed with a spatial resolution adequate for capturing the wave transformation processes in the shelf and near-shore regions. The system refines the existing NOAA modeling framework for dynamical downscaling to the coasts of Virginia, Maryland, Delaware, and New Jersey. In order to capture near-shore and shelf-scale physics, the refined model extends past the shelf break (200 m depth) to at least 200 km from the main shoreline. The resolution from all the models in the multi-level domain is shown in Table 4.1.

Table 4.1. Model resolution conversion table from spherical to planar coordinates and time steps used. 38°N is used as a reference latitude for the conversions.

Model Level	Agency	Spherical	Zonal, m	Meridional, m	Δt_g , s	Δt_{xy} , s	Δt_k , s	Δt_s , s
L1	NOAA-NCEP	30'	43,810	55,600	1800	600	900	30
L2	NOAA-NCEP	10'	14,600	18,530	900	450	450	15
L3	NOAA-NCEP	4'	5,842	7,413	600	150	300	15
L4	PNNL	1.2'	1,752	2,224	40	20	20	10

NCEP = National Centers for Environmental Prediction

WW3 solves the wave action equation explicitly requiring four time steps: global time step (Δt_g), spatial propagation time step (Δt_{xy}), intra-spectral propagation time step (Δt_k), and source term integration time step (Δt_s). The spatial propagation time step must conform with the Courant-Friedrichs-Lewy limit to ensure model stability. The selected model steps are shown in Table 4.1.

The offshore boundary condition is located at water depths of at least 2000 m, where surface gravity waves with periods of 25 s are not affected by the bathymetry. The transition from deep to shallow waters is being accounted for in the L4 model. The bathymetry for the L4 model was interpolated from the U.S. Coastal Relief Model (NGDS 1999a, b). These datasets have an approximate resolution of 100 m, much finer than the refined model (1 km) and are thus deemed adequate.

4.3.1 Wind Forcing

The model is forced by analyzed global winds at 10 m height from the Climate Forecast System Version 2 (Saha et al. 2014). The wind fields are collected at hourly intervals at two different spatial resolutions—12 arc-minutes and 30 arc-minutes. A convergence analysis to choose a model forcing resolution was performed by hindcasting January 2016 and forcing the wave model with both wind products. This month includes periods of small wave heights in the order of 1 m and a large wave event driven by a Category 5 blizzard (see Figure 4.13). Model performance was qualitatively assessed by comparing H_{m0} , T_p , and peak wave direction (D_p) at both deployments. Peak wave direction is defined as the direction that corresponds with the peak of the frequency integrated but directionally resolved variance spectrum. Model results are virtually indistinguishable; thus, for these types of conditions, there is model convergence. Because both wind fields are consistent, we will use the highest resolution model to force the WW3 ensemble given the potential of resolving hurricanes more accurately.

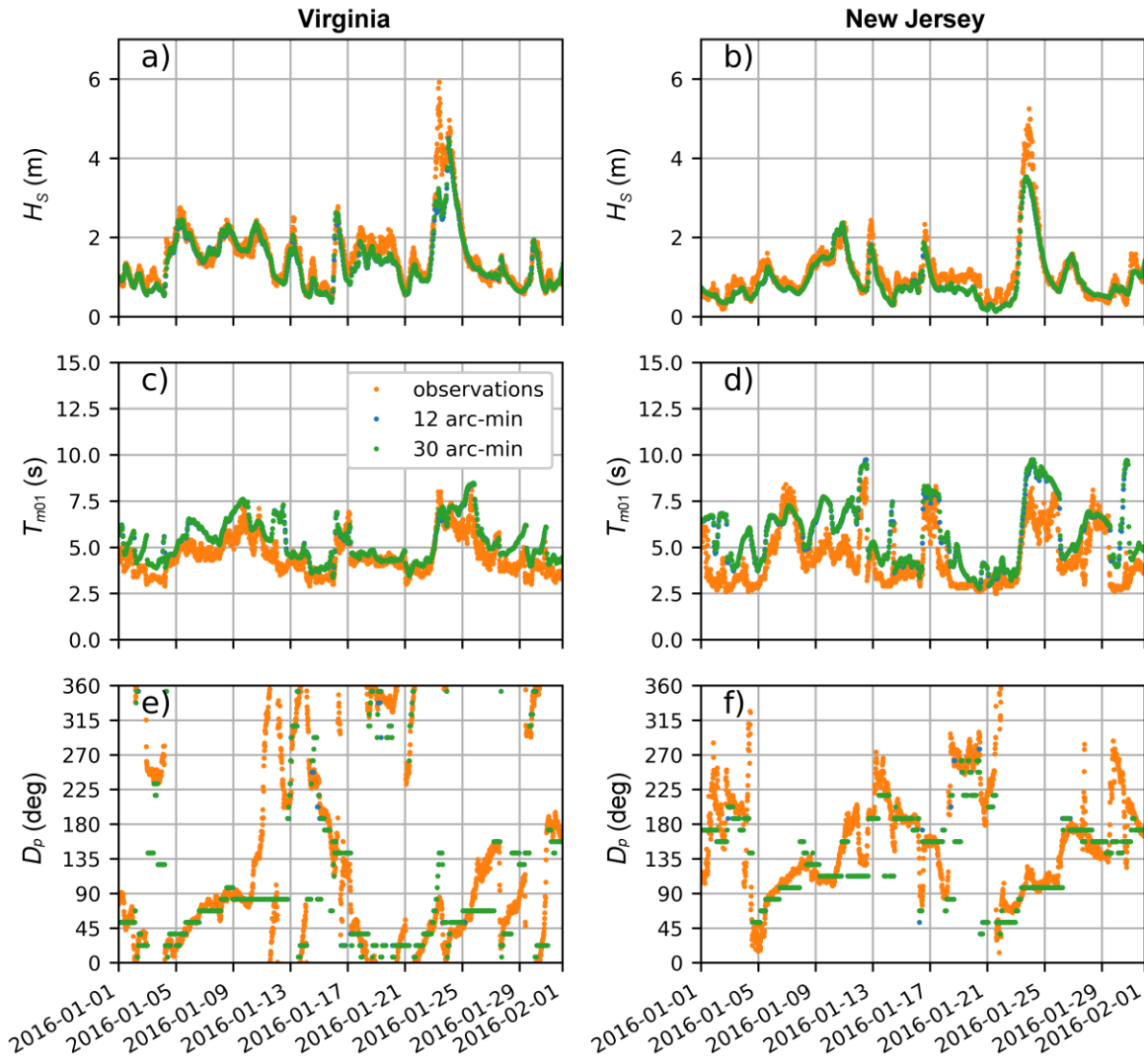


Figure 4.13. Model data comparisons for January 2016.

4.3.2 Surface Currents

Strong surface currents and eddies are ubiquitous in the Mid-Atlantic Bight. These currents can have a strong effect on the surface gravity waves (Ardhuin et al. 2017). We incorporate surface currents obtained from the HYCOM (Halliwell 2004) GOFS 3.0 analysis to force the model.^a The HYCOM GOFS 3.0 database covers the complete hindcast period with a consistent implementation, which is desirable for the temporal stability of the statistics. The surface currents are provided as daily snapshots at $1/12^\circ$ resolution. The Gulf Stream covers a significant portion of the L4 domain as shown in Figure 4.14. Maximum currents inside the model domain can exceed 4 m/s. Surface currents affect waves via refraction, advection of wave action, Doppler shifting, and wave growth—the latter because the wave growth source terms are a function of the relative speed between the wind and waves. For these reasons the currents are included in the model.

^a Data corresponding to experiments 91.0, 91.1, and 91.2 were downloaded from <https://www.hycom.org/dataserver/gofs-3pt0/analysis>.

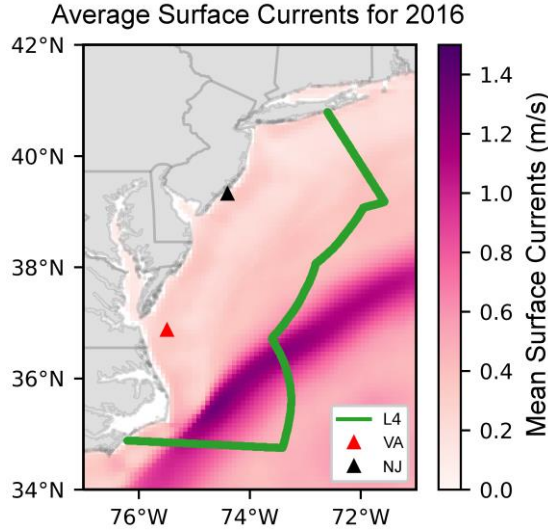


Figure 4.14. Average surface current intensity for 2016. VA and NJ stand for the buoy deployments off Virginia and New Jersey, respectively.

4.3.3 Ocean-Atmosphere Coupling

For simulation of wave growth and dissipation the source term package of Ardhuin et al. (2010) is implemented. This parameterization has been used extensively since its integration into WW3; it has been shown to outperform others (e.g., Ellenson and Ozkan-Haller 2018) and has been successfully implemented in global coastal hindcasts (Perez et al. 2017). The wind growth term is given by:

$$S_{in} = \frac{\rho_a}{\rho_w} \frac{\beta_{max}}{\kappa^2} e^{Z^2} Z^4 \left(\frac{u_*}{C}\right)^2 \times \max[\cos(\theta - \theta_u), 0]^p \sigma F(k, \theta), \tag{4.4}$$

where ρ_a and ρ_w are the density of the air and water, respectively; β_{max} is the non-dimensional growth parameter; κ is the von Kármán constant; Z is the effective wave age; u_* is the wind friction velocity; and F is the wavenumber-direction spectrum. Internally, WW3 keeps the wavenumber-direction spectrum, which can be converted to the frequency-direction spectrum in Equation 4.24.4, by using the linear wave dispersion relation, which is given by:

$$\sigma^2 = gk \tan h(kh). \tag{4.5}$$

where σ is the radian frequency, $k \left(= \frac{2\pi}{L}\right)$ is the wavenumber, L is the wavelength, g is the acceleration of gravity, and h is the water depth. The free parameter in Equation (4.4) is β_{max} , which represents the intensity of the ocean-atmospheric coupling. For model calibration this value has been set from 1.2 to 2 depending on the application (Rascle and Ardhuin 2013; Mentaschi et al. 2015; Perez et al. 2017). For the global and Atlantic Ocean models (L1 and L2) β_{max} is set at its default value of 1.33. Model calibration is performed at L3 and L4. Figure 4.15 shows the model results with β_{max} of 1.33 and 1.75. The improvement in the large wave prediction can be seen at the New Jersey deployment particularly when surface currents are included.

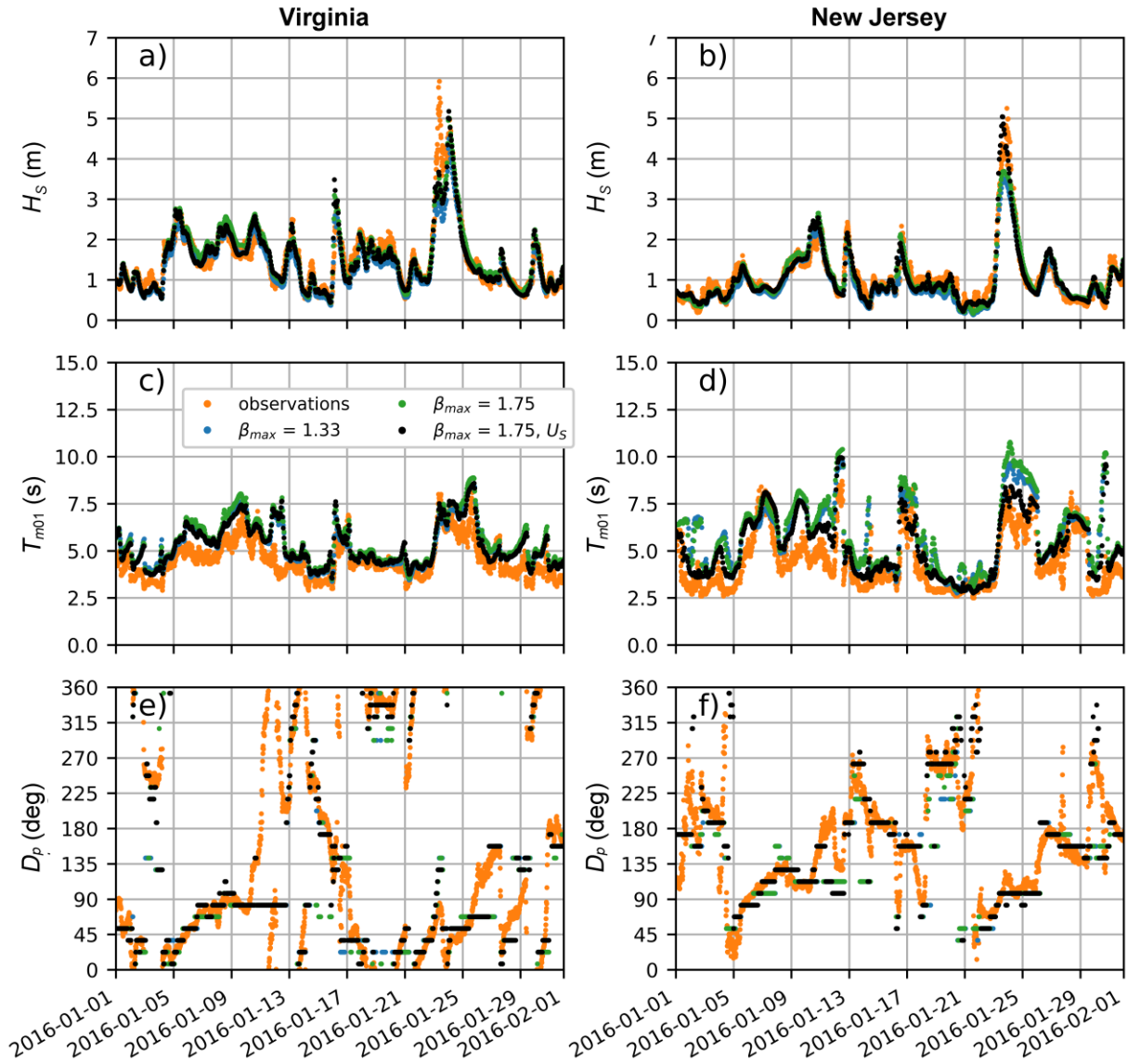


Figure 4.15. Model data comparisons for models with different atmospheric coupling intensities (β_{max}) and surface currents (U_s).

For a quantitative analysis, we compute *RMSE*

$$RMSE = \sqrt{\frac{\sum_{i=1}^N (P_i - M_i)^2}{N}}, \tag{44.6}$$

and percent bias (*pBias*)

$$pBias = \frac{100}{N} \sum_{i=1}^N \left(\frac{P_i - M_i}{M_i} \right). \tag{4.7}$$

N is the discrete number of observations, while P_i and M_i are the predicted and measured values, respectively. Error statistics are summarized in Table 4.2. The model shows statistical improvement when the ocean-atmospheric coupling intensity is increased and when the surface currents are included.

Table 4.2. Error statistics for sensitivity analysis.

Variable	Parameter		Virginia		New Jersey	
	β_{max}	U_s	RMSE	pBias, %	RMSE	pBias, %
Hs [m]	1.33	No	0.34	-10.1	0.28	-13.8
	1.75	No	0.29	2.5	0.23	-2.1
	1.75	Yes	0.28	-1.8	0.22	-2.6
Tm01 [s]	1.33	No	1.0	16.5	1.7	29.4
	1.75	No	1.2	20.0	1.9	33.8
	1.75	Yes	1.0	16.6	1.2	19.2

4.4 Summary

The wave climate during the lidar buoy deployment has been analyzed. The sampling provided during the deployment period aligns with the historical long-term climatology. Wave roses were calculated for the complete record and on a monthly basis to evaluate the trends. There is a seasonal rotation of the incoming waves at the Virginia site where most of the waves approach from the northeast in the winter and from the southeast in the summer. In contrast, the New Jersey site experiences a wave climate that is predominantly from the southeast.

A numerical model has been configured to complement the measurements at the lidar buoy sites. At the time of this writing, a four-year hindcast is underway. The numerical model has a spatial resolution of 1 km in the Mid-Atlantic Bight and is forced by analyzed winds and surface currents.

5.0 Basic Climatology of Ocean Currents

During both the Virginia and New Jersey deployments, ocean current data were collected using Nortek Aquadopp Acoustic Doppler Current Profilers (ADCPs), which were mounted to the stern of each buoy's hull. Ocean current data were collected at distinct sections within the water column (known as bins); separate measurements of the components of ocean currents were collected within each bin to generate a current profile. The depth of the first bin was approximately 3.65 m below the water surface with a bin cell size of 4 m. Given the water depth at the deployment locations and a bin size of 4 m, a total of 6 bins and 3 bins of data were collected at the Virginia and New Jersey deployment locations, respectively. Ocean current data for each buoy were truncated to only include times when the buoys were on station and operating by analyzing buoy position data.

5.1 Data Quality Analysis

Individual beam data were not archived during either the Virginia or the New Jersey deployment. Therefore, a data quality analysis relied primarily on a visual review of the magnitude of time series of averaged current profiles to identify data shifts (generally spikes) greater than 300 mm/s both spatially (compared to adjacent bins in the depth profile) and temporally (compared to adjacent averages). In this case, the data were averaged every 10 minutes. A total of 22 and 8 current profiles were removed from the Virginia and New Jersey ocean current data record, respectively.

The entire de-spiked current magnitude and direction data record is plotted for the Virginia and New Jersey buoys in Figures 5.1 and 5.2, respectively. Direction data are presented as magnetic directions *from* which the currents are flowing for these and all following figures, unless stated otherwise. A few items were noted in the visual data quality review of the current data:

1. Bin 1 of the Virginia ocean current magnitude data record appears to be low-biased.
2. The current direction in all bins of the Virginia ocean current data record appears to have shifted following the October 2015 high-current event (Hurricane Joaquin).
3. The current direction in all bins of the New Jersey ocean current data record appears to have shifted following a January 2016 high-current event (unnamed winter storm).

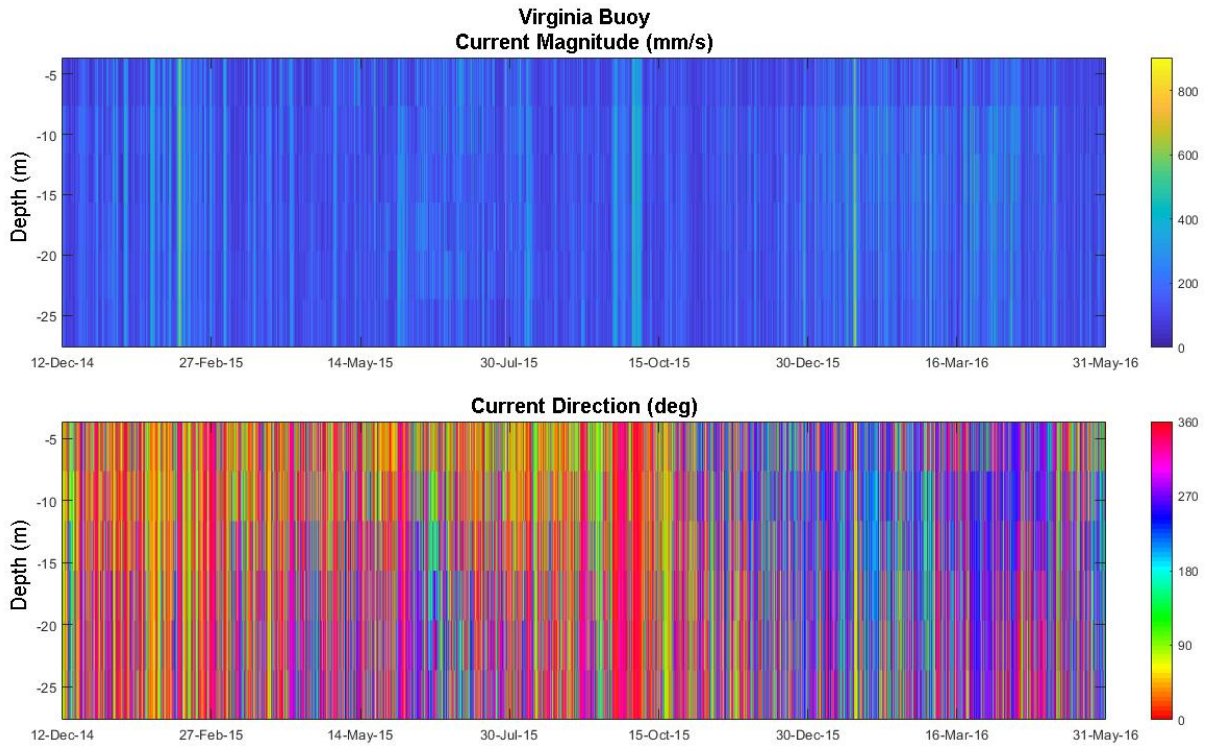


Figure 5.1. Current magnitude and direction color plots for the Virginia ocean current data record.

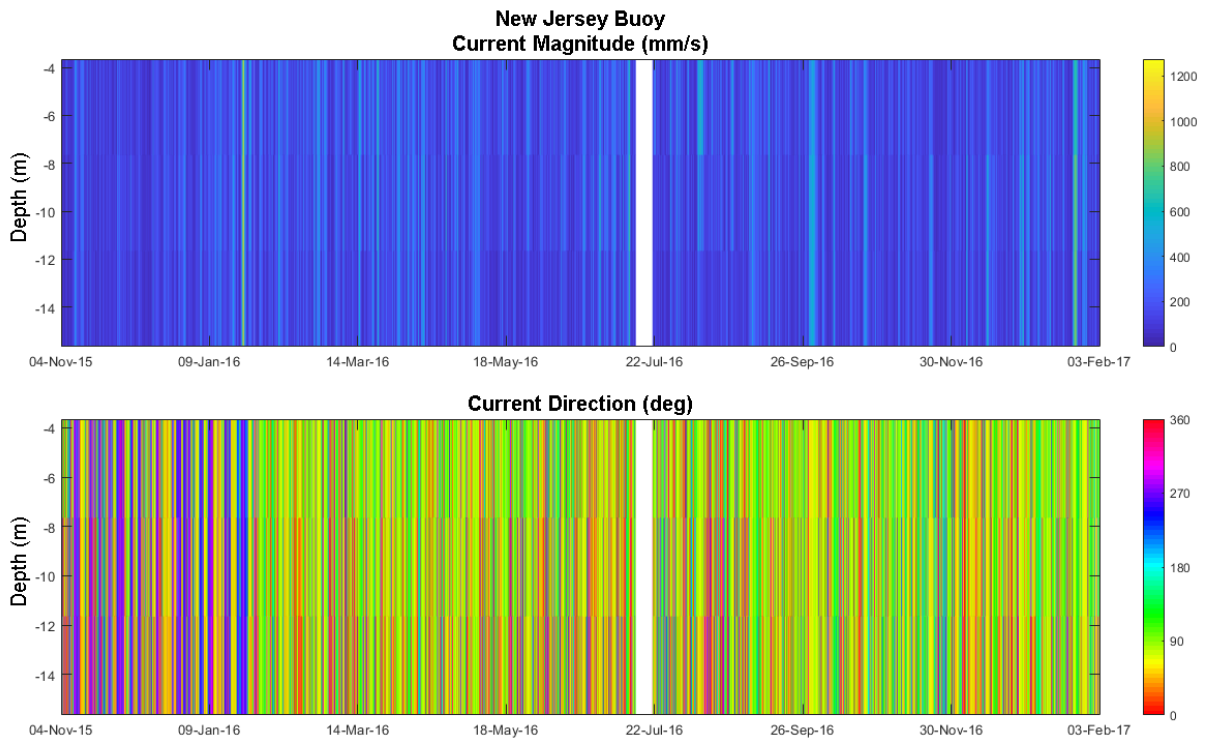


Figure 5.2. Current magnitude and direction color plots for the New Jersey ocean current data record.

Further analysis of the individual bin data was conducted in order to confirm and try to identify the cause of the items of note above. Figures 5.3 and 5.4, for the Virginia and New Jersey ocean current data records, respectively, show a current magnitude and direction comparison for each of the bins, averaged over five days for visual clarity. The low bias in Bin 1 of the Virginia ocean current data record is much more evident and appears to coincide with the shift following the October high-current event. Due to this low bias, any remaining analyses that consider the surface currents will use data from Bin 2. The New Jersey ocean current data record does not appear to be impacted by a low bias in Bin 1, aside from very minimal bias in the first few months of the deployment. Rather, all bins appear to have lower magnitudes in the first few months of the record. Note that the overlapping period of both records beginning in November 2015 shows very similar magnitude behavior in both deployment locations, suggesting that the low speeds in this period reflect ocean conditions.

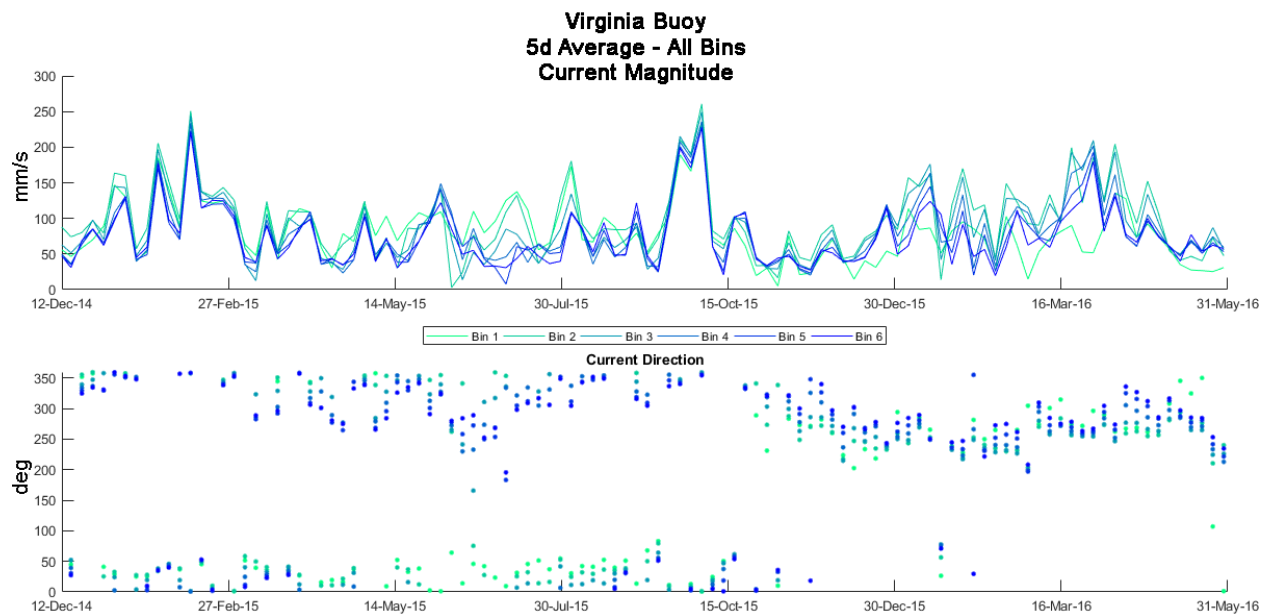


Figure 5.3. Current magnitude and direction by bin, averaged over 5 days, for the Virginia ocean current data record.

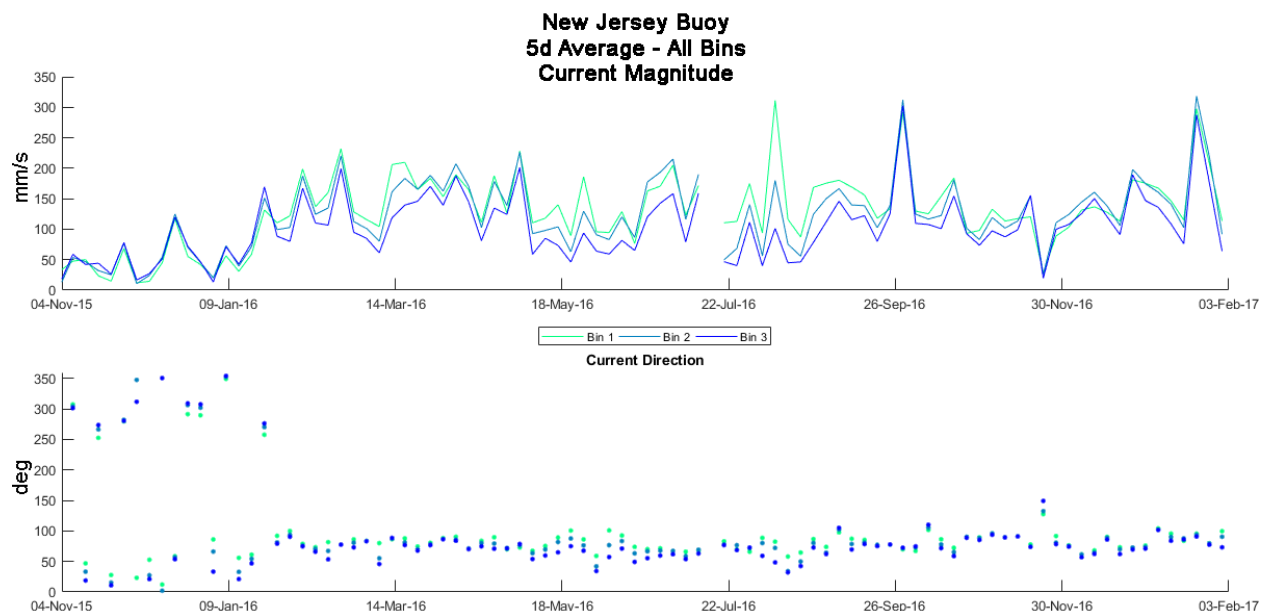


Figure 5.4. Current magnitude and direction by bin, averaged over 5 days, for the New Jersey ocean current data record.

Directions associated with the Virginia ocean current data indicate that the current direction as depth increases rotates in a counterclockwise direction prior to the direction shift and in a clockwise direction after the direction shift. Physically, this shift in rotation is unlikely and is an indication that the direction shift may be an artifact of the instrument rather than a physical oceanographic phenomenon.

In the New Jersey ocean current data record, the current directions have a bimodal element (likely tidal due to the proximity of this buoy to shore) that disappears after the January high-current event (which was smoothed out in 5-day averaging).

The exact dates of the shifts can be estimated both visually and numerically. Visually, the direction shifts appear to occur gradually between October 21, 2015, and November 4, 2015, for the Virginia deployment and on January 28, 2016, for the New Jersey deployment. A quantitative analysis identified the direction shifts to occur on November 3, 2015, and January 28, 2016, for the Virginia and New Jersey deployments, respectively. The analysis involved partitioning the data records for the Virginia and New Jersey deployments into two segments and iteratively adjusting the temporal location of the segment partition until the sum of the residual error of the local mean is minimized for both segments of the record.

For the Virginia ocean current data record, the gradual shift and the surface bin low bias suggests that the cause may have been a slow deterioration in instrument functionality or gradual increase in external interference. The only natural cause for the direction shift that seems plausible is an eddy separating from the nearby gulf stream and stagnating in the vicinity of the buoy. However, this is unlikely, as the eddy would have had to remain intact and in the same location for more than half a year, in relatively shallow waters.

For the New Jersey ocean current data record, the shift occurred suddenly after a 2-hour period of very low data quality (6 of the 8 removed ensembles during the quality review occur during this time period). The buoy was serviced on January 28, 2016, during which time the instrument

was removed from the water and cleaned. The direction shift can be directly correlated to the service visit, but it is unclear what the specific cause was. Not properly shutting off the instrument while out of water for cleaning may have been a factor, as operating ADCPs out of water for extended periods of time may cause instrument malfunctions. Exposure to a ferrous metal or other source of strong magnetic field may have also disrupted the compass calibration.

5.2 Comparison of Ocean Current Data to Other Buoy Sensor Data

The direction shift during both buoy deployments is further evident in the monthly surface current roses. Sample current roses are presented for each of the buoys in the two roses on the left-hand side of Figures 5.5 (Virginia) and 5.6 (New Jersey), comparing a month that occurs twice in its entirety during the respective deployment. The current direction associated with the Virginia ocean current data record appears to shift approximately 90–120 degrees and is evident during each of the repeated months. Prior to the direction shift, the currents generally originate from the north and flow southward. After the direction shift, the currents generally flow from east to west, which would imply the currents are coming from the shore. The directions associated with the New Jersey ocean current data record do not shift in the mean but rather shift from bimodal (flow from east-northeast and from west-northwest) to unimodal (flow from east-northeast). Due to the near-shore shallow depth of the New Jersey deployment, it is assumed the currents would be relatively bimodal due to tidal influence, but in actual ocean environments, this may not always be the case.

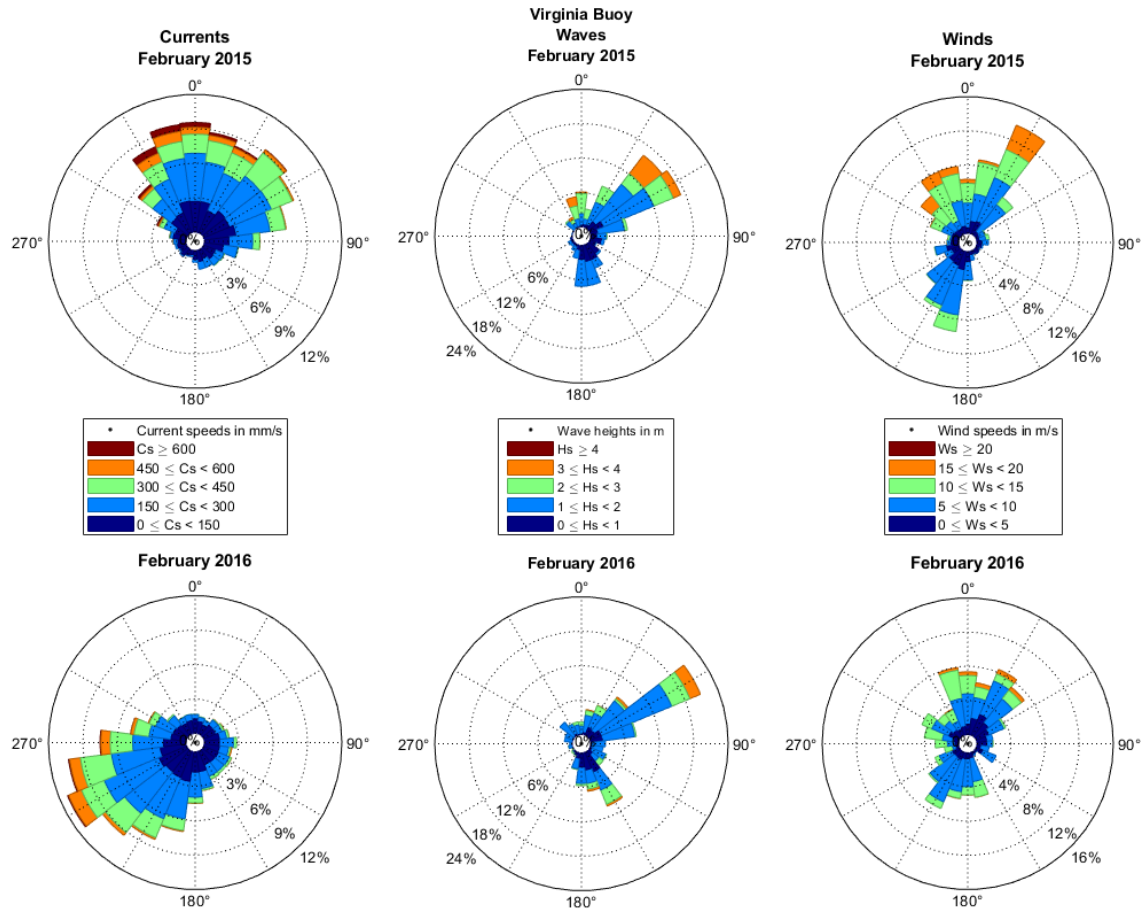


Figure 5.5. Current roses (*left*), wave roses (*center*), and wind roses (*right*) for February 2015 and February 2016 of the Virginia buoy deployment.

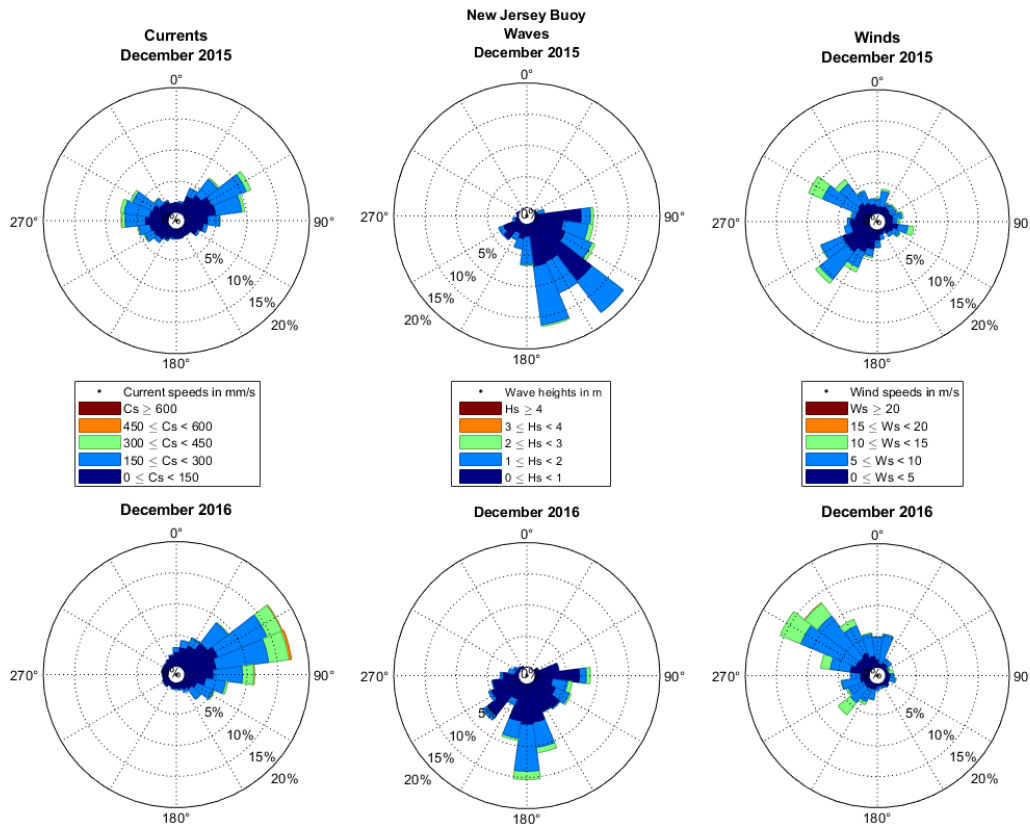


Figure 5.6. Current roses (left), wave roses (center), and wind roses (right) for December 2015 and December 2016 of the New Jersey buoy deployment.

Significant wave height and port anemometer wind roses for the same months are presented in the center and right roses of Figures 5.5 (Virginia) and 5.6 (New Jersey). Wave roses display significant wave height and mean wave direction measurements. The wind roses (and remaining analyses) use wind speed measurements from the port anemometer, as the starboard anemometer experienced signal problems during the New Jersey deployment and wind direction from the wind vane. Focusing on the directions of the winds and waves, the shift in direction seen in the current measurements is not evident, even during period of high winds when currents would most likely be influenced, further supporting the theory that the shifts are not likely a natural oceanographic phenomenon.

Figures 5.7 and 5.8 present time series comparisons of wind speed, significant wave height, and surface current magnitude for the Virginia and New Jersey deployments, respectively. For both deployments, increases in wind speed, significant wave height, and current magnitude are generally seen to occur at similar times throughout the record. Figures 5.9 and 5.10 present the time series comparisons of wind, wave, and surface current directions for the Virginia and New Jersey deployments, respectively.

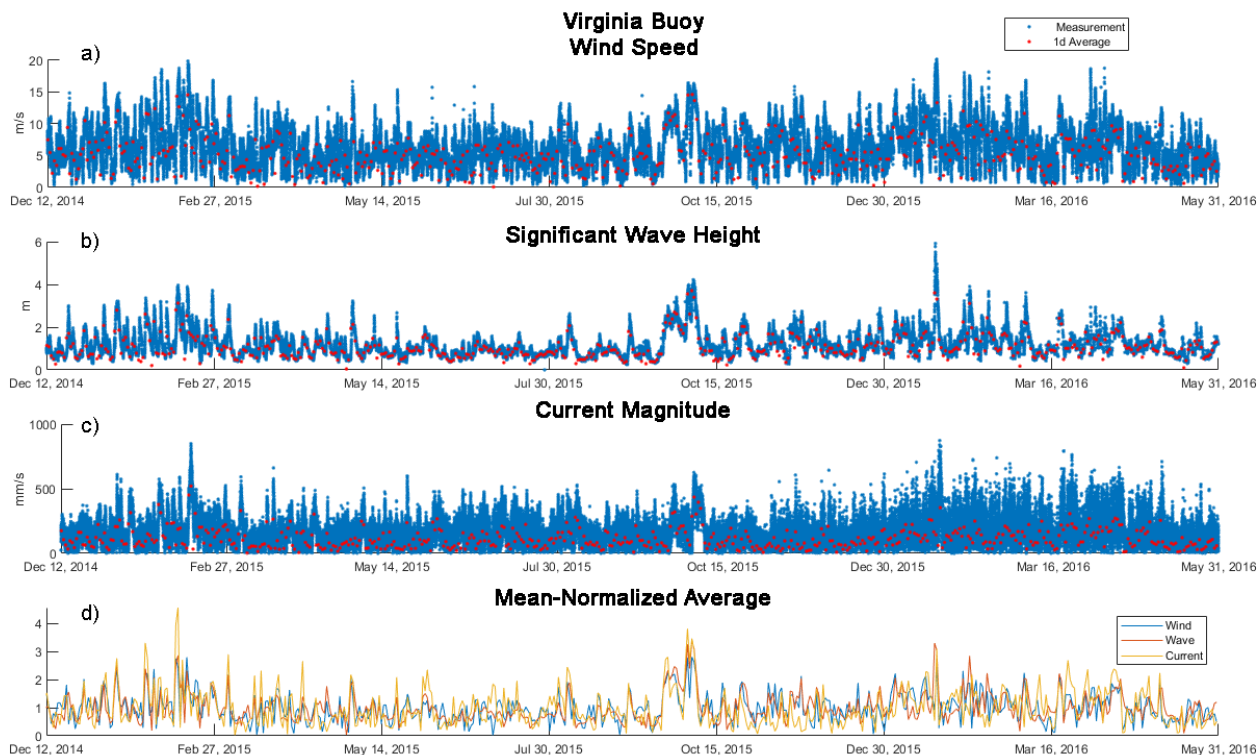


Figure 5.7. Wind speed (a), significant wave height (b), current magnitude (c), and a comparison of the mean-normalized averages (d) for the Virginia deployment.

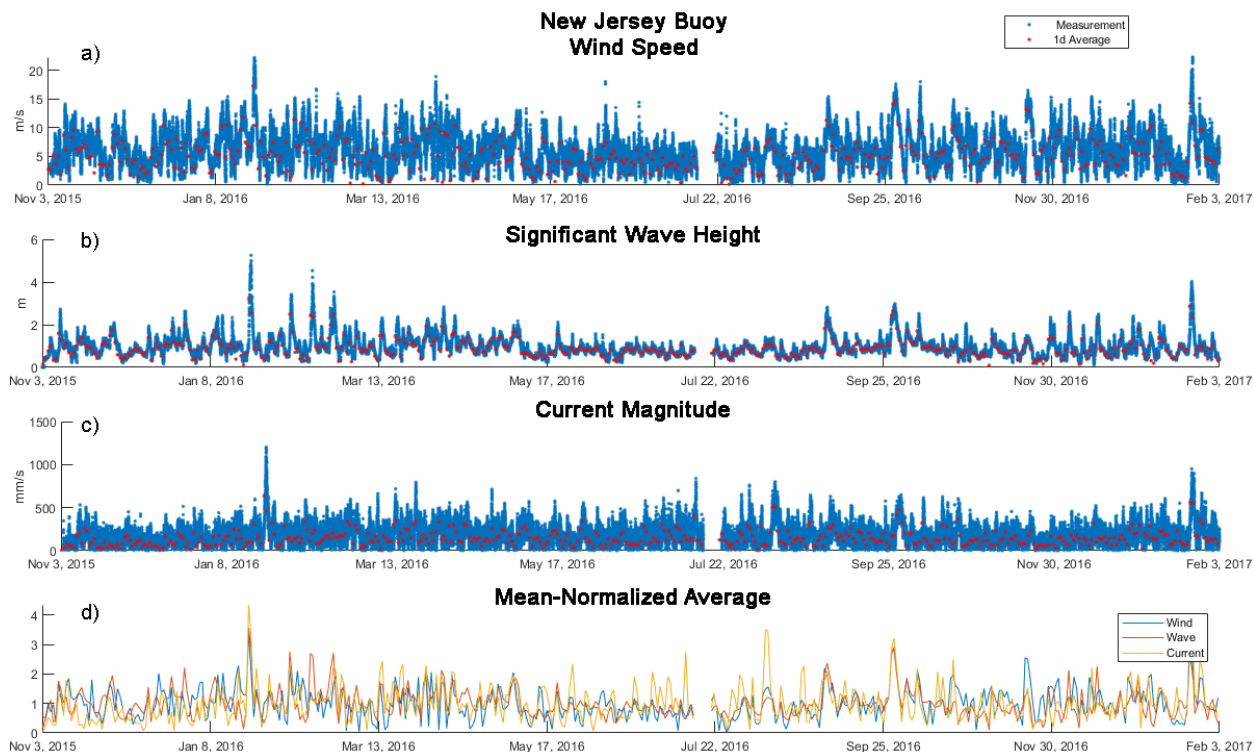


Figure 5.8. Wind speed (a), significant wave height (b), current magnitude (c), and a comparison of the mean-normalized averages (d) for the New Jersey deployment.

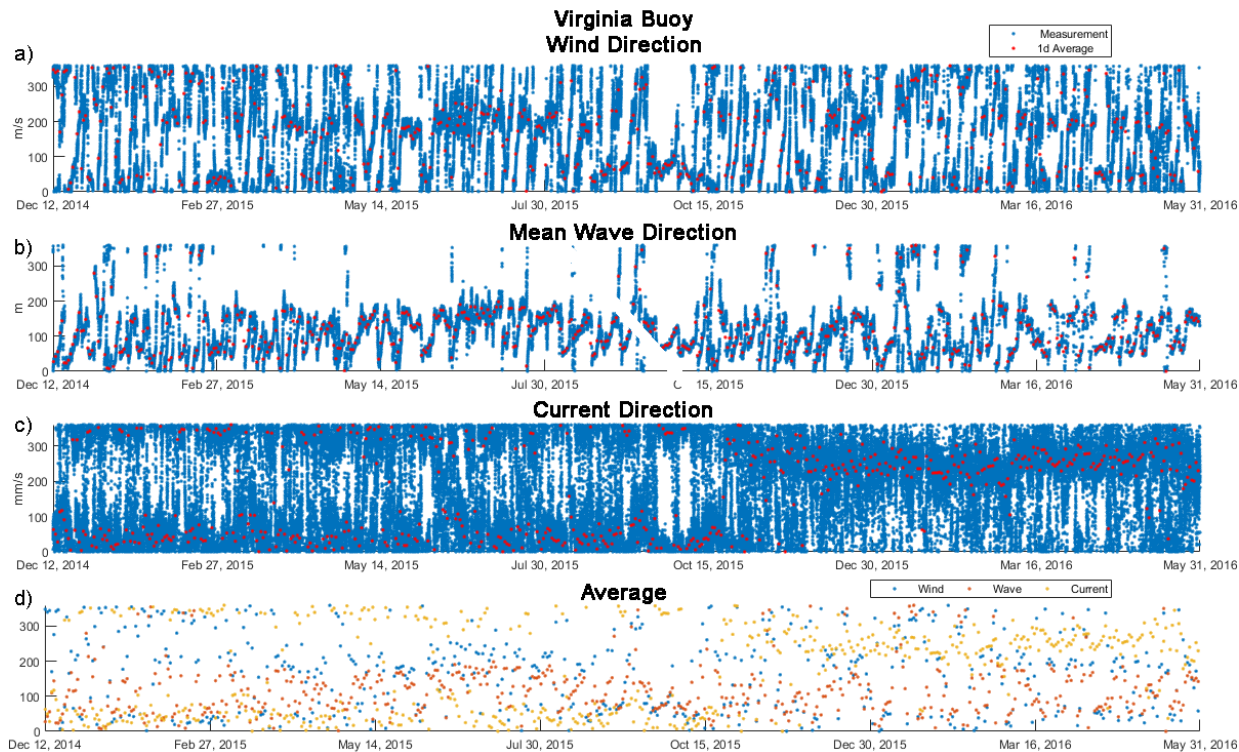


Figure 5.9. Wind direction (a), wave direction (b), current direction (c), and a comparison of the averages (d) for the Virginia deployment.

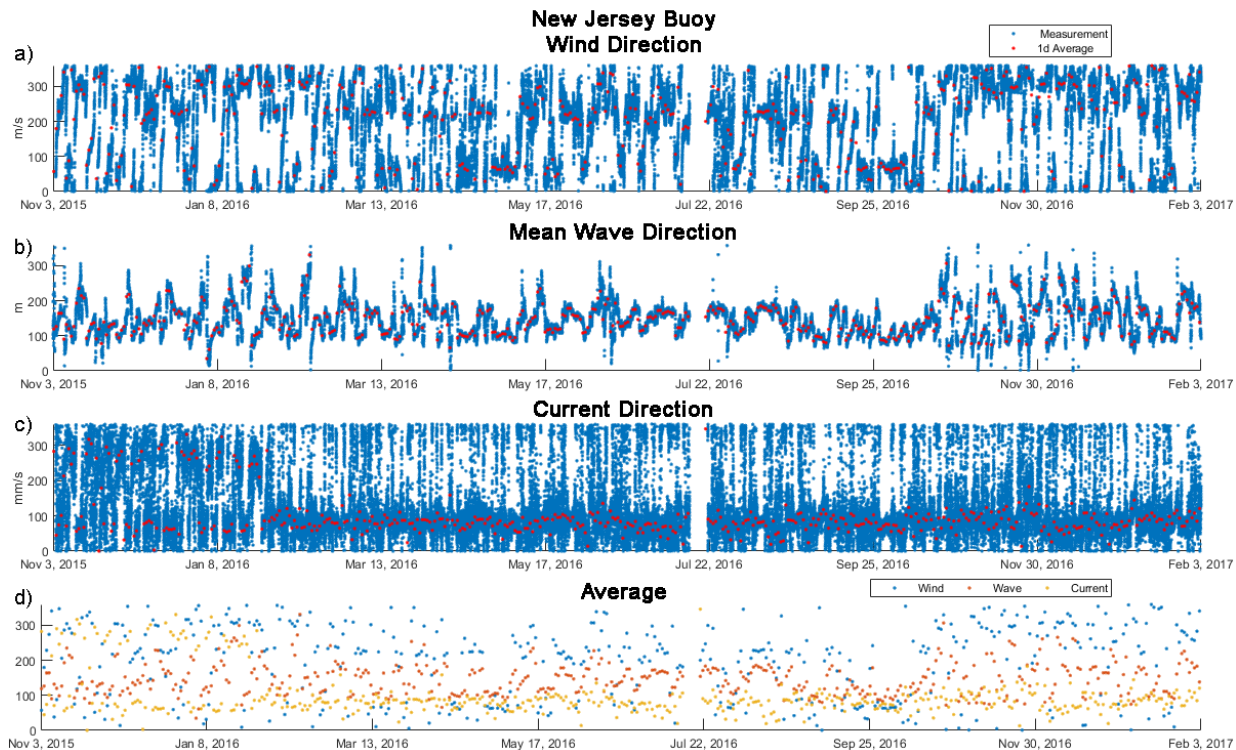


Figure 5.10. Wind direction (a), wave direction (b), current direction (d), and a comparison of the averages (d) for the New Jersey deployment.

Figures 5.11 (Virginia) and 5.12 (New Jersey) show vector plot comparisons between the 12-hour average of currents, waves, and winds for better visualization of the relationships between wind speed, significant wave height, and current magnitude and their respective directions. For the Virginia deployment, wind and wave directions generally shift in tandem, at an angle of approximately 30–60 degrees apart. The current directions, however, do not follow any distinct and consistent relationship pattern with the winds and waves, but during periods of increased magnitudes are generally in the same direction quadrant prior to the direction shift and are generally in the quadrant opposite the wind and waves after the shift. For the New Jersey deployment, a relationship between current, wave, and wind direction is much less distinct and difficult to parse out.

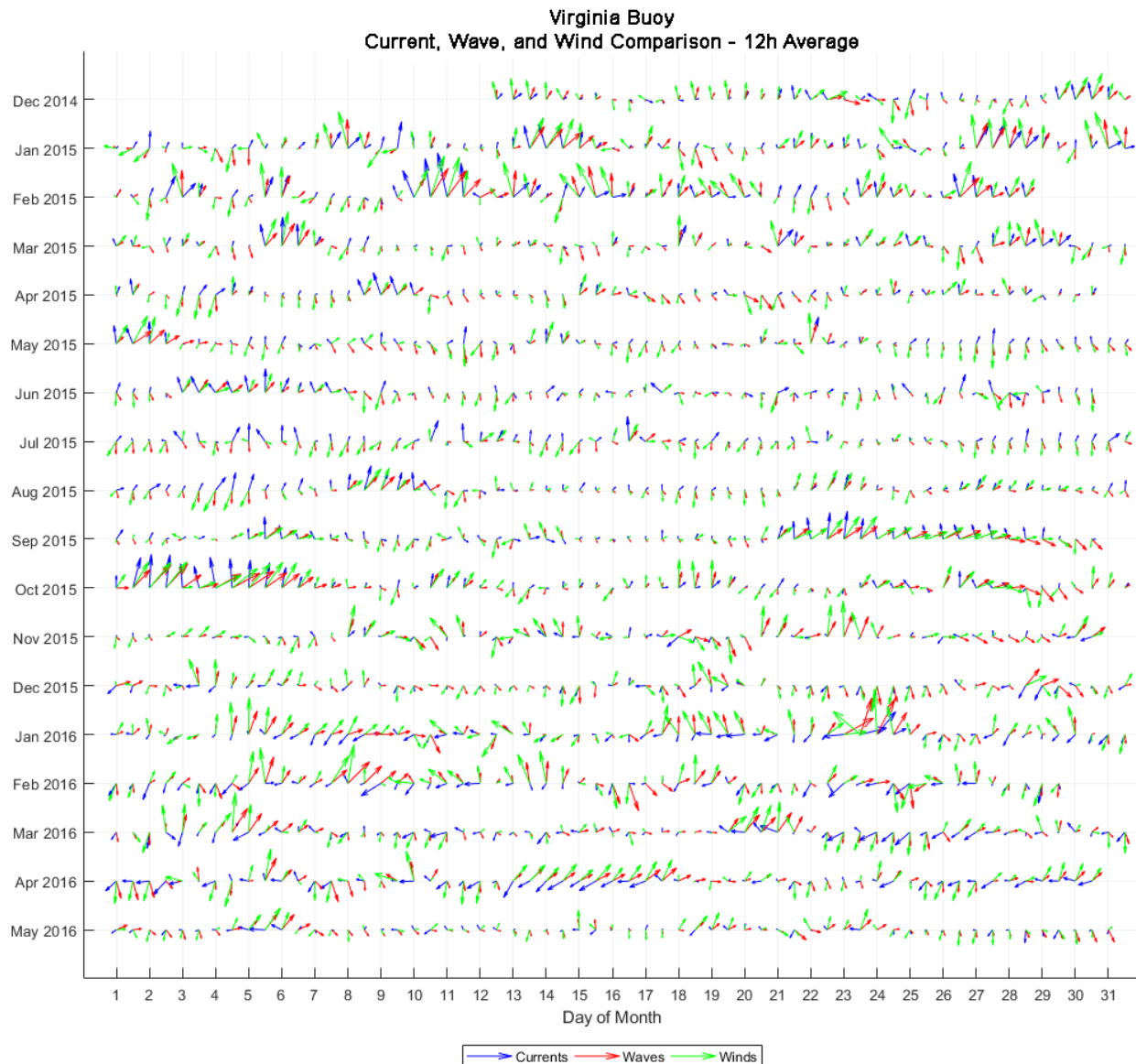


Figure 5.11. Vector plot comparison of 12-hour averaged currents, waves, and winds for the Virginia deployment.

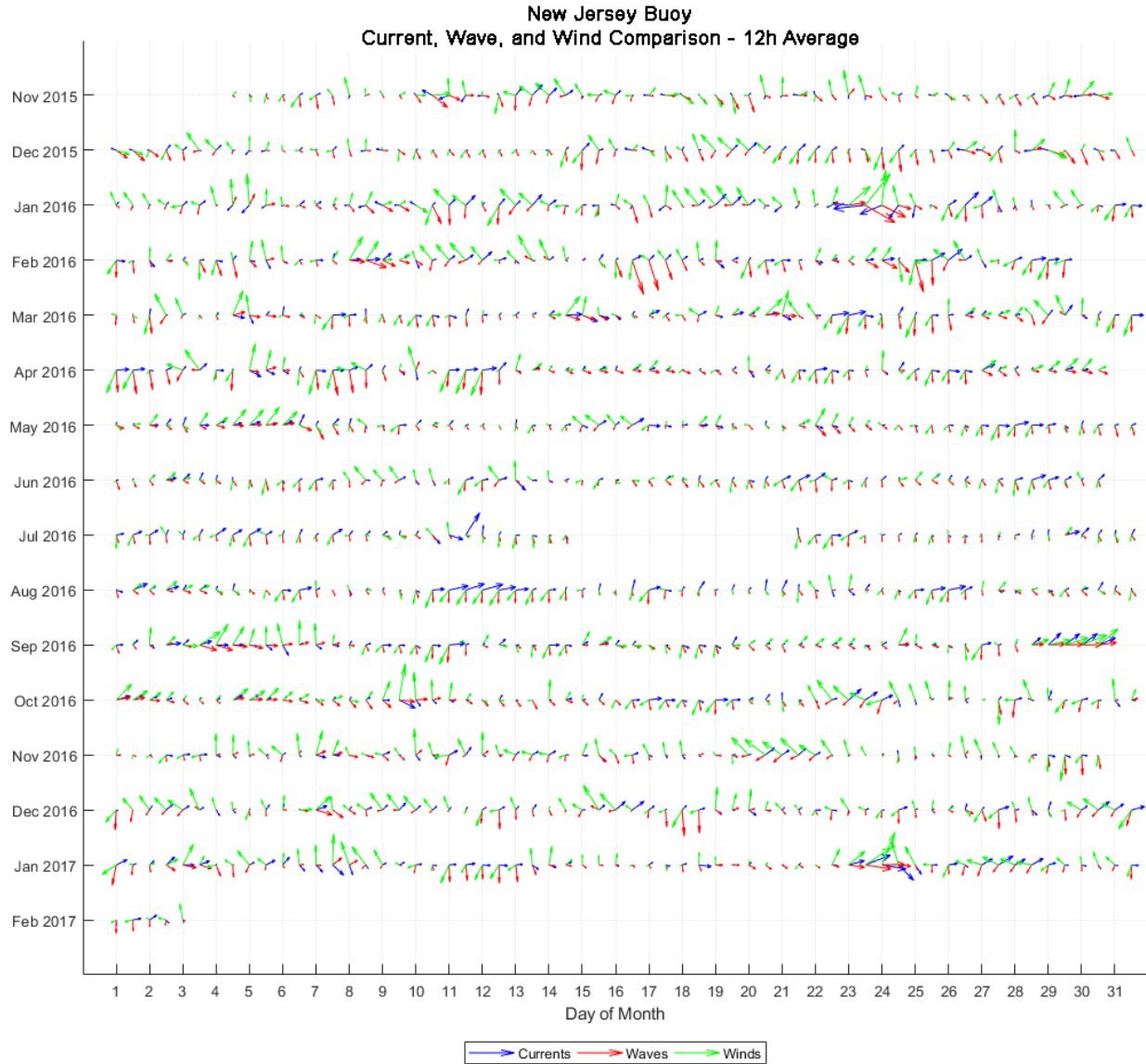


Figure 5.12. Vector plot comparison of 12-hour averaged currents, waves, and winds for the New Jersey deployment.

5.3 Ocean Current Data Trends

To evaluate trends in the ocean current data record from the two deployments, the data records were truncated (assuming the data collected after both direction shifts is inaccurate), resulting in nearly 11 months of good data for the Virginia deployment and nearly 3 months of good data for the New Jersey deployment. Figure 5.13 shows the current rose for each deployment over the trimmed data record. Boxplots of the current magnitude are shown in Figures 5.14 and 5.15 for Virginia and New Jersey, respectively. On each box, the central mark indicates the median, and the bottom and top edges of the box indicate the 25th and 75th percentiles, respectively. The whiskers extend to the most extreme data points not considered outliers; outliers are marked with a '+’.

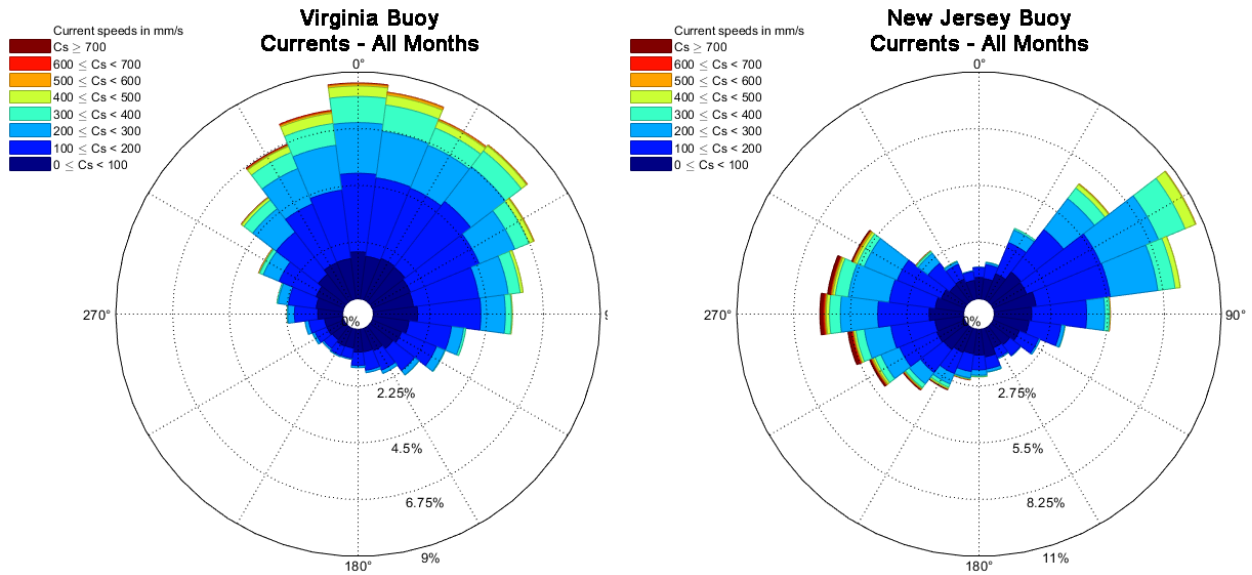


Figure 5.13. Current roses for the Virginia (left) and New Jersey (right) deployments for the trimmed data records.

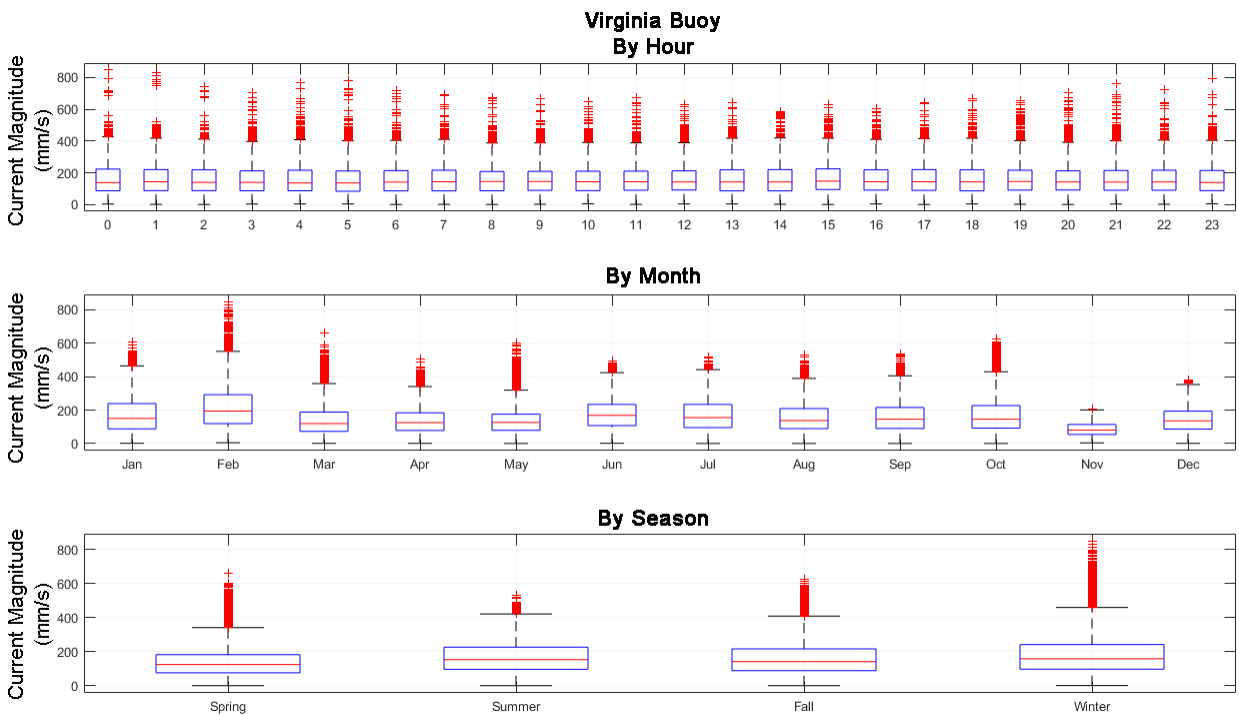


Figure 5.14. Hourly, monthly, and seasonal boxplots for the Virginia deployment trimmed data record.

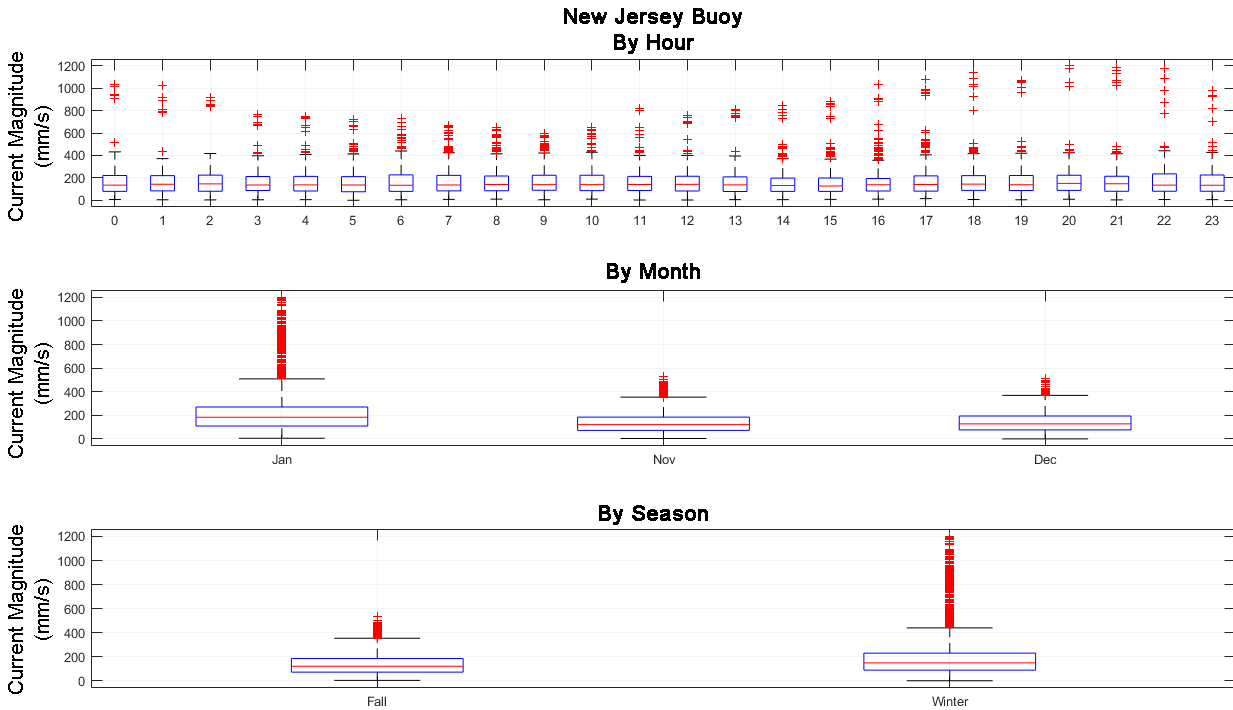


Figure 5.15. Hourly, monthly, and seasonal boxplots for the New Jersey deployment trimmed data record.

Currents during the Virginia deployment generally flow from the north-northeast with mean current speeds of 163 mm/s. The highest current speeds occur during the winter months, particularly in February, with a maximum current speed of 849 mm/s occurring on February 11, 2015. High-current outliers tend to occur during hours 0–5 and 20–23, which correspond to local afternoon through midnight.

Currents during the New Jersey deployment generally flow from the north-northeast or from the east with mean current speeds of 164 mm/s. As the dataset only covers the winter months, seasonal trends could not be inferred but the highest current speeds occurred in January, with a maximum current speed of 1202 mm/s occurring on January 23, 2016. High-current outliers tend to occur during hours 0–1 and 17–23, which correspond to local noon through evening.

5.4 Summary

While the buoys both collected wave and ocean current measurements for the full duration of the deployments off the coasts of Virginia and New Jersey, there is some concern that the ADCPs both experienced some form of error causing incorrect ocean current direction measurements. Due to the lack of availability of critical beam data, the investigation into the direction shifts focused on various analyses of the 10-minute average current magnitude and direction data and comparisons to other buoy parameters.

The current direction measurements during the Virginia deployment appear to gradually shift by 90–120 degrees several weeks following Hurricane Joaquin in October 2015. Analysis of currents at each depth bin show some inconsistencies, such as low bias in Bin 1 (surface) magnitudes and a shift in direction rotation with increasing depth, in the data following the direction shift. The inconsistencies suggest potential interference with one or more of the

instrument beams or an error in on-board data processing, potentially related to coordinate transformations. The fact that the shift did not appear to occur at a single point in time indicates that the potential for the direction shift to be from natural physical shifts is still within the realm of possibility, but possible explanations, such as a Gulf Stream eddy, seem unlikely due to the consistency and extended duration of the shift. The lack of any form of similar shift in the wave and wind data further suggests an instrument-related cause.

The current direction measurements during the New Jersey deployment appear to shift from a bimodal to unimodal direction distribution immediately following a service visit where the instrument was removed from the water for maintenance. The fact that there are inconsistencies on both sides of the direction shift, such as the minor low bias in Bin 1 and the lack of bin differences prior to the direction shift and higher error between current measurements and the model data following the shift, makes it difficult to identify which portion of the data may be more accurate based on magnitude and direction alone. Because the buoy was deployed in a shallow location very near shore, it is assumed that the tidal influence on the currents would be more evident, pointing towards the bimodal portion of the data to be more realistic. Also, since the shift occurred directly following a service visit, it is likely that there was some form of change with the instrument itself while out of water, further pointing towards the following data to be incorrect. Possible causes include not properly shutting off the instrument while out of water or a disruption of the compass calibration due to an exposure to a ferrous metal or other source of strong magnetic field.

For future buoy deployments, it is recommended that the ADCP data be archived at the instrument sample rate and the diagnostic instrument parameters such as individual beam correlations, echo intensities, and percent-good, and internal pitch, roll, and heading be archived, as well. Having this additional instrument data are crucial for identifying any data inconsistencies and potential causes and will also allow the reprocessing of the data if specific problems are identified and can be remedied.

There was also a lack of documentation on the on-board data processing for these two deployments, with general confusion surrounding what compass data (buoy or ADCP) was being used for the transformations and what information is processed and exported by the instrument and the buoy-based data acquisition system. It is recommended that these be confirmed and documented prior to future deployments.

Additional steps that can be taken during service visits to help in confirming the instruments are performing as expected include confirming measurements with nearby observations (i.e., another ADCP or shipboard readings) and confirming the calibration after servicing, if possible. Also, a recommended practice to follow when servicing any ADCP is to ensure that the instrument has been properly turned off when not in the water, minimizing potential transducer failures.

6.0 Preliminary Analysis of the Wind Profile

6.1 Wind Shear, Fluxes and Monin-Obukhov Similarity Theory

Observations from both the Virginia and New Jersey deployments indicate a strong relationship between the air-sea temperature difference and wind shear. Plots of wind shear versus the virtual air-sea temperature difference, ΔT_v , are shown in Figure 6.1 for both the Virginia and New Jersey deployments. Water temperature measurements were made with the Seabird SBE37SMP CTD sensor located in the moon pool on the stern of the buoys. Air temperature measurements were obtained from a Rotronic MP101A sensor located roughly 2.7 m above the deck of the buoy. The wind shear was estimated as the difference between the lidar wind speed at the 90 m level and the surface cup anemometers, normalized by the height of 90 m. Positive temperature differences, $\Delta T_v > 0$, correspond to stable stratification. Figure 6.1 shows that the wind shear is small under unstable conditions, then increases rapidly for $\Delta T_v > 0$.

For the analysis presented here we attempted to minimize the effects of nearby land surfaces by restricting wind directions to open water fetches. This helped to reduce the scatter in the New Jersey results, but had little effect on the Virginia results. This is consistent with the Virginia buoy having been deployed much further from shore.

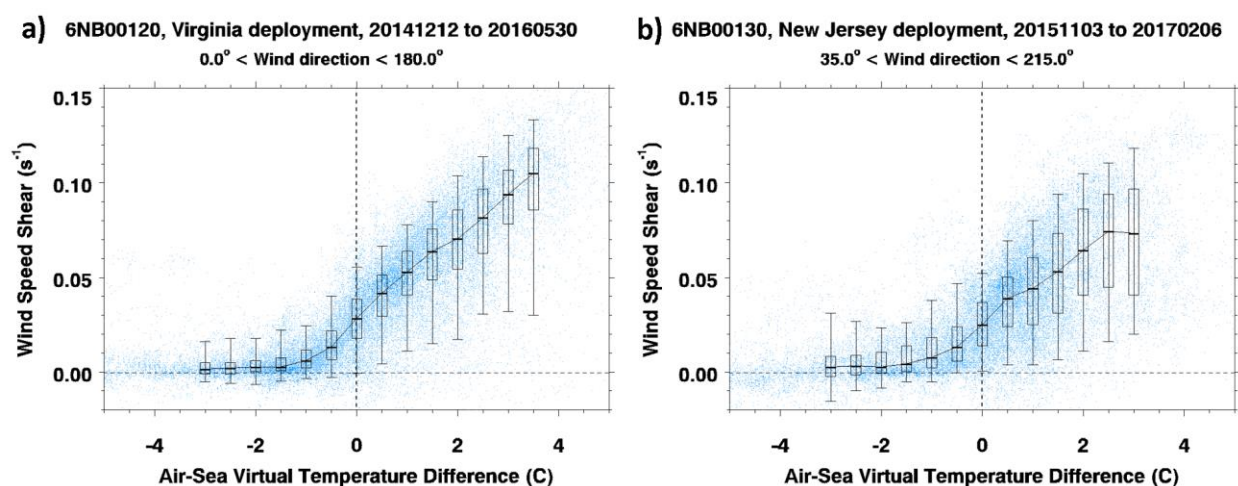


Figure 6.1. Wind speed shear as a function of the air-sea temperature difference for a) the Virginia deployment and b) the New Jersey deployment.

The relationship between wind shear and air-sea temperature difference was evaluated in the context of Monin-Obukhov (MO) similarity theory. Turbulent fluxes of heat and momentum were estimated using a bulk parameterization method developed at the Woods Hole Oceanographic Institution, with MATLAB code obtained from https://woodshole.er.usgs.gov/operations/sea-mat/air_sea-html/index.html. This code, which uses a simplified version of the Fairall et al. (1996) TOGA/COARE algorithm, makes use of MO theory and the Dyer parameterization (Dyer 1974) to estimate vertical fluxes of heat and momentum above the ocean surface from standard buoy atmospheric and near-surface oceanographic measurements. We note this does not include lidar observations, as these are non-standard measurements.

It is not possible to directly evaluate the accuracy of the fluxes predicted by the bulk method given the available measurements. However, the bulk method assumes that the resolved non-

dimensional wind shear is a universal function of atmospheric stability. Thus, it is possible to compare wind shear predicted by the bulk method with direct observations of wind shear from lidar and surface measurements.

The non-dimensional wind shear used in the bulk method is given by

$$\phi = \frac{kz}{u_*} \frac{\partial U}{\partial z}, \quad (6.1)$$

where z is the height of the measurement, U is the wind speed at height z , and k is von Kármán's constant, which we take to be 0.4 for this analysis. The bulk method makes use of the Dyer (1974) parameterization

$$\phi_{Dyer}(z/L) = \begin{cases} (1 - 16z/L)^{-1/4} & \text{for } z/L < 0 \\ 1 + 5z/L & \text{for } z/L > 0 \end{cases}, \quad (6.2)$$

where z/L is the stability parameter and L is the Obukhov length. The Obukhov length is given by

$$L = -\frac{\bar{\theta}_v u_*^3}{kg(\overline{w'\theta'_v})_s}, \quad (6.3)$$

where $\bar{\theta}_v$ is the mean virtual potential temperature, u_* is the friction velocity, g is the acceleration of gravity, and $(\overline{w'\theta'_v})_s$ is the kinematic virtual heat flux evaluated at the surface.

The friction velocity is given by

$$u_* = \left((\overline{u'w'})_s^2 + (\overline{v'w'})_s^2 \right)^{1/4} \quad (6.4)$$

The bulk method provides estimates of $(\overline{w'\theta'_v})_s$, $(\overline{u'w'})_s$, and $(\overline{v'w'})_s$, from which u_* and L are computed. This then enables us to compute the wind shear predicted by the bulk method from Equation (6.1), i.e.,

$$\left(\frac{\partial U}{\partial z} \right)_{MO} = \frac{u_*}{kz} \phi(z/L) \quad (6.5)$$

where $z = 4$ m is the height of the anemometer above the ocean surface. The observed wind shear is computed using the wind speeds measured by the lidar at 90 m above the surface, and the cup anemometers on the buoy, i.e.,

$$\left(\frac{\partial U}{\partial z} \right)_{obs} = (U_{lidar}^{90m} - U_{cup}) / 90m \quad (6.6)$$

where U_{lidar}^{90m} is the lidar wind speed at 90 m and U_{cup} is the wind speed from the cup anemometers on the buoy. We can then compare this prediction against the observed wind shear from the lidar and surface measurements.

Figure 6.2 shows a comparison between observed parameters (surface wind speed, air-sea temperature difference, and wind shear) and quantities estimated from the bulk method (friction velocity, sensible heat flux, and wind shear) for the Virginia buoy during the month of January 2015. The top panel shows that the friction velocity from the bulk method is highly correlated with the observed wind speed from the cup anemometers on the buoy, as expected. Also, the middle panel in Figure 6.2 shows that observed air-sea temperature difference and the sensible heat flux from the bulk method are strongly anti-correlated. The bottom panel shows a comparison between $(\partial U / \partial z)_{MO}$ and $(\partial U / \partial z)_{obs}$. Comparing the top and bottom panels, we see that the bulk method wind shear, $(\partial U / \partial z)_{MO}$, is strongly correlated with the observed surface wind speed, but poorly correlated with the observed wind shear, $(\partial U / \partial z)_{obs}$. The bulk method also predicts much larger wind shears compared to the observations. In fact, the bulk method predicts large wind shears even under unstable conditions, i.e., when $\Delta T_v < 0$. From Figure 6.1 we see that $(\partial U / \partial z)_{obs}$ tends to remain close to zero whenever $\Delta T_v < 0$, and increases rapidly with ΔT_v for $\Delta T_v > 0$. The bulk method wind shear, $(\partial U / \partial z)_{MO}$, does not show this same behavior. Rather, it just tends to follow the surface wind speed.

Figure 6.3 shows a scatter plot of $(\partial U / \partial z)_{MO}$ versus $(\partial U / \partial z)_{obs}$ for the Virginia and New Jersey deployments. In both cases, the correlation between these quantities is quite poor (essentially zero). This suggests a problem with MO similarity theory, the Dyer parameterization, or our wind shear observations. We point out that the observed wind shear may be biased low because we used the difference between the surface anemometer and 90 m range gate from the lidar. Ideally, the wind shear should be estimated closer to the surface. For this analysis we avoided the use of the lowest lidar range gate (at 55 m) because previous analysis has shown a significant slow bias at that level. Further analysis is required to understand the large discrepancies between $(\partial U / \partial z)_{MO}$ and $(\partial U / \partial z)_{obs}$.

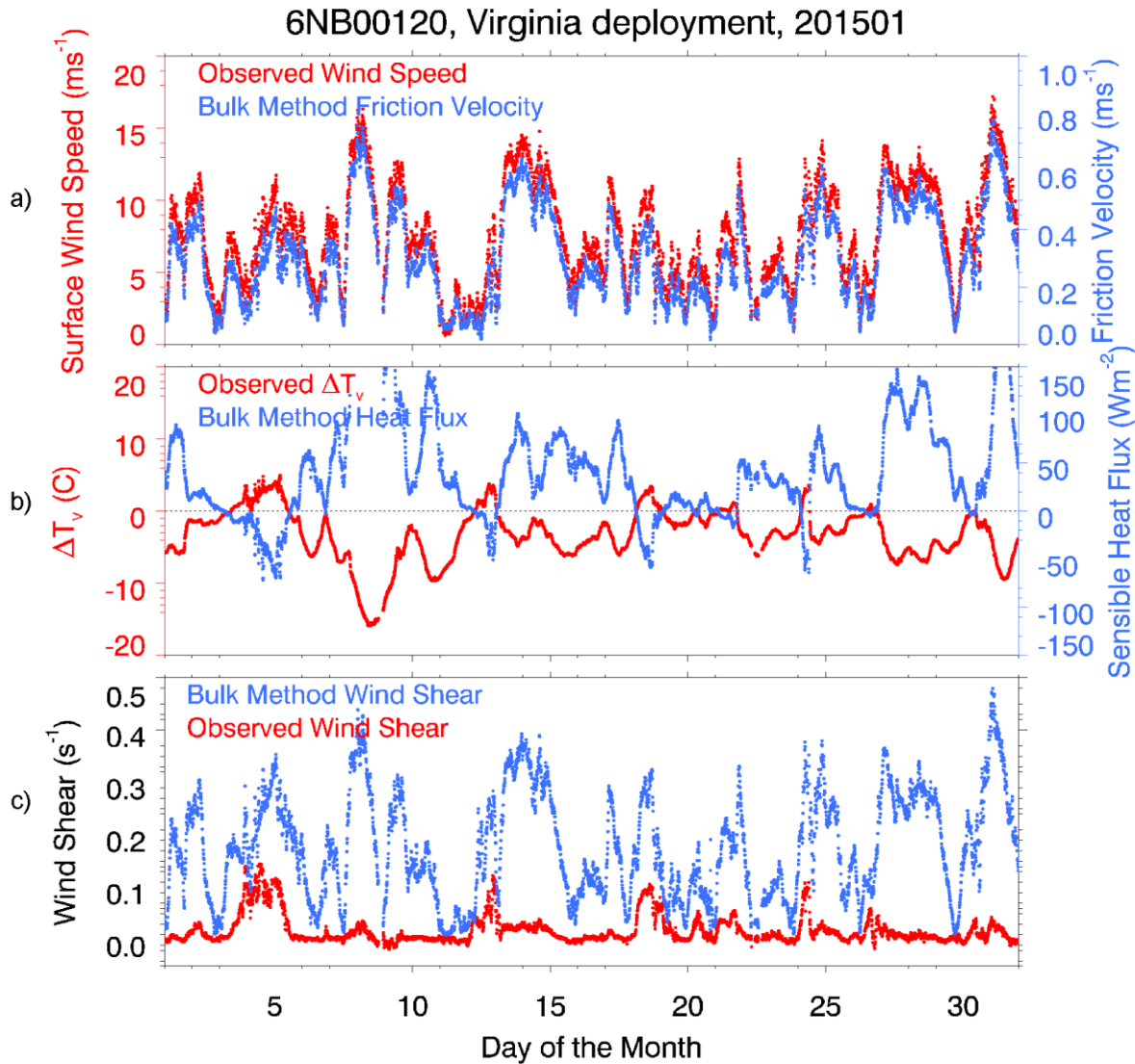


Figure 6.2. Comparison between observations and the results of the bulk method for January 2015 during the Virginia deployment. a) Observed surface wind speed (red) and the friction velocity from the bulk method (blue). b) Observed air-sea virtual temperature difference (red) and the sensible heat flux from the bulk method (blue). c) Observed wind shear (red) and the wind shear implied by the bulk method (blue).

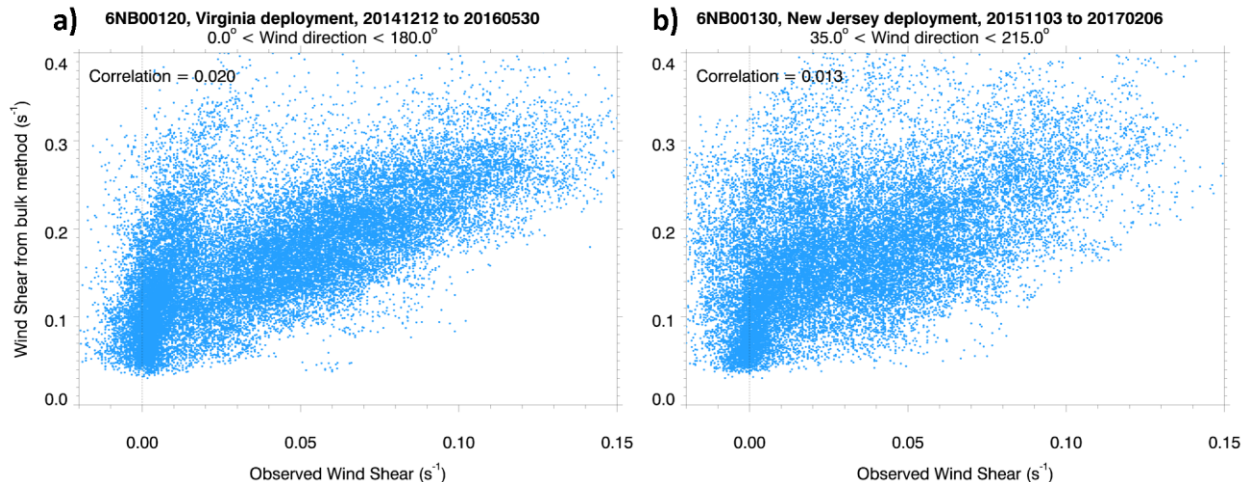


Figure 6.3. Scatter plots showing the bulk method wind shear versus the observed wind shear during a) the entire Virginia deployment and b) the entire New Jersey deployment.

6.2 Summary

Plots of wind shear versus the air-sea virtual temperature difference show a clear relationship, such that under unstable conditions ($\Delta T_v > 0$) the wind shear is small, but then increases rapidly with ΔT_v for $\Delta T_v > 0$ (i.e., stable stratification). Similar behavior was observed from both buoys, but the New Jersey buoy exhibited more scatter. For the New Jersey buoy, we found that the scatter could be reduced by restricting the analysis to include only those wind directions coming from offshore.

The relationship between wind shear and air-sea virtual temperature difference was evaluated in the context of MO similarity theory. This required estimation of turbulent fluxes from the available buoy measurements. This was accomplished using the bulk parameterization algorithm from the Wood Hole Oceanographic Institute. The code implements a simplified version of the Fairall et al. (1996) TOGA/COARE algorithm to estimate fluxes from standard surface meteorological and oceanographic measurements. Our results showed that the retrieved friction velocity is highly correlated with the observed wind speed from the cup anemometers, and the retrieved sensible heat flux is strongly anti-correlated with the observed air-sea temperature difference. These observations are consistent with our expectations.

Turbulent fluxes from the bulk method were used to compute the wind shear predicted by MO similarity theory. These estimates were then compared to direct measurements of wind shear using the lidar wind speed at 90 m and the surface anemometers. We found that the predicted wind shear is strongly correlated with the observed wind speed from the cup anemometers. However, the correlation between the observed and predicted wind shear was found to be essentially zero. This suggests a problem with MO similarity theory, the Dyer parameterization, or our wind shear observations. Further work is needed to reduce uncertainty and identify the source of the discrepancy.

7.0 Extraction of Turbulence from Vindicator Doppler Lidars

Wind velocity, temperature, relative humidity, and turbulence are key parameters that are measured during a wind resource assessment campaign. Doppler lidars are frequently used in the wind energy industry for wind resource assessment, wind turbine control, and continued site assessment. The accuracy of average wind speed and direction measurements have been thoroughly validated in various field campaigns and consultant reports, with an uncertainty less than 2%. Lidars are also included in the latest edition of IEC 61400-12-1 as one of the standard instruments for power curve assessment and can be used as a stand-alone device. Because they can provide a vertical profile of winds from 40 m to 300 m above ground level (AGL, depending on aerosol loading and type of lidar), they are an attractive and cheaper alternative for deployment in challenging locations (offshore/complex terrain). Although the average 10-minute winds are considered accurate, due to the inherent volume averaging of lidar measurements over a range gate and to relatively long sampling intervals, estimates of turbulence from lidars have been more challenging than point observations from an in situ sensor (such as a sonic or cup anemometer). Turbulence intensity (TI) and turbulence kinetic energy (TKE) are two such parameters that are frequently used either in the wind energy industry or academia to assess the stochastic nature of the atmosphere within the atmospheric boundary layer. TI is an important parameter to assess the potential loads on a wind turbine. According to IEC 61400-1 guidelines, a wind turbine should be designed for different classes of turbulence intensities. Apart from TI, it is also important to measure the mean wind speed gradient, which is dependent on velocity covariances (Wyngaard 2010). Because momentum fluxes are produced in part by the mean wind gradient, wind shear can have considerable impact on wind turbine moments. TKE also influences the wind turbine loads significantly. In an offshore environment, Doppler lidars are generally deployed on a buoy. A motion-compensation algorithm is applied to the lidar datasets to account for the motion induced by the waves. Although the mean wind speeds are considered reasonably accurate, wave motion causes additional complication while extracting turbulence during such campaigns.

In this report, a benchmark study on the ability of DOE Vindicator Doppler lidars (hereafter referred to as Vindicator lidars) to measure turbulence is evaluated. In April–May 2015, two Vindicator lidars were deployed near the Boulder Atmospheric Observatory (BAO) alongside a 300 m tall meteorological tower during the eXperimental Planetary boundary layer Instrumentation Assessment (XPIA) field campaign (Lundquist et al. 2017). This allowed for a thorough evaluation of the Vindicator lidars' performance to estimate wind speed and various turbulence measurements. Various turbulence retrieval methods were tested with the lidar dataset to provide a benchmark on the accuracy level of such turbulence estimates for future campaigns. In Section 7.1 turbulence mathematical equations used in this report are discussed. Section 7.2 details the XPIA field campaign. Section 7.3 provides comparison of turbulence measurements (both TI and TKE) without motion compensation from various algorithms with an uncertainty framework. Conclusions are provided in Section **Error! Reference source not found.**

7.1 Mathematical Preliminaries

Below we provide some mathematical relations related to turbulence, which are used in the following sections.

We define the wind vectors as $\mathbf{v}=(u,v,w)$, such that u (longitudinal component) is in the mean wind direction, v (transverse component) is perpendicular to the mean wind direction, and w is

the vertical direction (positive upwards). If we consider that the fluctuations of the wind vector are homogeneous in space, i.e., the statistics of turbulence are invariant with respect to location, then the auto and cross covariance functions can be defined in terms of the separation vectors as,

$$R_{ij}(\mathbf{r}) = \langle v'_i(\mathbf{x}) v'_j(\mathbf{x} + \mathbf{r}) \rangle \quad (7.1)$$

where $R_{ij}(\mathbf{r})$ is the auto or cross correlation function for each wind vector and \mathbf{x} is the position vector in the three-dimensional (3D) Cartesian coordinate system, \mathbf{r} is the separation vector, $\langle \rangle$ denotes ensemble averaging, and $v'(\mathbf{x})$ denotes the fluctuations about the ensemble average. The two-point statistic can be used to calculate a single point turbulence statistic at $\mathbf{r} = 0$, as

$$R = \begin{bmatrix} \langle u'^2 \rangle & \langle u'v' \rangle & \langle u'w' \rangle \\ \langle v'u' \rangle & \langle v'^2 \rangle & \langle v'w' \rangle \\ \langle w'u' \rangle & \langle w'v' \rangle & \langle w'^2 \rangle \end{bmatrix} \quad (7.2)$$

where the diagonal terms are the variances of the respective wind vectors and the off-diagonal terms are the covariances. We can also define the spectral velocity tensor as the Fourier transform of $R_{ij}(\mathbf{r})$

$$\varphi_{ij}(\mathbf{k}) = \frac{1}{(2\pi)^3} \int R_{ij}(\mathbf{r}) e^{i\mathbf{k}\cdot\mathbf{r}} d\mathbf{r} \quad (7.3)$$

where $\varphi_{ij}(\mathbf{k})$ is the 3D spectral velocity tensor and \mathbf{k} is the wave number in all three directions. Practically it is not possible to measure a spectral velocity tensor, as we cannot measure at all points in a 3D space. Alternatively, a turbulence model such as Mann (1994) can be used to replicate the true atmospheric conditions by fitting the model spectra to sonic anemometer data. This method is now being vigorously researched to estimate turbulence from all types of Doppler lidars. The TKE is defined as

$$TKE = \frac{1}{2} (\langle u'^2 \rangle + \langle v'^2 \rangle + \langle w'^2 \rangle). \quad (7.4)$$

In wind energy, a more frequently used statistic as discussed above is TI, which is defined as

$$TI = \frac{\sigma_u}{u} \quad (7.5)$$

where TI is the turbulence intensity and $\sigma_u = \sqrt{\langle u'^2 \rangle}$ is the standard deviation of the horizontal wind speed u . As discussed above, it is important to measure the tensor R_{ij} accurately to provide insight into wind turbine loads and variability within the atmospheric boundary layer processes.

7.2 Measurement Campaign

During the XPIA field campaign several remote sensing instruments were validated alongside the 300 m BAO tower (Lundquist et al. 2017). Figure 7.1 shows the location of the two Vindicator lidars near the BAO tower and approximate distance. The met-mast was fitted with sonic anemometers at several levels (50, 100, 150, 200, 250, and 300 m AGL). The Vindicator lidars were configured to measure at heights 55, 60, 80, 100, 120, and 150 m AGL. The two Vindicator lidars were continuously collecting data from April 8, 2015, to May 29, 2015. One of the Vindicator lidars was installed on top of a motion platform, which was operated during favorable time periods. Further information on the Vindicator lidars' motion-compensation algorithm and performance can be found in Newsom (2016). The sonic anemometer datasets were interpolated to match the heights of the Vindicator lidar heights. The errors due to the interpolation are considered negligible and are not included in the analysis below.

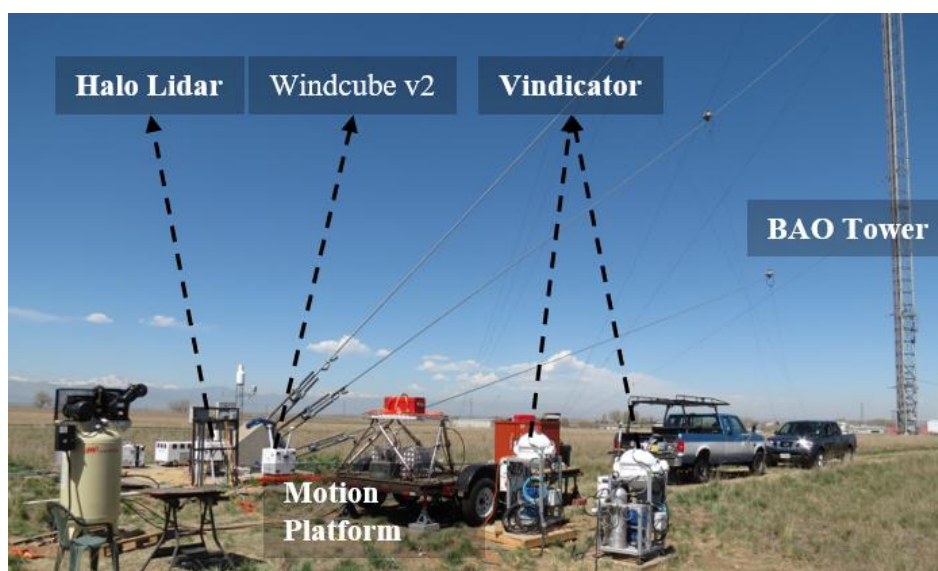


Figure 7.1. Location of the Vindicator lidars near the BAO tower during XPIA field campaign in 2015.

7.3 Lidar Turbulence Retrieval Algorithms

Due to the inherent volume averaging within a given range gate, beam separation during Doppler beam swinging (DBS)-type scans and sampling frequency relative to turbulence time scales, many algorithms have been proposed to accurately estimate turbulence at a given height. Five algorithms to estimate TKE and TI were implemented on the Vindicator lidar datasets. First, a standard algorithm that uses 1 Hz wind vector measurements from the Vindicator lidars' processed data are used to calculate the TI and TKE based on definitions in Section 7.1. The second method is based on the theory discussed in Kumer et al. (2016), which points to the effect of the true frequency of the wind vector estimates as a result of the update rate of the radial velocity measurements. For example, in a Windcube v2 Doppler lidar, radial velocity measurements at four cardinal directions (plus one vertical beam) are used to estimate one wind vector profile. Each radial velocity measurement takes roughly 0.8 seconds, resulting in a true sampling interval of the wind vector to be every 4 seconds. Kumer et al. (2016) show better correlation in the spectral domain when picking wind vector estimates based on the true frequency to sonic anemometer measurements. Method 3 is based on Newman et al. (2016),

which provides a modified set of equations considering the effect of beam separation. This beam separation results in contamination of the wind vector components. The main reason for the deviations in the TI measurements is the different measurement principles between lidars and sonic anemometers: while the typical met-mast wind sensors, i.e., cup and sonic anemometers, are in situ, a lidar measurement is related to a volume with significant dimensions. Evaluating wind velocity variances over the measurement volume leads to cross-contamination between wind velocity components. In a turbulent wind field, the error comes from combining the radial velocities from spatially separated lidar beams. Assuming Taylor's frozen turbulence hypothesis (Taylor 1938), and considering the distance between two measurement points and the time needed for the mean wind to cover the distance, the wind velocities between the two points are expected to be well correlated. Whenever the wavelength of the measured turbulence equals $2/n$ times the separation distance, with $n = 1, 3, 5, \dots$, a resonance effect occurs. The wind speed component being measured cannot be detected in these cases and is replaced by contributions of other wind speed components. Figure 7.2 shows the effect of fluctuations of u and w on the lidar radial velocity measurement (further explanations can be found in Kelberlau and Mann 2019). Method 4 tackles this issue by fitting a spectral model to the sonic anemometer data and estimating the 3D spectral velocity tensor (Mann et al. 2010). This technique provides estimates of the entire R_{ij} tensor but needs sonic anemometer measurements at all heights to calculate required input variables (dissipation rate, length scale, and an anisotropy parameter). Because the Vindicator lidar spectra is questionable, the need for a sonic anemometer at all heights is one of the major drawbacks for practical implementation of this method for stand-alone Vindicator lidar measurements. The algorithm still shows considerable errors during stable and unstable atmospheric conditions (Sathe et al. 2011). Finally, a physics-based machine learning approach using various input features extracted from the lidar data to estimate TKE was also tested. Data-driven machine learning approaches such as the random forest (RF) methods are particularly skilled at pattern recognition and bias correction and have been used for various meteorological applications (Hsieh and Tang 1998; McGovern et al. 2019). Multiple studies have shown that machine learning algorithms perform well when tasked with wind speed forecasting on a variety of timescales (Bilgili et al. 2007; Chen et al. 2019). Therefore, the efficacy of such models to estimate TKE from Vindicator lidars during XPIA was also tested.

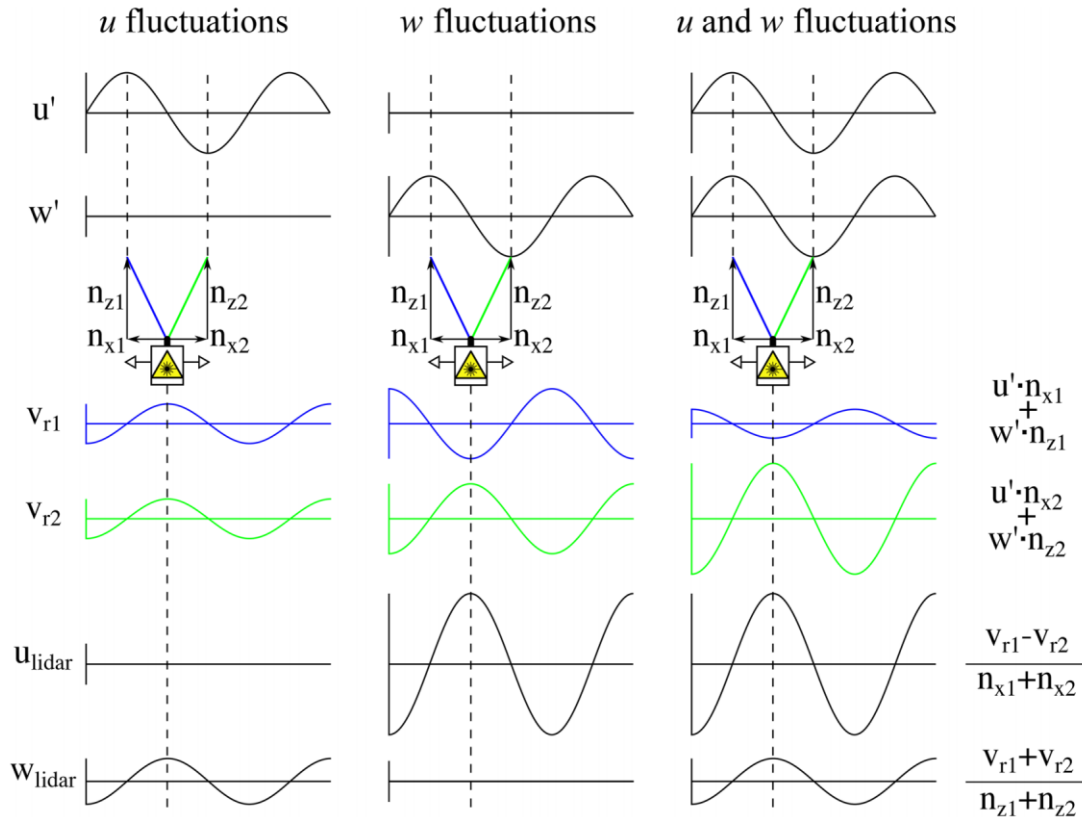


Figure 7.2. Effect of cross-contamination between the wind components using the lidar DBS measurement technique (Kelberlau and Mann 2019).

In order to assess the dependence of lidar turbulence errors on stability, errors were categorized according to the Obukhov length scale (L), as defined in Equation (6.3). The various stability classes were defined as ranges of L , shown in Table 7.1.

Table 7.1. Stability classification based on L thresholds (Sathe et al. 2011).

Stratification	L
Very stable	$10 < L < 50$
Stable	$50 < L < 200$
Near-neutral stable	$200 < L < 500$
Neutral	$ L > 500$
Near-neutral unstable	$-500 < L < -200$
Unstable	$-200 < L < -100$
Very unstable	$-100 < L < -50$

Figure 7.3 shows the u -component power spectral density from sonic anemometers, Vindicator lidar, and Windcube v2 lidar in various atmospheric stability conditions. All the lidar measurements were rotated to match the coordinate system of the sonic anemometers prior to performing the Fourier transform. Significant differences are observed between the Vindicator lidar and sonic anemometer spectra during various stability conditions. The Vindicator lidar

spectra are calculated from the processed wind vector provided by the manufacturer. The spectra indicate that the Vindicator lidar measurements undergo significant smoothing, which was also observed by Newsom (2016). This smoothing could be done to reduce the inherent noise of radial velocity measurements from the Vindicator lidars. This will be further investigated below to estimate the optimal smoothing required for accurate turbulence estimates from such lidars.

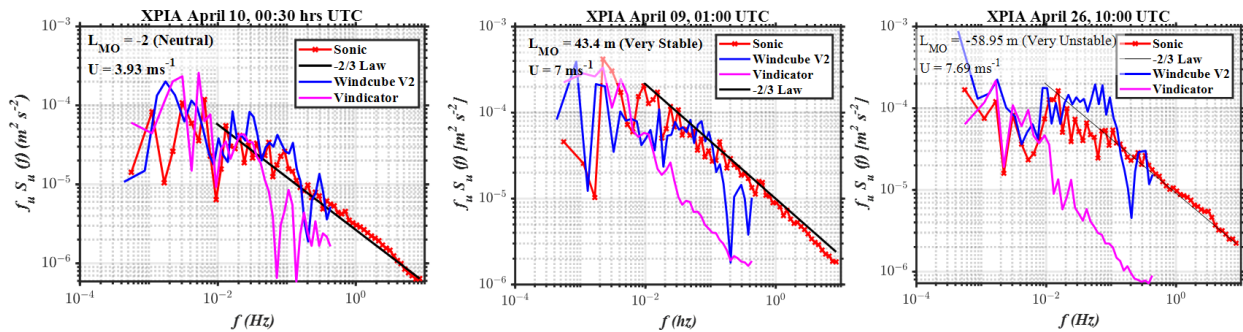


Figure 7.3. u -component power spectral density from sonic anemometer, Vindicator lidar, and Windcube v2 lidar during neutral, stable, and very unstable atmospheric conditions.

In order to process the 3D wind vector from the raw radial velocity measurements, a new wind retrieval algorithm was developed. Figure 7.4 shows estimates of all three components of wind retrieved from the raw radial velocity measurements following techniques in Browning and Wexler (1968), Krishnamurthy et al. (2013), and Newsom (2016). The new processing is referred to as PNNL processing, while the supplier estimate is referred to as OADS processing. The PNNL-processed data are much noisier than the OADS-processed data, which reflects the inherent temporal averaging done by the OADS.

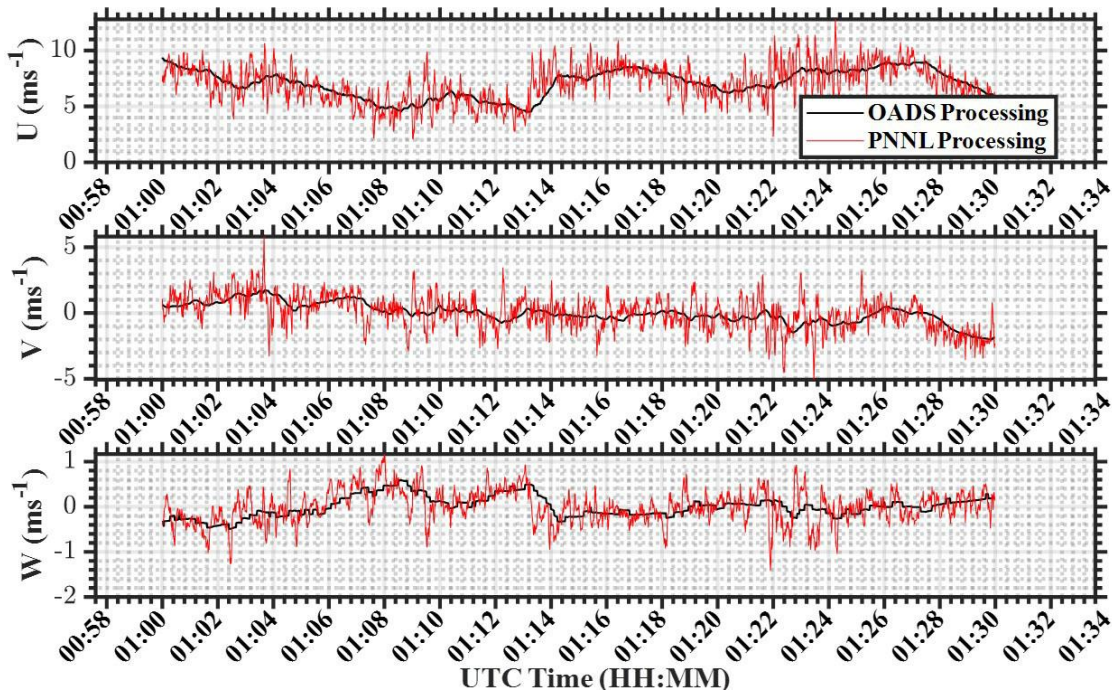


Figure 7.4. PNNL 1 Hz wind vector processing compared to OADS smoothed estimates.

Figure 7.5 shows the u -component power spectral density using the new PNNL processing, and the noise in the Vindicator lidar measurements is clearly observed at frequencies greater than 10^{-2} Hz. Lidar-derived spectra of one of the components can at certain wave numbers show lower energy values than the original wind spectrum of that component but may also show too high values due to a contribution from a different velocity component. Based on the longitudinal separation, i.e., separation along the mean wind direction, fluctuations at two points separated in line with the wind are highly correlated. The chosen wavelength of the wind fluctuations equals twice the separation distance. Based on the spacing between the lidar beams, the resonance wavelengths (Ω) can be calculated as (Kelberlau and Mann 2019)

$$\Omega = \frac{(2n-1)\pi}{D} \tag{7.6}$$

where D is the diameter of the measurement circle ($D = 2htan\varnothing$), $n = 1,2,3\dots$ are the number of modes, h is the height of measurement, and \varnothing is the half-cone angle. For the Vindicator lidars, the resonance wavenumbers in Figure 7.5 are calculated to be equal to 0.05 m^{-1} (first mode) and 0.1 m^{-1} (third mode). It can be observed in Figure 7.5 that the peaks in the spectra correspond to the first and third mode wavenumbers. This is a classic example of the effect of cross-contamination of the lidar beams, as also observed in Kelberlau and Mann (2019). Due to the small half-cone angle ($\varnothing = 15$ degrees) the effect of cross-contamination could have larger impacts on the turbulence retrievals compared to a traditional Windcube v2 lidar.

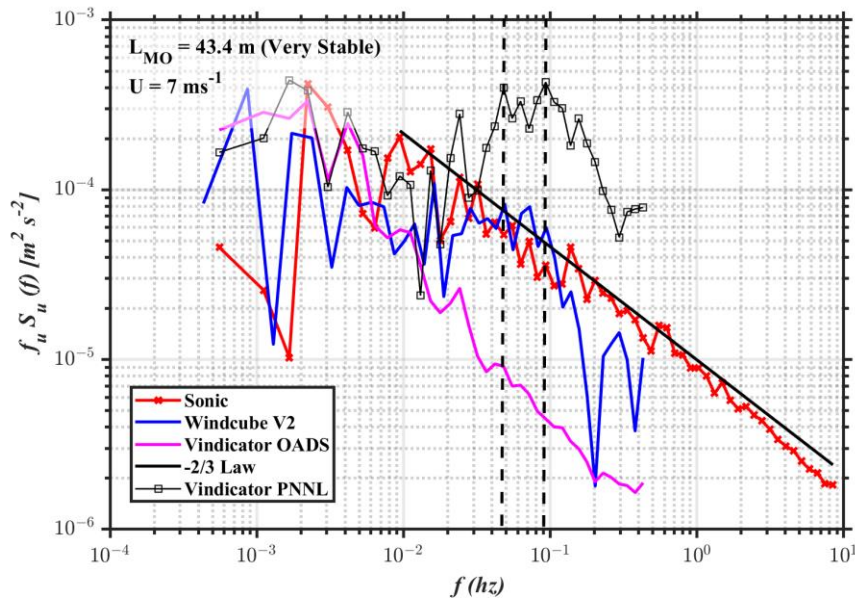


Figure 7.5. u -component power spectral density of sonic anemometer, Windcube v2, and Vindicator lidars using both OADS- and PNNL-processed 1 Hz data. The resonance wavelengths are shown by the dotted black lines.

There are no known key performance indicators (KPIs) for turbulence estimates from lidar measurements, but as a basis for comparing various algorithms Table 7.2 provides KPIs for TKE and TI estimates. The thresholds are set based on historically known lidar performances to set a benchmark for various algorithms.

Table 7.2. Key performance indicators for turbulence measurements.

Key Performance Indices for TKE or TI	Threshold for Acceptance
Coefficient of determination (R^2)	> 80%
Slope	0.9–1.1
Root-mean-square error for TKE	< 0.25 m^2s^{-2}
Bias	< 0.2 units

7.3.1 Turbulence Intensity Performance

Turbulence intensity is a standard measure of turbulence in the wind energy industry. It is one of the primary parameters used to assess the potential load a wind turbine would experience at a given site. Standard TI is based on 1 Hz wind speed estimates from the lidar and tower. Figure 7.6 shows comparisons between lidar and sonic TI for both Vindicator and Windcube lidars. The Vindicator lidars showed lower coefficient of determination (R^2) and slope values compared to the Windcube lidars. A few reasons for the difference could be due to smaller zenith angles in the Vindicator lidars, accuracy of the radial velocity, number of beams (3), and spacing between the beams (~103 degrees) to the mean wind direction. Doppler lidars inherently possess the issue of cross-contamination as discussed above; therefore, other compounding effects deteriorate the accuracy of turbulence estimates. Figure 7.7 shows profiles of various statistics for TI between the Vindicator lidar, Windcube lidar, and sonic anemometer. The averaging effect of OADS processing compared to 1 Hz PNNL processing is evident in Figure 7.6b, where the noise in the PNNL-processed data provides a much higher RMSE compared to the smoothed OADS-processed data. The PNNL-processed output matches the OADS outputs when a temporal filter of 30 seconds is applied. Despite lower rates of data availability, the OADS output shows similar results to Windcube v2.

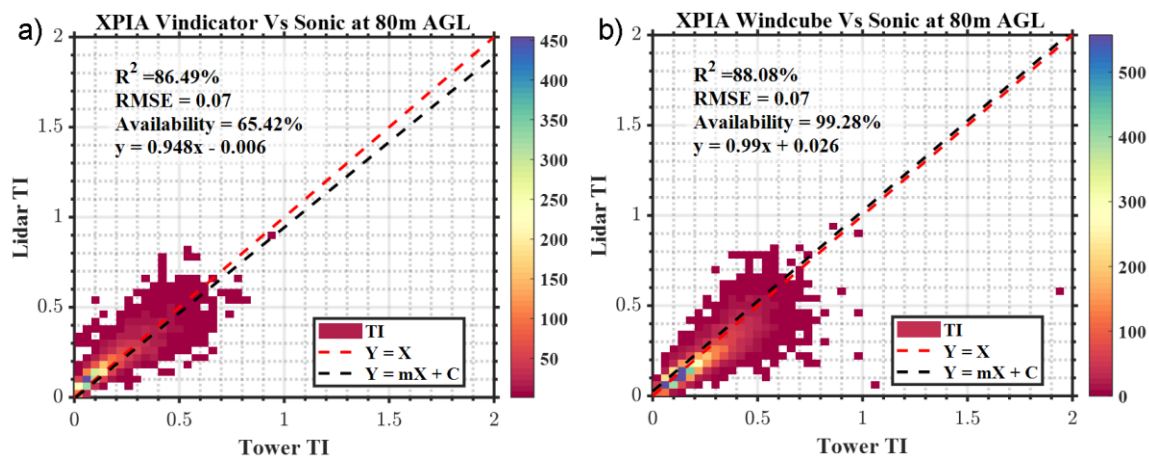


Figure 7.6. Turbulence intensity comparisons between a) Vindicator lidar, b) Windcube v2 and sonic anemometer. The color bar represents the number of samples in each bin.

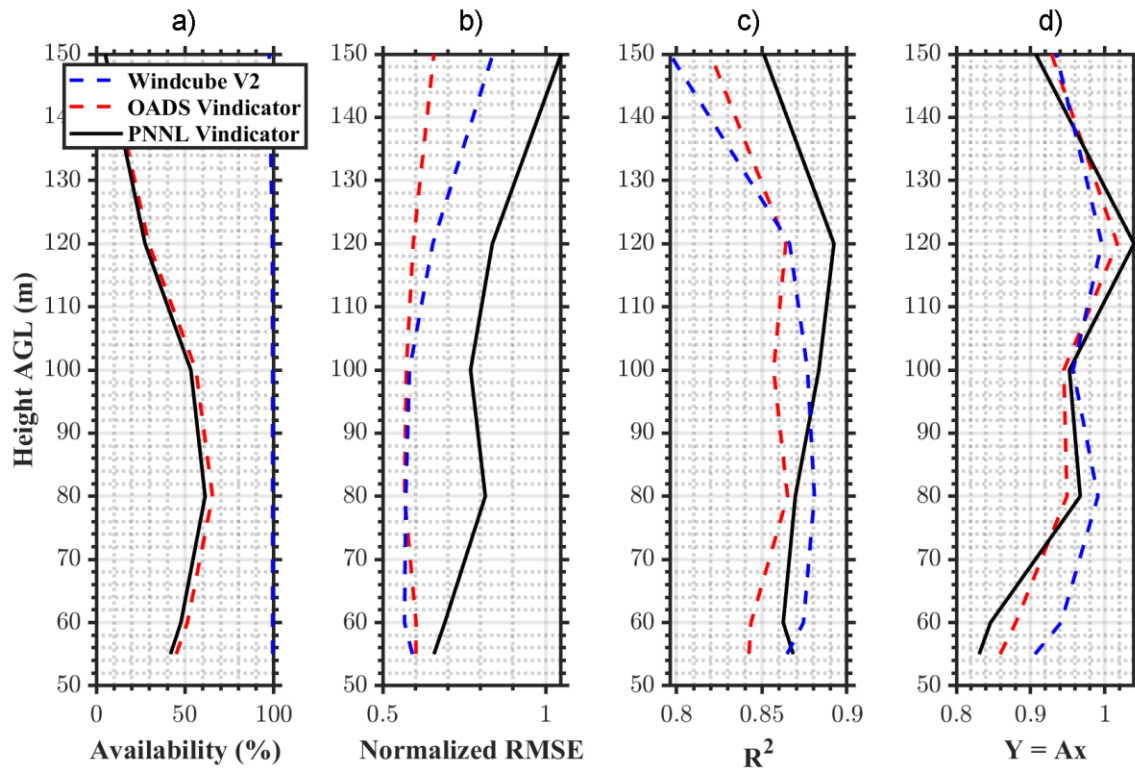


Figure 7.7. Turbulence intensity profiles of a) availability, b) normalized root-mean-square error, c) coefficient of correlation, and d) slope values from a linear fit from both Vindicator and Windcube v2 lidar compared to a sonic anemometer.

The XPIA campaign showed a range of atmospheric stability conditions. Figure 7.8a shows the MO classification as per thresholds in Table 7.2. The distribution shows several cases of very stable and neutral conditions observed near the BAO tower. The effect of atmospheric stability on the performance of TI shows the error varies considerably with respect to atmospheric stability (Figure 7.8b). The true contributions to the under/overestimation are difficult to decipher from the current dataset. But during unstable conditions, the lidar is observed to overestimate and one possible reason could be due to variance contamination discussed above. During stable conditions, the lidar underestimates, which could be due to volume averaging of the stably stratified atmosphere compared to a sonic. This performance is expected for Doppler lidars due to the inherent difference in measuring techniques compared to in situ measurement. The turbulence intensities observed at this site were low and below IEC 61400-1 Class C curves (not shown).

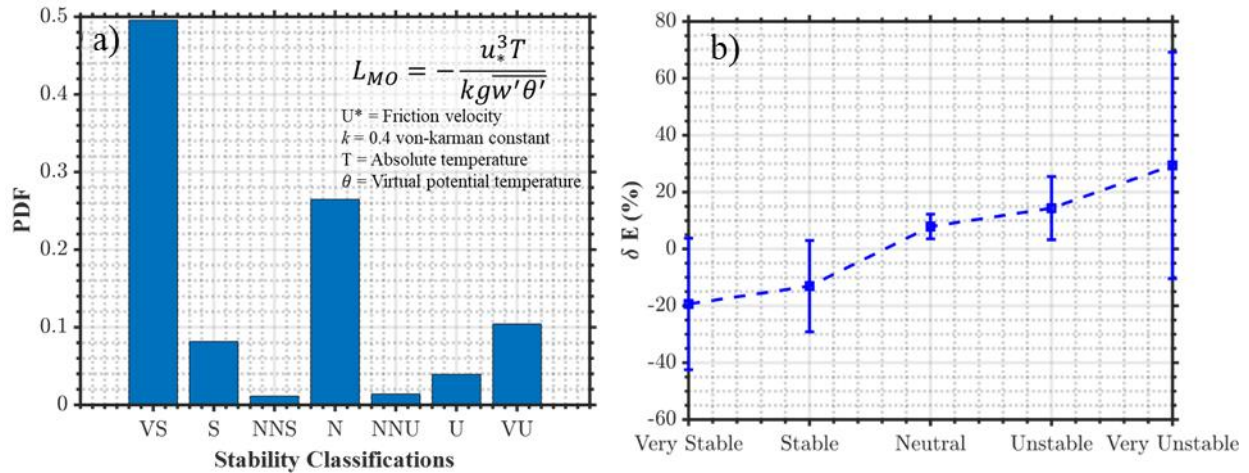


Figure 7.8. a) Atmospheric stability distribution observed during the XPIA field campaign from sonic anemometer data at the BAO tower, and b) percentage errors in turbulence intensity as a function of atmospheric stability for the Vindicator lidars. The error bars indicate 1 standard deviation.

7.3.2 Turbulence Kinetic Energy Performance

The mean TKE is estimated using the 1 Hz retrieved wind vector measurements from the Vindicator lidars. As previously described, the OADS-processed data performs averaging, and prior to proceeding with various methods available in the literature, a preliminary assessment on the effect of averaging on TKE estimates was performed. In this comparison, averaging of the raw radial velocity measurements were made prior to estimating wind vector from the three Doppler lidar beams. Figure 7.9 shows the effect of beam averaging on the lidar TKE estimates. OADS-processed data were not altered in the comparison. It is important to note that averaging not only improved certain aspects of the statistic such as the slope and intercept but also increased the data availability. With increasing averaging, the correlation coefficient decreased and the RMSE increased. All the comparisons were made in log-scale, as the TKE estimates were relatively low. Based on the results, a 2-second averaging with a statistical bias correction seems to be the best approach. But the bias is not expected to be constant—perhaps site-specific and seasonal. Therefore, a 20-second averaging is deemed appropriate to reduce the noise in 1 Hz radial velocity measurements, improve TKE slope and intercept estimates, and improve the data availability of Vindicator lidars. Further comparisons with other methods are made using a 20-second averaging of radial velocity prior to estimating the wind vector.

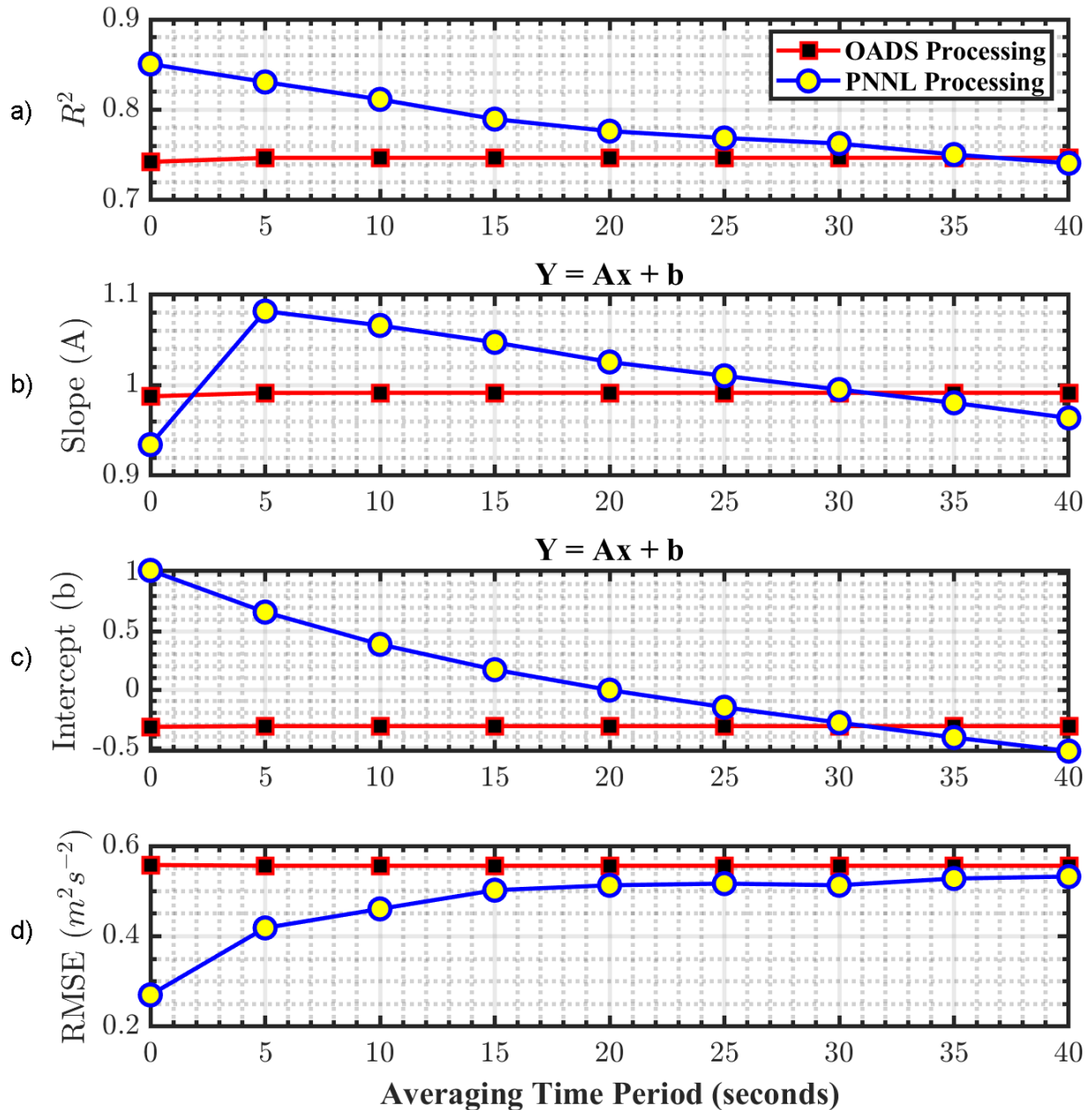


Figure 7.9. 10-minute statistical comparison between PNNL-processed and OADS-processed TKE estimates with sonic anemometer for varying averaging seconds (0 seconds refers to no averaging, i.e., instantaneous): a) coefficient of determination, b) slope of the linear regression, c) intercept of the linear regression, and d) root-mean-square error between the lidar and sonic datasets.

Method #1: The standard TKE method is based on 1 Hz wind vector measurements and is calculated using the equation below

$$TKE = \frac{1}{2}(u^2 + v^2 + w^2) \tag{7.7}$$

where $\langle u'^2 \rangle$ is the variance of the velocity fluctuations over 10 minutes. The instantaneous wind vectors are based on 20-second averaging of the raw radial velocity measurements. The impact of averaging on the TKE estimates is a function of atmospheric stability, as the variation in radial velocity is observed to be higher during unstable conditions and lower during stable conditions. Hence, the true effect of the low-pass filter on TKE estimates cannot be quantified. Therefore, an uncertainty framework is devised based on stand-alone lidar measurements in the next section to address this issue.

Method #2: The Doppler lidars generally measure each radial velocity sequentially, and therefore the true frequency of the wind vector is $1/N$, where N is the number of Doppler lidar beams. Based on the spectra, reducing the number of measurements to match the “true” frequency (0.33 Hz for the Vindicator lidars) did not improve the power spectral density compared to a sonic anemometer (as shown in Kumer et al. 2016). But nonetheless, a complete assessment of this method was warranted to test the theory.

Method #3: An approach to account for the variance contamination of the beams as shown earlier is provided in Newman et al. (2016). Although this method was meant solely for the Windcube v2, a variation of that was applied to the Vindicator lidars. The individual variances of the three wind components are shown below

$$\sigma_u^2 = \frac{2}{1+\gamma_u} \overline{u'_{DBS}^2} - \frac{(1-\gamma_w) \sin 2\varphi}{(1+\gamma_u) \cos 2\varphi} \overline{w'^2} \quad (7.8)$$

$$\sigma_v^2 = \frac{2}{1+\gamma_v} \overline{v'_{DBS}^2} - \frac{(1-\gamma_w) \sin 2\varphi}{(1+\gamma_v) \cos 2\varphi} \overline{w'^2} \quad (7.9)$$

$$\sigma_w^2 = \overline{w'^2} - \sigma_e^2 \quad (7.10)$$

where γ_u , γ_v , and γ_w are auto-covariance functions; φ is the half-cone angle; σ_e^2 is the instrumental noise (Lenschow et al. 2000); $\overline{u'_{DBS}^2}$ is the average velocity fluctuation of the u -component of wind velocity calculated from the three beams every 1 sec (unlike in Newman et al. 2016); $\overline{v'_{DBS}^2}$ is the average velocity fluctuation of the v -component calculated from the 1 Hz wind vector; and σ_u^2 , σ_v^2 , and σ_w^2 are the variance of the velocity fluctuations used for TKE estimation. Because an unbiased estimate of auto-correlations cannot be produced from the lidar measurements due to variance contamination and volume-averaging effects, the auto-correlations in u , v , and w were estimated using the sonic anemometer at the BAO tower. For this analysis, $\gamma_u = 0.9$, $\gamma_v = 0.75$, and $\gamma_w = 0.6$ was used based on the 100 m sonic anemometer measurements and were set constant for the measurement time period.

Method #4: Spectral model corrections for lidar data were proposed by Mann et al. (2010). In this method a uniform shear model (Mann 1994), which estimates the spatial spectral tensor (Φ_{ij}), is estimated by fitting the model to a sonic anemometer spectrum at each height. The lidar spatial averaging estimate is projected into the Fourier space and the lidar variances are corrected using the tensor for the Mann model (Sathe et al. 2011). Figure 7.10 shows the model fit to a sonic model and the three-parameter output (eddy dissipation rate [$\alpha \epsilon^{2/3}$], length scale [L], and anisotropy parameter [Γ]).

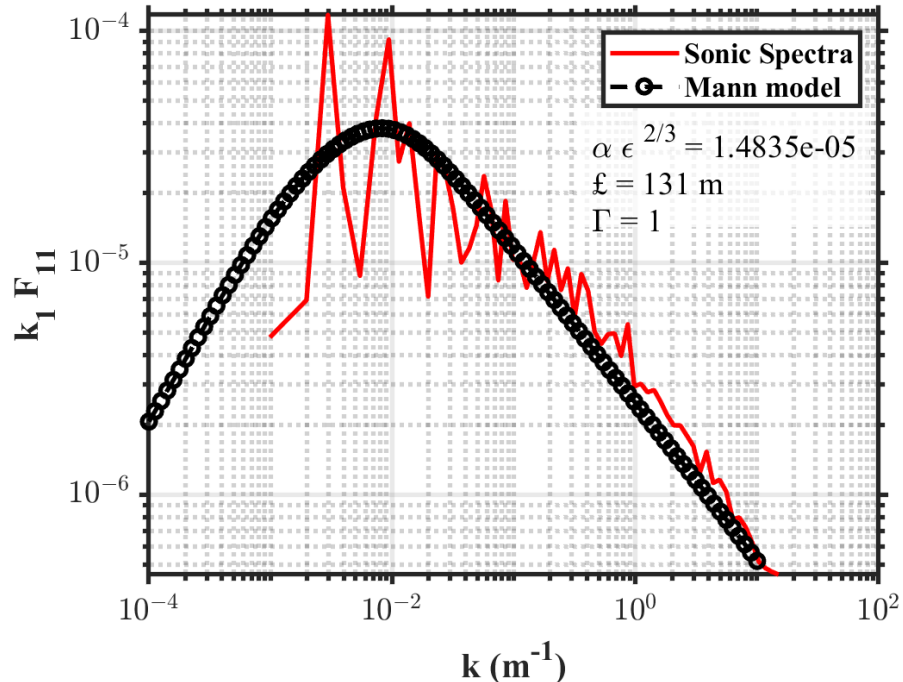


Figure 7.10. Mann uniform shear model fit to sonic anemometer at 100 m AGL on March 22, 2015, at 00 hrs. The fit parameters are also shown.

Method #5: Here, an RF model was built based on input features that can be extracted from the Doppler lidar data. Five input features were selected; namely,

- a. 10-minute average horizontal wind speed,
- b. turbulence intensity,
- c. uncertainty of TKE (shown in Section 7.3.3),
- d. wind shear, and
- e. vertical velocity variance.

All these input features were shown to improve the predictability of TKE from Vindicator lidars. The RF model parameters were optimized using Bayesian optimization to provide the least model loss (Bull 2011). Based on the optimization results, the RF model was configured with 450 learning cycles, 2 tree splits, and a learning rate of 0.25. Lasso regularization of the RF model was also performed for optimal model convergence. The RF model was first trained with 50% of the data (10% of which was used for validation) and tested on the remaining 50% of the data. The sonic anemometer TKE estimates were taken as reference for the training period. Figure 7.11 shows the unbiased predictor importance estimates for the five input features used in the model. Wind speed and TKE uncertainty estimates were the two key features that are observed to be beneficial for TKE estimation using the RF model.

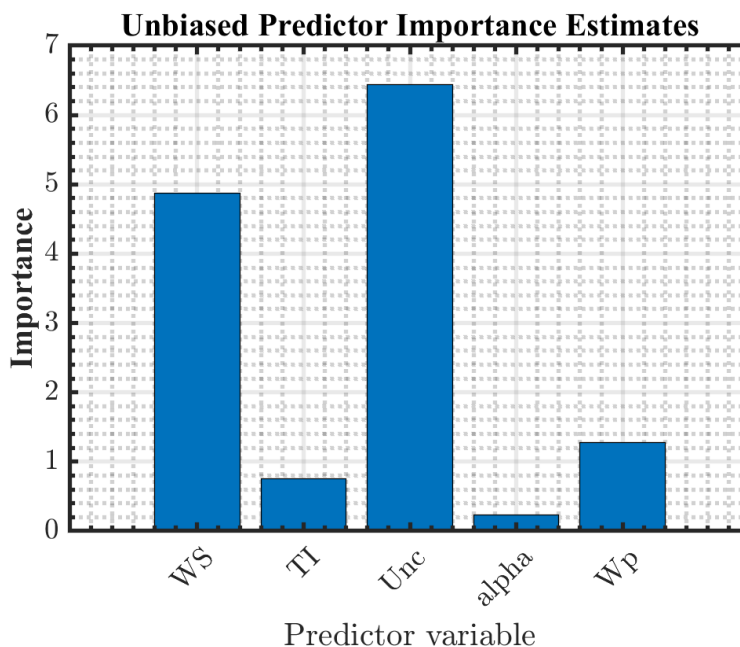


Figure 7.11. Unbiased predictor importance for TKE estimates using Vindicator lidar data. The predictor variables are WS – windspeed, TI – turbulence intensity, Unc – lidar TKE uncertainty, alpha – wind shear, and Wp – vertical velocity variance.

As shown in Table 7.3, Methods 1, 3, and 5 (i.e., the standard TKE based on 20-second radial velocity averaging, the variance contamination adjustment approach, and machine learning methods) provide the best results compared to a sonic anemometer. Of the five approaches, the RF method provides the least RMSE. The variance contamination approach shows overall improvement in the slope, RMSE, and bias. As shown above, the effect of contamination of the beams on the turbulent velocities for the Vindicator lidars is observed to be high; therefore, this method attempts to remove the effect of cross-contamination effectively. The RF model based on physical inputs does provide significant improvements in R^2 and RMSE, but since this approach uses local data to build the model, the efficacy of the same model for a different location is unknown. Therefore, if the validation of the lidar happens at the same location of the deployment, such a technique would be most beneficial. Method 4 shows the least correlation as the applicability of the spectral fit between the model and sonic is questionable due to inhomogeneous flow conditions. Method 4 also requires sonic anemometers at every height to estimate the model input parameters. Sathe et al. (2011) and Sathe and Mann (2013) detail the entire methodology and provide areas where this method fails, which coincides with the above analysis. One possible reason for poor performance of Method 2 could be due to disjunctive sampling of the velocity estimates, which is known to inflate the variance estimates. Atmospheric stability had similar effects on TKE as TI estimates from lidar measurements. A time series plot of TKE (not shown) indicated that similar trends are observed between sonic and Vindicator lidar, but the values are either higher or lower depending on how the lidar pulse probes the atmosphere. Knowing that lidars sample differently compared to sonic anemometers, it is important to understand the uncertainty of TKE from lidars. This uncertainty will aide developers and modelers in using lidar TKE estimates with confidence. The next section provides an uncertainty estimation approach using only lidar estimates, purely based on statistics.

Table 7.3. Evaluation of Vindicator lidar TKE methods compared to sonic anemometer at 100 m AGL

TKE Methods	Y = Ax + b	R ² , %	RMSE, m ² s ⁻²
Method #1	Y = 1.01x - 0.15	77.63%	0.55
Method #2	Y = 0.98x - 0.10	72.18%	0.61
Method #3	Y = 1.02x - 0.15	76.62%	0.33
Method #4	Y = 0.84 + 0.05	62.42%	0.63
Method #5	Y = 0.91x - 0.09	83.73%	0.23

7.3.3 Lidar Uncertainty Quantification

Uncertainty of turbulence quantities is seldom prioritized in measurement campaigns. How to determine confidence limits is not so clear for higher-order turbulence quantities. Since many turbulence quantities are not normally distributed, simple uncertainty formulas based on the chi-squared statistic, χ^2 , are not valid. Kendall and Stuart (1958) and Benedict and Gould (1996) present general formulas for the sampling variance of univariate and bivariate central moments based on large sample theory. Following Benedict and Gould (1996), if the exact r^{th} order central moment, μ_r , of a distribution is given by

$$\mu_r = \int_{-\infty}^{\infty} (x - \mu_x)^r dF \quad (7.11)$$

where dF is the cumulative distribution function of the variable, x , and if the r^{th} order central moment sampling statistic, m_r , is given by

$$m_r = \frac{1}{N} \sum_{i=1}^N (x_i - \bar{x})^r \quad (7.12)$$

then the sampling variance of m_r is given by

$$\text{var}(m_r) = \frac{1}{N} (\mu_{2r} - \mu_r^2 + r^2 \mu_{r-1}^2 \mu_2 - 2r \mu_{r+1} \mu_{r-1}) \quad (7.13)$$

where terms of order N^{-2} have been neglected. The 95% confidence intervals may then be constructed as $m_r \pm 1.96 [\text{var}(m_r)]^{1/2}$ and the 99% confidence interval can be evaluated as $m_r \pm 2.58 [\text{var}(m_r)]^{1/2}$. Therefore, the 95% confidence interval for the second-order central moment of U for any probability distribution shape would be given as

$$\delta_{u^2} = u^2 \pm 1.96 \left\{ \overline{u^4} - (\overline{u^2})^2 / N \right\}^{1/2}. \quad (7.14)$$

Similarly, for standard deviation of U , the 95% confidence interval can be given as

$$\delta_{\sqrt{u^2}} = \sqrt{u^2} \pm 1.96 \left\{ \left[\frac{\overline{u^4} - (\overline{u^2})^2}{4\overline{u^2}} \right] / N \right\}^{1/2}. \quad (7.15)$$

Here a resampling algorithm is used to estimate the uncertainty of turbulence quantities. The method, called the “jackknife” by Tukey (1958), is used for estimating standard errors. This method estimates the statistics based on N data subsets that leave out one measurement at a time from the original dataset. Therefore, for each subset, $i = 1, 2 \dots N$, the jackknife samples would be

$$\mathbf{x}_{jack,i} = (\mathbf{x}_1, \mathbf{x}_2, \dots, \mathbf{x}_{i-1}, \mathbf{x}_{i+1}, \dots, \mathbf{x}_N). \quad (7.16)$$

The statistical estimator, $\mathcal{G}_{jack,i}$, for each of the N subsets are calculated and the estimate of variance for the original dataset is defined as

$$var(\mathcal{G})_{jack} = \frac{N-1}{N} \sum_{i=1}^N (\mathcal{G}_{jack,i} - \overline{\mathcal{G}_{jack}})^2 \quad (7.17)$$

where

$$\overline{\mathcal{G}_{jack}} = \frac{1}{N} \sum_{i=1}^N (\mathcal{G}_{jack,i}). \quad (7.18)$$

The variance for jackknife sample i is written as

$$\mathcal{G}_i = \overline{u_{jack,i}^2} = \frac{1}{N-1} \left[\sum_{\substack{j=1 \\ j \neq i}}^N U_j^2 - 2\overline{U_{jack,i}} \sum_{\substack{j=1 \\ j \neq i}}^N U_j + (N-1)\overline{U_{jack,i}}^2 \right]. \quad (7.19)$$

Each of the variance samples above are summed once over $j = 1, 2 \dots N$ for each overall variance estimate. These jackknife replications are used to determine the variance of u^2 . This procedure can be carried for any statistic based on central moments. The measurements are also expected to be independent or uncorrelated. The data rate of the measurements should be a function of the integral time scale, practically $\frac{1}{2}T$. Because the data rate of the sonic is 20 Hz and the lidar is 1 Hz, any integral time scales longer than 2 seconds would satisfy this condition. For measurements above 50 m, this assumption is reasonable (Higgins et al. 2012). When statistical uncertainty of each measurement can be reliably calculated, the task of combining uncertainties of individual terms in an equation to estimate the overall uncertainty of the result is easily accomplished according to the guidelines of Kline and McClintock (1953) and Moffat (1982). For a given uncertainty, δx_i , the constant odds general form can be given as

$$\delta R = \left\{ \left(\frac{\partial R}{\partial x_1} \delta x_1 \right)^2 + \left(\frac{\partial R}{\partial x_2} \delta x_2 \right)^2 + \dots + \left(\frac{\partial R}{\partial x_N} \delta x_N \right)^2 \right\}^{1/2}. \quad (7.20)$$

The jitter program as provided in Moffat (1982) is used to calculate the contribution of individual uncertainty estimates on the final uncertainty value. To note, this is the uncorrelated form of errors, but some of the errors could be correlated depending on the atmospheric time/length scales (lidar can be sensing the same eddy over several seconds).

The uncertainty of TKE would account for the individual uncertainties in u , v , and w and similarly for TI, individual uncertainties of u and v . This methodology can be applied to any instrument or type of lidar, as its purely statistical. Figure 7.12 shows the time series of uncertainty and TKE estimates from Vindicator lidar. It can be observed that the uncertainty from lidar measurements is calculated to be higher when the lidar TKE deviates most from sonic TKE estimates.

Figure 7.13 shows the change in TKE between lidar and sonic compared to lidar TKE estimates. With increasing deviation, the lidar uncertainty also tends to increase. The linear fit is just an indication to show the increasing uncertainty with higher deviations, but the fit appears more non-linear. Further additions to uncertainty to account for the lidar equations and noise as per Boccippio (1995), Lenschow et al. (2000), Thiébaux and Zwiers (1984), and Newsom et al. (2017) are being considered and is a part of future work. The effect of integral time/length scales in the uncertainty estimates is an important consideration, as the scales measured by the sonic and lidar are not equal. Sonic anemometer measures much smaller turbulence scales, while the lidar measures length scales at least greater than the range gate of the lidar. Therefore, the sample size for turbulence estimates for each instrument should depend on integral length scales that the instrument is capable of measuring (Thiébaux and Zwiers 1984).

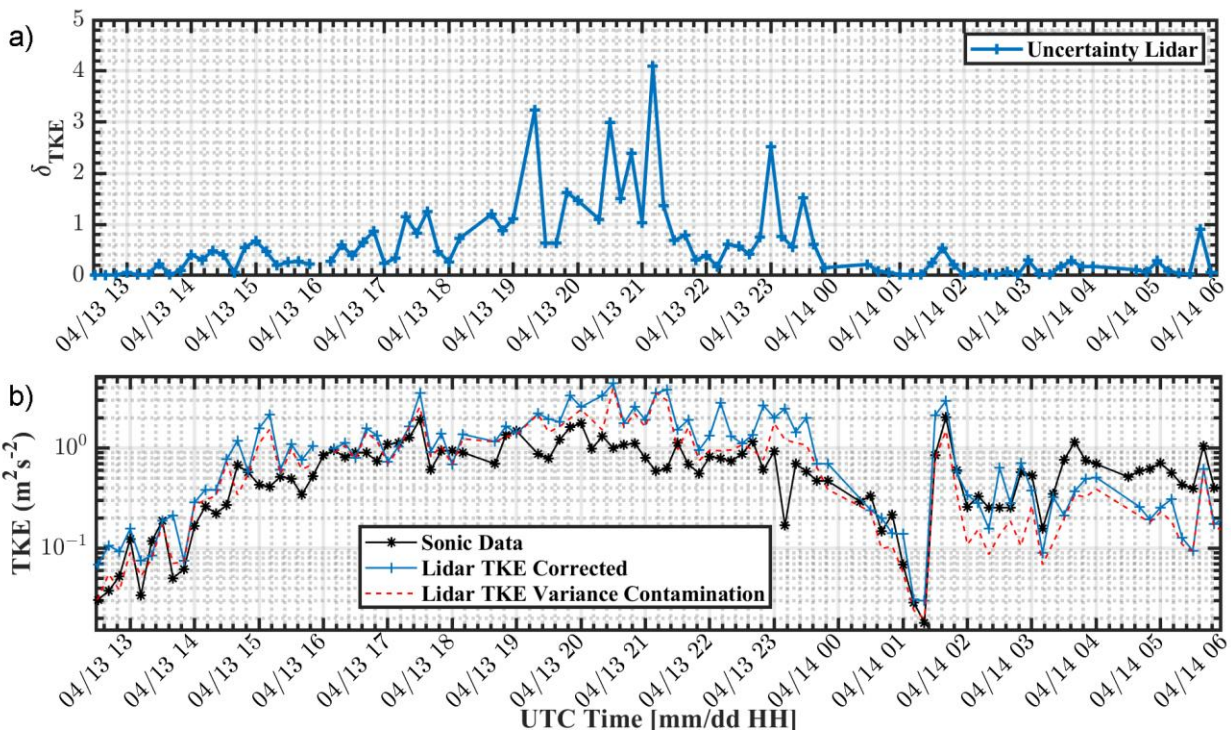


Figure 7.12. a) The uncertainty of TKE from Vindicator lidar measurements and b) time series of 10-minute averaged TKE estimates from sonic and two best methods of lidar TKE estimates (Methods 1 and 3).

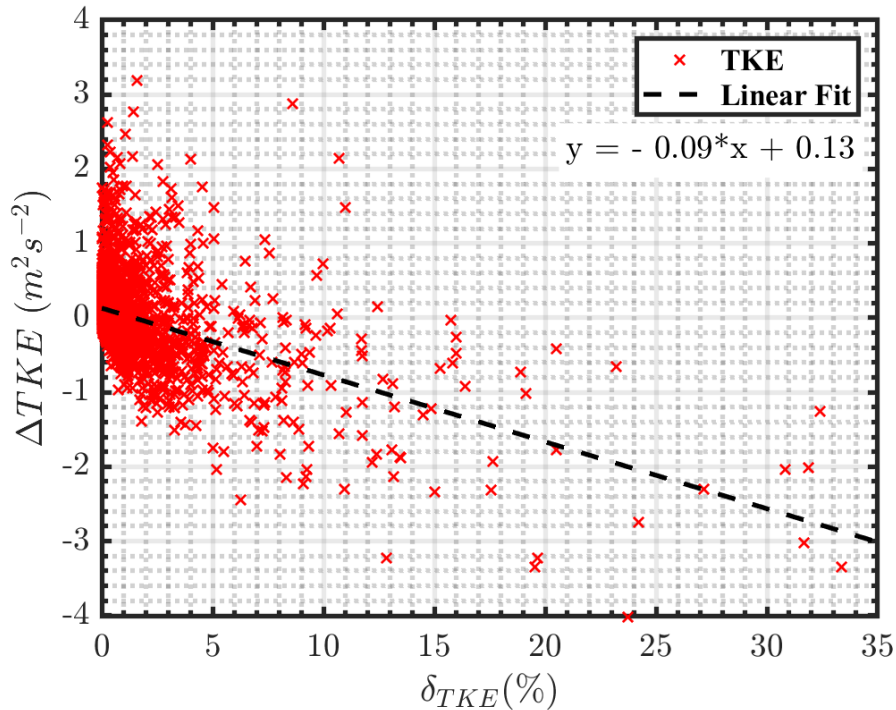


Figure 7.13. Error in TKE estimates between Method 3 and sonic anemometer at 100 m AGL versus lidar TKE uncertainty during XPIA campaign. Higher lidar uncertainty shows poorer confidence in TKE estimates.

7.4 Summary

A thorough analysis of existing turbulence methods on Vindicator lidar data was conducted with the data collected during the XPIA campaign. The Vindicator lidars showed they can estimate TI with relatively good accuracy, with a correlation coefficient greater than 85% while TKE estimates are less than 80%. The power spectral density from the Vindicator lidars does not compare well with that from the sonic anemometers and clearly shows the effect of resonance wavelengths (small separation between the beams). This effect causes larger cross-contamination effects while estimating turbulence from the Vindicator lidars. A low-pass filter of the wind vectors over 20–30 seconds filters out the effect of resonance wavelengths, but significantly underestimates spectra when compared to sonic anemometer measurements. Atmospheric stability is observed to considerably influence the turbulence spectra and turbulence error. Lidar turbulence errors are smallest during neutral atmospheric conditions, while are largest during stable atmospheric conditions. The effect of beam averaging and variance cross-contamination could be some of the reasons for these discrepancies. Out of the various TKE methods tested above, the machine learning approach provides the best results. Although they are not expected to be reproducible at all locations, further evaluation on the reproducibility of such machine learning techniques in multiple locations needs to be researched. Therefore, estimates based on 1 Hz wind vector (after multi-second averaging of radial velocities) and the modified version of variance contamination method provided the best results and could be considered as a standard for future turbulence estimations from Vindicator buoy lidars. The uncertainty evaluation based on purely statistical theory showed increased TKE uncertainties during larger deviations from sonic anemometers. Further additions to the uncertainty framework will include the effects of lidar volume averaging, instrument noise, and effect of spatial variability.

8.0 General Summary

The initial deployment for one of the DOE lidar buoys was off the coast of Virginia beginning in 2015, and the other buoy was first deployed off the coast of New Jersey beginning in 2016. Over the last two years, PNNL has had an opportunity to analyze the data collected during these first two deployments. This report has provided a summary of results from several analyses of data from the lidars and other instruments on the buoys.

A notable instrumentation challenge during the New Jersey deployment was the failure of the lidar inertial measurement unit from November 6, 2015, through the end of the deployment. The primary effect of this failure was the loss of direction information in the wind velocities above the surface. We have demonstrated that we can use the corresponding information from the TRIAXYS Next Wave II wave measurement system on the buoy to substitute for the lost data, and we have thus recovered the lost wind information.

In exceeding a year at each location, the data from these buoys provided a rare data set of offshore wind profile information in the United States, exceeding a continuous annual cycle at each location. In both locations, the strongest winds at 90 m were observed to be primarily from the southwest, although winter winds from the northwest were also prominent at the New Jersey location. As expected, winds were stronger in the winter than in the summer, and nighttime winds were somewhat stronger at each location at 90 m in a very weak mean diurnal cycle. Surface winds showed no significant mean diurnal cycle. Winds also tended to be lighter with unstable thermodynamic stratification.

We have also analyzed the wave conditions over the deployment period using data collected by the buoys. For the Virginia deployment, waves arrived mainly from the northeast and southeast, with the largest waves arriving from east-northeast. For New Jersey, principal propagation directions were from the east and southeast. The seasonal wave climate at each location aligned with general climatology of calmer conditions in the summer and more vigorous conditions in the winter. There are significant month-to-month variations in dominant wave directions. Tidal impacts on wave data were also considered. Spectral analysis showed a 3 cm amplitude impact at the Virginia location, but no significant tidal impact for the New Jersey deployment. Finally, a numerical model has been configured to complement the measurements at the lidar buoy sites. The numerical model has a spatial resolution of 1 km in the Mid-Atlantic Bight and is forced by analyzed winds and surface currents.

Investigation of the current profiles measured by each buoy generated some concern that the ADCPs both experienced some form of error causing incorrect ocean current direction measurements. Due to the lack of availability of critical beam data, the investigation into the direction shifts focused on various analyses of the 10-minute average current magnitude and direction data and comparisons to other buoy parameters. The current direction measurements during the Virginia deployment appear to gradually shift by 90–120 degrees several weeks following Hurricane Joaquin in October 2015. Analysis of currents at each depth bin show some inconsistencies, such as low bias in Bin 1 (surface) magnitudes and a shift in direction rotation with increasing depth, in the data following the direction shift. The inconsistencies suggest potential interference with one or more of the instrument beams or an error in on-board data processing, potentially related to coordinate transformations. The fact that the shift did not appear to occur at a single point in time indicates that the potential for the direction shift to be from natural physical shifts is still within the realm of possibility, but possible explanations, such as a Gulf Stream eddy, seem unlikely due to the consistency and extended duration of the shift. The lack of any form of similar shift in the wave and wind data further suggests an instrument-

related cause. The current direction measurements during the New Jersey deployment appear to shift from a bimodal to unimodal direction distribution immediately following a service visit where the instrument was removed from the water for maintenance. For future buoy deployments, it is recommended that the ADCP data be archived at the instrument sample rate and the diagnostic instrument parameters such as individual beam correlations; echo intensities; percent-good; and internal pitch, roll, and heading be archived, as well.

Beyond the basic analyses, we have also made a preliminary investigation of the wind profiles in the context of classical Monin-Obukhov Similarity Theory of the atmospheric surface layer. This required estimation of turbulent fluxes from the available buoy measurements. This was accomplished using the bulk parameterization algorithm from the Wood Hole Oceanographic Institute. Turbulent fluxes from the bulk method were used to compute the wind shear predicted by MO similarity theory. These estimates were then compared to direct measurements of wind shear using the lidar wind speed at 90 m and the surface anemometers. We found that the predicted wind shear is strongly correlated with the observed wind speed from the cup anemometers. However, the correlation between the observed and predicted wind shear was found to be essentially zero. This suggests a problem with MO similarity theory, the Dyer parameterization, or our wind shear observations. Further work is needed to reduce uncertainty and identify the source of the discrepancy.

Finally, in anticipation of future efforts to extract turbulence information from the buoys, we have also carried out a benchmark study to identify and apply algorithms to extract turbulence kinetic energy and turbulence intensity from the Vindicator lidars. The validation data were collected during the DOE-funded XPIA study at the Boulder Atmospheric Observatory in 2015, which provided the opportunity to compare turbulence information derived from Vindicator lidars with turbulence measured using sonic anemometers at multiple heights on the 300-m BAO. Five different approaches to calculating turbulence from the lidars were evaluated. The Vindicator lidars showed they can estimate TI with relatively good accuracy, with a correlation coefficient greater than 85% while TKE estimates are less than 80%. The power spectral density from the Vindicators does not compare well with that from the sonic anemometers and clearly shows the effect of resonance wavelengths (small separation between the beams). A low-pass filter of the wind vectors over 20–30 seconds filters out the effect of resonance wavelengths, but significantly underestimates spectra when compared to sonic anemometer measurements. Atmospheric stability is observed to considerably influence the turbulence spectra and turbulence error. Lidar turbulence errors are smallest during neutral atmospheric conditions, while are largest during stable atmospheric conditions. Estimates based on 1 Hz wind vector measurements (after multi-second averaging of radial velocities) and the modified version of the variance contamination method provided the best results and could be considered as a standard for future turbulence estimations from Vindicator buoy lidars. Because the data are less noisy, it is expected that the algorithms evaluated here will provide even better results for turbulence estimation when applied to data from the Leosphere v2 lidars that have just replaced the Vindicator systems on the DOE buoys.

The analyses contained in this report provide a great deal of new information about offshore conditions on the U.S. East Coast. In addition, the experience gained will inform both configurations and analysis of data from future deployments of these lidar buoy systems.

9.0 References

Ardhuin F, ST Gille, D Menemenlis, CB Rocha, N Rasche, B Chapron, J Gula and J Molemaker. 2017. "Small-Scale Open Ocean Currents Have Large Effects on Wind Wave Heights." *Journal of Geophysical Research-Oceans* 122(6):4500-4517. DOI: 10.1002/2016jc012413.

Ardhuin F, E Rogers, AV Babanin, J-F Filipot, R Magne, A Roland, A van der Westhuysen, P Queffelec, J-M Lefevre, L Aouf and F Collard. 2010. "Semiempirical Dissipation Source Functions for Ocean Waves. Part I: Definition, Calibration, and Validation." *Journal of Physical Oceanography* 40(9):1917-1941. DOI: 10.1175/2010jpo4324.1.

Benedict LH and RD Gould. 1996. "Towards Better Uncertainty Estimates for Turbulence Statistics." *Experiments in Fluids* 22(2):129-136. DOI: 10.1007/s003480050030.

Bilgili M, B Sahin and A Yasar. 2007. "Application of Artificial Neural Networks for the Wind Speed Prediction of Target Station Using Reference Stations Data." *Renewable Energy* 32(14):2350-2360. DOI: 10.1016/j.renene.2006.12.001.

Boccippio DJ. 1995. "A Diagnostic Analysis of the VVP Single-Doppler Retrieval Technique." *Journal of Atmospheric and Oceanic Technology* 12(2):230-248. DOI: 10.1175/1520-0426(1995)012<0230:Adaotv>2.0.CO;2.

Bromirski PD and DR Cayan. 2015. "Wave Power Variability and Trends Across the North Atlantic Influenced by Decadal Climate Patterns." *Journal of Geophysical Research-Oceans* 120(5):3419-3443. DOI: 10.1002/2014jc010440.

Browning KA and R Wexler. 1968. "The Determination of Kinematic Properties of a Wind Field Using Doppler Radar." *Journal of Applied Meteorology (1962-1982)* 7(1):105-113.

Bull AD. 2011. "Convergence Rates of Efficient Global Optimization Algorithms." *Journal of Machine Learning Research* 12:2879-2904. Available at <https://arxiv.org/abs/1101.3501v3>.

Chen Y, S Zhang, W Zhang, J Peng and Y Cai. 2019. "Multifactor Spatio-Temporal Correlation Model Based on a Combination of Convolutional Neural Network and Long Short-Term Memory Neural Network for Wind Speed Forecasting." *Energy Conversion and Management* 185:783-799. DOI: 10.1016/j.enconman.2019.02.018.

Dyer AJ. 1974. "A Review of Flux-Profile Relationships." *Boundary-Layer Meteorology* 7(3):363-372. DOI: 10.1007/bf00240838.

Ellenson A and HT Ozkan-Haller. 2018. "Predicting Large Ocean Wave Events Characterized by Bimodal Energy Spectra in the Presence of a Low-Level Southerly Wind Feature." *Weather and Forecasting* 33(2):479-499. DOI: 10.1175/Waf-D-17-0035.1.

Fairall CW, EF Bradley, DP Rogers, JB Edson and GS Young. 1996. "Bulk Parameterization of Air-Sea Fluxes for Tropical Ocean-Global Atmosphere Coupled-Ocean Atmosphere Response Experiment." *Journal of Geophysical Research: Oceans* 101(C2):3747-3764. DOI: 10.1029/95jc03205.

- Halliwell GR. 2004. "Evaluation of Vertical Coordinate and Vertical Mixing Algorithms in the HYbrid-Coordinate Ocean Model (HYCOM)." *Ocean Modelling* 7(3-4):285-322. DOI: 10.1016/j.ocemod.2003.10.002.
- Higgins CW, M Froidevaux, V Simeonov, N Vercauteren, C Barry and MB Parlange. 2012. "The Effect of Scale on the Applicability of Taylor's Frozen Turbulence Hypothesis in the Atmospheric Boundary Layer." *Boundary-Layer Meteorology* 143(2):379-391. DOI: 10.1007/s10546-012-9701-1.
- Hsieh WW and B Tang. 1998. "Applying Neural Network Models to Prediction and Data Analysis in Meteorology and Oceanography." *Bulletin of the American Meteorological Society* 79(9):1855-1870. DOI: 10.1175/1520-0477(1998)079<1855:Annmtp>2.0.CO;2.
- Kelberlau F and J Mann. 2019. "Better Turbulence Spectra from Velocity–Azimuth Display Scanning Wind Lidar." *Atmospheric Measurement Techniques* 12(3):1871-1888. DOI: 10.5194/amt-12-1871-2019.
- Kendall MG and A Stuart. 1958. *The Advanced Theory of Statistics*, London: C. Griffin. Three volumes.
- Kline SJ and FA McClintock. 1953. "Describing Uncertainties in Single-Sample Experiments." *Mechanical Engineering* 75(1):3-8.
- Komar PD and JC Allan. 2008. "Increasing Hurricane-Generated Wave Heights Along the US East Coast and Their Climate Controls." *Journal of Coastal Research* 24(2):479-488. DOI: 10.2112/07-0894.1.
- Krishnamurthy R, A Choukulkar, R Calhoun, J Fine, A Oliver and KS Barr. 2013. "Coherent Doppler Lidar for Wind Farm Characterization." *Wind Energy* 16(2):189-206. DOI: 10.1002/we.539.
- Kumer V-M, J Reuder, M Dorninger, R Zauner and V Grubišić. 2016. "Turbulent Kinetic Energy Estimates from Profiling Wind LiDAR Measurements and Their Potential for Wind Energy Applications." *Renewable Energy* 99:898-910. DOI: 10.1016/j.renene.2016.07.014.
- Lenschow DH, V Wulfmeyer and C Senff. 2000. "Measuring Second- through Fourth-Order Moments in Noisy Data." *Journal of Atmospheric and Oceanic Technology* 17(10):1330-1347. DOI: 10.1175/1520-0426(2000)017<1330:Mstfom>2.0.CO;2.
- Lundquist JK, JM Wilczak, R Ashton, L Bianco, WA Brewer, A Choukulkar, A Clifton, M Debnath, R Delgado, K Friedrich, S Gunter, A Hamidi, GV Iungo, A Kaushik, B Kosović, P Langan, A Lass, E Lavin, JC-Y Lee, KL McCaffrey, RK Newsom, DC Noone, SP Oncley, PT Quelet, SP Sandberg, JL Schroeder, WJ Shaw, L Sparling, CS Martin, AS Pe, E Strobach, K Tay, BJ Vanderwende, A Weickmann, D Wolfe and R Worsnop. 2017. "Assessing State-of-the-Art Capabilities for Probing the Atmospheric Boundary Layer: The XPIA Field Campaign." *Bulletin of the American Meteorological Society* 98(2):289-314. DOI: 10.1175/bams-d-15-00151.1.
- Mann J. 1994. "The Spatial Structure of Neutral Atmospheric Surface-Layer Turbulence." *Journal of Fluid Mechanics* 273:141-168. DOI: 10.1017/S0022112094001886.

- Mann J, A Peña, F Bingöl, R Wagner and MS Courtney. 2010. "Lidar Scanning of Momentum Flux in and above the Atmospheric Surface Layer." *Journal of Atmospheric and Oceanic Technology* 27(6):959-976. DOI: 10.1175/2010jtecha1389.1.
- McGovern A, R Lagerquist, DJG II, GE Jergensen, KL Elmore, CR Homeyer and T Smith. 2019. "Making the Black Box More Transparent: Understanding the Physical Implications of Machine Learning." *Bulletin of the American Meteorological Society* 100(11):2175-2199. DOI: 10.1175/bams-d-18-0195.1.
- Mentaschi L, G Besio, F Cassola and A Mazzino. 2015. "Performance Evaluation of Wavewatch III in the Mediterranean Sea." *Ocean Modelling* 90:82-94. DOI: 10.1016/j.ocemod.2015.04.003.
- Moffat RJ. 1982. "Contributions to the Theory of Single-Sample Uncertainty Analysis." *Journal of Fluids Engineering* 104(2):250-258. DOI: 10.1115/1.3241818.
- Newman JF, PM Klein, S Wharton, A Sathe, TA Bonin, PB Chilson and A Muschinski. 2016. "Evaluation of Three Lidar Scanning Strategies for Turbulence Measurements." *Atmospheric Measurement Techniques* 9(5):1993-2013. DOI: 10.5194/amt-9-1993-2016.
- Newsom RK. 2016. *Optimizing Lidar Wind Measurements from the DOE WindSentinel Buoys*. PNNL-25512. Richland, WA: Pacific Northwest National Laboratory. Available at https://www.pnnl.gov/main/publications/external/technical_reports/PNNL-25512.pdf.
- Newsom RK, WA Brewer, JM Wilczak, DE Wolfe, SP Oncley and JK Lundquist. 2017. "Validating Precision Estimates in Horizontal Wind Measurements from a Doppler Lidar." *Atmospheric Measurement Techniques* 10(3):1229-1240. DOI: 10.5194/amt-10-1229-2017.
- NGDS. 1999a. "U.S. Coastal Relief Model – Northeast Atlantic." Boulder, CO: National Geophysical Data Center (NGDC), NOAA. Accessed July 5, 2019. DOI: 10.7289/V5MS3QNZ.
- NGDS. 1999b. "U.S. Coastal Relief Model – Southeast Atlantic." Boulder, CO: National Geophysical Data Center (NGDC), NOAA. Accessed July 5, 2019. DOI: 10.7289/V53R0QR5.
- Perez J, M Menendez and IJ Losada. 2017. "GOW2: A Global Wave Hindcast for Coastal Applications." *Coastal Engineering* 124:1-11. DOI: 10.1016/j.coastaleng.2017.03.005.
- Raschle N and F Ardhuin. 2013. "A Global Wave Parameter Database for Geophysical Applications. Part 2: Model Validation with Improved Source Term Parameterization." *Ocean Modelling* 70:174-188. DOI: 10.1016/j.ocemod.2012.12.001.
- Saha S, S Moorthi, XR Wu, J Wang, S Nadiga, P Tripp, D Behringer, YT Hou, HY Chuang, M Iredell, M Ek, J Meng, RQ Yang, MP Mendez, H Van Den Dool, Q Zhang, WQ Wang, MY Chen and E Becker. 2014. "The NCEP Climate Forecast System Version 2." *Journal of Climate* 27(6):2185-2208. DOI: 10.1175/Jcli-D-12-00823.1.
- Sathe A and J Mann. 2013. "A Review of Turbulence Measurements Using Ground-Based Wind Lidars." *Atmospheric Measurement Techniques* 6(11):3147-3167. DOI: 10.5194/amt-6-3147-2013.

- Sathe A, J Mann, J Gottschall and MS Courtney. 2011. "Can Wind Lidars Measure Turbulence?" *Journal of Atmospheric and Oceanic Technology* 28(7):853-868. DOI: 10.1175/jtech-d-10-05004.1.
- Shaw WJ, MI Pekour and RK Newsom. 2018. *Lidar Buoy Data Analysis: Basic Assessment of Observed Conditions and Instrument Performance off Virginia and New Jersey*. PNNL-28058. Richland, WA: Pacific Northwest National Laboratory.
- Taylor GI. 1938. "The Spectrum of Turbulence." *Proceedings of the Royal Society A: Mathematical, Physical and Engineering Sciences* 164(919):476-490. DOI: 10.1098/rspa.1938.0032.
- Thiébaux HJ and FW Zwiers. 1984. "The Interpretation and Estimation of Effective Sample Size." *Journal of Climate and Applied Meteorology* 23(5):800-811. DOI: 10.1175/1520-0450(1984)023<0800:Tiaeoe>2.0.CO;2.
- Tukey JW. 1958. "Bias and Confidence in Not-quite Large Samples." In *The Annals of Mathematical Statistics*, p. 614. Beachwood, OH: The Institute of Mathematical Statistics. 29. Abstracts of Papers: Abstracts of papers presented at the Ames, Iowa Meeting of the Institute, April 3-5, 1958. DOI: 10.1214/aoms/1177706647.
- WW3DG. 2016. *User Manual and System Documentation of WAVEWATCH III® Version 5.16*. MMAB Contribution No. 316. College Park, MD: WAVEWATCH III Development Group (WW3DG), National Oceanic and Atmospheric Administration, National Weather Service, National Centers for Environmental Prediction.
- Wyngaard JC. 2010. *Turbulence in the Atmosphere*, Cambridge, United Kingdom: Cambridge University Press. ISBN 9780521887694.
- Young IR and MA Donelan. 2018. "On the Determination of Global Ocean Wind and Wave Climate from Satellite Observations." *Remote Sensing of Environment* 215:228-241. DOI: 10.1016/j.rse.2018.06.006.

Appendix A – Format of NetCDF Files Containing Reprocessed 1 Hz Winds

```

netcdf \6NB00130_reprocessed_lidar_1Hz_20160608 {
dimensions:
time = 86333;
height = 6;
variables:
int base_time;
base_time:long_name = "Base time in Epoch";
base_time:units = "seconds since 1970-1-1 0:00:00 0:00";
double time_offset(time);
time_offset:long_name = "Time offset from base_time";
time_offset:units = "seconds";
float height(height);
height:long_name = "Height above ground";
height:units = "m";
float pnnl_wspd(height, time);
pnnl_wspd:long_name = "Reprocessed wind speed using AXYS IMU data";
pnnl_wspd:units = "m/s";
float pnnl_wdir(height, time);
pnnl_wdir:long_name = "Reprocessed wind direction using AXYS IMU data";
pnnl_wdir:units = "deg";
float pnnl_w(height, time);
pnnl_w:long_name = "Reprocessed vertical wind component using AXYS IMU data";
pnnl_w:units = "m/s";
float pnnl_yaw(time);
pnnl_yaw:long_name = "Yaw angle from the AXYS IMU";
pnnl_yaw:units = "deg";
float pnnl_pitch(time);
pnnl_pitch:long_name = "Pitch angle from the AXYS IMU";
pnnl_pitch:units = "deg";
float pnnl_roll(time);
pnnl_roll:long_name = "Roll angle from the AXYS IMU";
pnnl_roll:units = "deg";
byte pnnl_attitude_qc(time);
pnnl_attitude_qc:long_name = "Quality control parameter for attitude measurements, 1 is good, 0 is bad";
pnnl_attitude_qc:units = "unitless";
byte pnnl_wind_qc(height, time);
pnnl_wind_qc:long_name = "Quality control parameter for wind measurements, 1 is good, 0 is bad";
pnnl_wind_qc:units = "unitless";
float oads_wspd(height, time);
oads_wspd:long_name = "Reprocessed wind speed using AXYS IMU data";
oads_wspd:units = "m/s";
float oads_wdir(height, time);
oads_wdir:long_name = "Reprocessed wind direction using AXYS IMU data";
oads_wdir:units = "deg";
float oads_w(height, time);

```

```

oads_w:long_name = "Reprocessed vertical wind component using AXYS IMU data";
oads_w:units = "m/s";
float oads_yaw(time);
oads_yaw:long_name = "Yaw angle from the AXYS IMU";
oads_yaw:units = "deg";
float oads_pitch(time);
oads_pitch:long_name = "Pitch angle from the AXYS IMU";
oads_pitch:units = "deg";
float oads_roll(time);
oads_roll:long_name = "Roll angle from the AXYS IMU";
oads_roll:units = "deg";
byte oads_attitude_qc(time);
oads_attitude_qc:long_name = "Quality control parameter for attitude measurements, 1 is good,
0 is bad";
oads_attitude_qc:units = "unitless";
byte oads_wind_qc(height, time);
oads_wind_qc:long_name = "Quality control parameter for wind measurements, 1 is good, 0 is
bad";
oads_wind_qc:units = "unitless";
float sig1(height, time);
sig1:long_name = "Signal strength along beam 1";
sig1:units = "unitless";
float sig2(height, time);
sig2:long_name = "Signal strength signal along beam 2";
sig2:units = "unitless";
float sig3(height, time);
sig3:long_name = "Signal strength signal along beam 3";
sig3:units = "unitless";
float lat(time);
lat:long_name = "north latitude";
lat:units = "degrees";
float lon(time);
lon:long_name = "east longitude";
lon:units = "degrees";

// global attributes:
:date = "Mon Dec 2 10:38:46 2019";
:missing-data = -9999;
}

```

Appendix B – Format of NetCDF Files Containing Reprocessed Time Averaged Winds

```

netcdf \6NB00130_reprocessed_lidar_10min_20160531 {
dimensions:
time = 144;
height = 6;
variables:
int base_time;
base_time:long_name = "Base time in Epoch";
base_time:units = "seconds since 1970-1-1 0:00:00 0:00";
double time_offset(time);
time_offset:long_name = "Time offset from base_time";
time_offset:units = "seconds";
float height(height);
height:long_name = "Height above ground";
height:units = "m";
float pnnl_wspd(height, time);
pnnl_wspd:long_name = "Reprocessed scalar averaged wind speed using AXYS IMU data";
pnnl_wspd:units = "m/s";
float pnnl_gust(height, time);
pnnl_gust:long_name = "Reprocessed wind speed gust using AXYS IMU data";
pnnl_gust:units = "m/s";
float pnnl_wspd_std(height, time);
pnnl_wspd_std:long_name = "Reprocessed wind speed standard deviation using AXYS IMU
data";
pnnl_wspd_std:units = "m/s";
float pnnl_u(height, time);
pnnl_u:long_name = "Reprocessed easterly wind component using AXYS IMU data";
pnnl_u:units = "m/s";
float pnnl_u_std(height, time);
pnnl_u_std:long_name = "Reprocessed easterly wind component standard deviation using
AXYS IMU data";
pnnl_u_std:units = "m/s";
float pnnl_v(height, time);
pnnl_v:long_name = "Reprocessed northerly wind component using AXYS IMU data";
pnnl_v:units = "m/s";
float pnnl_v_std(height, time);
pnnl_v_std:long_name = "Reprocessed northerly wind component standard deviation using
AXYS IMU data";
pnnl_v_std:units = "m/s";
float pnnl_w(height, time);
pnnl_w:long_name = "Reprocessed vertical wind component using AXYS IMU data";
pnnl_w:units = "m/s";
float pnnl_w_std(height, time);
pnnl_w_std:long_name = "Reprocessed vertical wind component standard deviation using
AXYS IMU data";
pnnl_w_std:units = "m/s";
float pnnl_wdir(height, time);
pnnl_wdir:long_name = "Reprocessed vector averaged wind direction using AXYS IMU data";

```

```

pnnl_wdir:units = "deg";
float pnnl_wdir_std(height, time);
pnnl_wdir_std:long_name = "Reprocessed wind direction standard deviation using AXYS IMU data";
pnnl_wdir_std:units = "deg";
float pnnl_yaw(time);
pnnl_yaw:long_name = "Vector average yaw angle for the AXYS IMU";
pnnl_yaw:units = "deg";
float pnnl_yaw_std(time);
pnnl_yaw_std:long_name = "Standard deviation of yaw angle from the AXYS IMU";
pnnl_yaw_std:units = "deg";
float pnnl_roll_std(time);
pnnl_roll_std:long_name = "Standard deviation of the roll angle from the AXYS IMU";
pnnl_roll_std:units = "deg";
float pnnl_pitch_std(time);
pnnl_pitch_std:long_name = "Standard deviation of the pitch angle from the AXYS IMU";
pnnl_pitch_std:units = "deg";
float pnnl_attitude_qc(time);
pnnl_attitude_qc:long_name = "Quality control parameter for attitude measurements, 1 is good, 0 is bad";
pnnl_attitude_qc:units = "unitless";
float pnnl_wind_qc(height, time);
pnnl_wind_qc:long_name = "Quality control parameter for wind measurements, 1 is good, 0 is bad";
pnnl_wind_qc:units = "unitless";
float oads_wspd(height, time);
oads_wspd:long_name = "Reprocessed wind speed using OADS IMU data";
oads_wspd:units = "m/s";
float oads_gust(height, time);
oads_gust:long_name = "Reprocessed wind speed gust using OADS IMU data";
oads_gust:units = "m/s";
float oads_wspd_std(height, time);
oads_wspd_std:long_name = "Reprocessed wind speed standard deviation using OADS IMU data";
oads_wspd_std:units = "m/s";
float oads_u(height, time);
oads_u:long_name = "Reprocessed easterly wind component using OADS IMU data";
oads_u:units = "m/s";
float oads_u_std(height, time);
oads_u_std:long_name = "Reprocessed easterly wind component standard deviation using OADS IMU data";
oads_u_std:units = "m/s";
float oads_v(height, time);
oads_v:long_name = "Reprocessed northerly wind component using OADS IMU data";
oads_v:units = "m/s";
float oads_v_std(height, time);
oads_v_std:long_name = "Reprocessed northerly wind component standard deviation using OADS IMU data";
oads_v_std:units = "m/s";
float oads_w(height, time);
oads_w:long_name = "Reprocessed vertical wind component using OADS IMU data";

```

```

oads_w:units = "m/s";
float oads_w_std(height, time);
oads_w_std:long_name = "Reprocessed vertical wind component standard deviation using
OADS IMU data";
oads_w_std:units = "m/s";
float oads_wdir(height, time);
oads_wdir:long_name = "Reprocessed wind direction using OADS IMU data";
oads_wdir:units = "deg";
float oads_wdir_std(height, time);
oads_wdir_std:long_name = "Reprocessed wind direction standard deviation using OADS IMU
data";
oads_wdir_std:units = "deg";
float oads_yaw(time);
oads_yaw:long_name = "Vector average yaw angle from the OADS IMU";
oads_yaw:units = "deg";
float oads_yaw_std(time);
oads_yaw_std:long_name = "Standard deviation of the yaw angle from the OADS IMU";
oads_yaw_std:units = "deg";
float oads_roll_std(time);
oads_roll_std:long_name = "Standard deviation of the roll angle from the OADS IMU";
oads_roll_std:units = "deg";
float oads_pitch_std(time);
oads_pitch_std:long_name = "Standard deviation of the pitch angle from the OADS IMU";
oads_pitch_std:units = "deg";
float oads_attitude_qc(time);
oads_attitude_qc:long_name = "Quality control parameter for attitude measurements, 1 is good,
0 is bad";
oads_attitude_qc:units = "unitless";
float oads_wind_qc(height, time);
oads_wind_qc:long_name = "Quality control parameter for wind measurements, 1 is good, 0 is
bad";
oads_wind_qc:units = "unitless";
float sig1(height, time);
sig1:long_name = "Mean signal along beam 1";
sig1:units = "unitless";
float sig2(height, time);
sig2:long_name = "Mean signal along beam 2";
sig2:units = "unitless";
float sig3(height, time);
sig3:long_name = "Mean signal along beam 3";
sig3:units = "unitless";
float lat(time);
lat:long_name = "north latitude";
lat:units = "degrees";
float lon(time);
lon:long_name = "east longitude";
lon:units = "degrees";
// global attributes:
:date = "Mon Dec 2 12:47:12 2019";
:missing-data = -9999;
:averaging_time_seconds = 600;}

```

Pacific Northwest National Laboratory

902 Battelle Boulevard
P.O. Box 999
Richland, WA 99354
1-888-375-PNNL (7665)

www.pnnl.gov